REPORT DOCUMENTATION PAGE

Form Approved
OMB NO. 0704-0188

1. AGENCY USE ONLY (Leave Blank)	2. REPORT DATE 28 April 2003	3. REPORT TYPE AND DATES COVERED Final report for 15 Sept. 2001 to 14 Sept. 2002

4. TITLE AND SUBTITLE
GPR Performance in the Presence of Buried Biomass: Final Report

5. FUNDING NUMBERS
C: DAAD19-01-1-0760
PR: E-43042-EL-000-01234-1

6. AUTHOR(S)
Nakasit Niltawach, M. Higgins, Joel T. Johnson, Chi-Chih Chen, and Brian A. Baertlein

7. PERFORMING ORGANIZATION NAME(S) AND ADDRESS(ES)
The Ohio State University ElectroScience Laboratory
1320 Kinnear Road
Columbus, OH 43212

8. PERFORMING ORGANIZATION REPORT NUMBER 741809-3

9. SPONSORING / MONITORING AGENCY NAME(S) AND ADDRESS(ES)

U. S. Army Research Office
P.O. Box 12211
Research Triangle Park, NC 27709-2211

10. SPONSORING / MONITORING AGENCY REPORT NUMBER

11. SUPPLEMENTARY NOTES
The views, opinions and/or findings contained in this report are those of the author(s) and should not be construed as an official Department of the Army position, policy or decision, unless so designated by other documentation.

12 a. DISTRIBUTION / AVAILABILITY STATEMENT
Approved for public release; distribution unlimited.

12 b. DISTRIBUTION CODE

13. ABSTRACT (Maximum 200 words)
The effects of buried biomass (e.g., tree roots) on GPR performance were examined through a combination of theory and experiment. In Part 1, experiments performed at Eglin AFB, FL are described. Wideband polarimetric GPR data were acquired at sites where extensive root structures are known to exist. After completing those measurements, the site was excavated to a depth of 24 inches, and the root content was exhumed intact. Soil samples were acquired at the same time. In Part 2, analyses of the root structure and GPR data are presented. An efficient numerical model for calculating root scattering was developed using the discrete dipole approximation (DDA). The DDA model was then used to simulate GPR data collected at Eglin. Additional studies found that root scattering is roughly proportional to the dielectric contrast and to the root cross-sectional area. Additional simulations suggest that roots have a very modest affect on the signatures of targets buried under them, but they are a significant source of clutter, particularly at frequencies above about 0.5 GHz. A statistical study based on simulated data suggests that root-related clutter will strongly affect detectability.

14. SUBJECT TERMS
Ground-penetrating radar (GPR), roots, biomass, propagation, clutter

15. NUMBER OF PAGES
118

16. PRICE CODE

17. SECURITY CLASSIFICATION OR REPORT	18. SECURITY CLASSIFICATION ON THIS PAGE	19. SECURITY CLASSIFICATION OF ABSTRACT	20. LIMITATION OF ABSTRACT
UNCLASSIFIED	**UNCLASSIFIED**	**UNCLASSIFIED**	**UL**

NSN 7540-01-280-5500
Standard Form 298 (Rev.2-89)
Prescribed by ANSI Std. 239-18 298-102

REPORT DOCUMENTATION PAGE (SF298)
(Continuation Sheet)

GPR Performance in the Presence of Buried Biomass

Part 1: Experimental Findings

Final Report

for the period

15 September 2001 – 14 September 2002

Contract: DAAD19-01-1-0760
Project: E-43042-EL-000-01234-1

Prepared for

Dr. Russell Harmon
The US Army Research Office
P.O. Box 12211
Research Triangle Park, NC 27709-2211

Prepared by

Mr. M. Higgins
Mr. N. Niltawach
Prof. J. T. Johnson
Dr. C.-C. Chen
Dr. B. A. Baertlein

The Ohio State University
ElectroScience Laboratory
1320 Kinnear Road
Columbus, OH 43212

20 September 2002

Table of Contents

TABLE OF CONTENTS II

LIST OF FIGURES III

1.0 INTRODUCTION 1

2.0 GPR MEASUREMENTS WITH A GROUND-CONTACTING ANTENNA 2

2.1 GPR Description 2

2.2 Results 5

2.3 Statistical Characterization of Clutter i

3.0 SURFACE SCATTERING MEASUREMENTS FROM ELEVATED HORN VIII

3.1 Measurement Setup viii

3.2 Results ix

4.0 SUPPLEMENTAL MEASUREMENTS XII

4.1 Root Structure and Properties xii

4.2 Shrub density. xiv

5.0 CONCLUSIONS XVI

APPENDIX: FILE FORMATS XVII

List of Figures

Figure 1. Test locations at Eglin AFB, Site C62 2
Figure 2. Ground-contacting GPR system with dielectric-loaded horn antenna. The horn is made from two folded bow-tie elements terminated in resistive film. 3
Figure 3. GPR system (top view). A small wheeled platform is used to drag the ground-contacting antenna, which is mounted on a circular plastic sled. 3
Figure 4. GPR system (side view). The antenna is connected to the network analyzer via a semi-rigid coaxial cable. Trailing arms connect the antenna platform and the wheeled cart. 4
Figure 5 GPR measurement paths (not to scale). 5
Figure 6 S_{11} Site 2, frequency-domain one-foot-depth rod, centered 6
Figure 7 S_{22} Site 2, frequency-domain one-foot-depth rod, centered 6
Figure 8 S_{21} Site 2, frequency-domain one-foot-depth rod, centered 6
Figure 9 S_{11} Site 1, center scan of three-foot-depth rod 7
Figure 10 S_{11} Site 1, offset scan of three-foot-depth rod 7
Figure 11 S_{11} Site 2, center scan of three-foot-depth rod. 8
Figure 12 S_{11} Site 2, offset scan of three-foot-depth rod. 8
Figure 13 S_{22} Site 1, center scan of three-foot-depth rod 8
Figure 14 S_{22} Site 1, offset scan of three-foot-depth rod 8
Figure 15 S_{22} Site 2, center scan of three-foot-depth rod 8
Figure 16 S_{22} Site 2, offset scan of three-foot-depth rod 8
Figure 17 S_{21} Site 1, center scan of three-foot-depth rod 9
Figure 18 S_{21} Site 1, offset scan of three-foot-depth rod 9
Figure 19 S_{21} Site 2, center scan of three-foot-depth rod 9
Figure 20 S_{21} Site 2, offset scan of three-foot-depth rod 9
Figure 21 S_{11} Site 1, center scan of two-foot-depth rod 9
Figure 22 S_{11} Site 1, offset scan of two-foot-depth rod 9
Figure 23 S_{11} Site 2, center scan of two-foot-depth rod 10
Figure 24 S_{11} Site 2, offset scan of two-foot-depth rod 10
Figure 25 S_{22} Site 1, center scan of two-foot-depth rod 10
Figure 26 S_{22} Site 1, offset scan of two-foot-depth rod 10
Figure 27 S_{22} Site 2, center scan of two-foot-depth rod 10
Figure 28 S_{22} Site 2, offset scan of two-foot-depth rod 10
Figure 29 S_{21} Site 1, center scan of two-foot-depth rod 11
Figure 30 S_{21} Site 1, offset scan of two-foot-depth rod 11
Figure 31 S_{21} Site 2, center scan of two-foot-depth rod 11
Figure 32 S_{21} Site 2, offset scan of two-foot-depth rod 11
Figure 33 S_{11} Site 1, center scan of one-foot-depth rod 11
Figure 34 S_{11} Site 1, offset scan of one-foot-depth rod 11
Figure 35 S_{11} Site 2, center scan of one-foot-depth rod 12
Figure 36 S_{11} Site 2, offset scan of one-foot-depth rod 12
Figure 37 S_{22} Site 1, center scan of one-foot-depth rod 12
Figure 38 S_{22} Site 1, offset scan of one-foot-depth rod 12
Figure 39 S_{22} Site 2, center scan of one-foot-depth rod 12
Figure 40 S_{22} Site 2, offset scan of one-foot-depth rod 12
Figure 41 S_{21} Site 1, center scan of one-foot-depth rod 13
Figure 42 S_{21} Site 1, offset scan of one-foot-depth rod 13
Figure 43 S_{21} Site 2, center scan of one-foot-depth rod 13
Figure 44 S_{21} Site 2, offset scan of one-foot-depth rod 13
Figure 45 S_{11} Site 1, time-domain empty site 13
Figure 46 S_{22} Site 1, time-domain Empty Site 13
Figure 47 S_{11} Site 2, time-domain empty site 14
Figure 48 S_{22} Site 2, time-domain empty site 14

Figure 49 S_{21} Site 1, time-domain empty site 14
Figure 50 S_{21} Site 2, time-domain empty site 14
Figure 51 S_{11} Standard deviation for the full band (50 to 1500 MHz)..... ii
Figure 52 S_{22} standard deviation for the full band (50 to 1500 MHz) ii
Figure 53 S_{21} standard deviation for the full band (50 to 1500 MHz) iii
Figure 54 S_{11} standard deviation for the band 250 to 750 MHz iii
Figure 55 S_{22} standard deviation for the band 250 to 750 MHz iv
Figure 56 S_{21} standard deviation for the band 250 to 750 MHz iv
Figure 57 S_{11} standard deviation for the band 50 to 250 MHz v
Figure 58 S_{22} standard deviation for the band 50 to 250 MHz v
Figure 59 S_{21} standard deviation for the band 50 to 250 MHz vi
Figure 60 S_{11} standard deviation for the band 750 to 1500 MHz vi
Figure 61 S_{22} standard deviation for the band 750 to 1500 MHz vii
Figure 62 S_{21} standard deviation for the band 750 to 1500 MHz vii
Figure 63 Surface scattering measurement setup with calibration sphere..... viii
Figure 64 Dimensions relevant to the surface scattering measurement. ix
Figure 65. Background-suppressed data (i.e., sphere – no sphere) for the parallel polarization plotted in the time-domain for the frequency band 50 – 2000 MHz..... x
Figure 66. Background-suppressed data (i.e., sphere – no sphere) for the perpendicular polarization plotted in the time-domain for the frequency band 50 – 2000 MHz x
Figure 67 Parallel polarization return for the empty site (50 – 2000 MHz)..... xi
Figure 68 Perpendicular polarization return for the empty site (50 – 2000 MHz)..... xi
Figure 69. The test sites after excavation to a depth of 24 inches. The roots were left intact and painted red for better visibility. String lines mark 1 meter square sections xii
Figure 70. Top view of the root distribution at Site 1, obtained by ortho-rectifying a mosaic of photos..... xiii
Figure 71 Histogram of root diameters..... xiv
Figure 72. Near-surface soil shows darker color than deeper soil..... xiv

1.0 Introduction

This document comprises Part 1 of the final report for the research effort entitled "GPR performance in the presence of buried biomass" (Contract DAAD19-01-1-0760, Project No.: E-43042-EL-000-01234-1). There is extensive anecdotal evidence that biomass (i.e., plant and tree roots) adversely affects ground-penetrating radar (GPR) performance. In this effort the Ohio State University (OSU) ElectroScience Laboratory (ESL) described the physics that govern the propagation and scattering of GPR waveforms in the presence of buried biomass. This work is being performed in collaboration with the US Army Research Laboratory.

This report is presented in two parts. In Part 1 we document the results of experimental GPR measurements performed at Site C62 at Eglin, AFB, FL. In Part 2 we describe numerical modeling work that permits us to simulate and interpret many of the results presented herein.

This document is organized in three major sections. In Section 2 we discuss measurements performed with a ground-contacting GPR antenna. In Section 3 we discuss surface-scattering measurements performed with an elevated antenna. Finally, in Section 4 we describe measurements of some supplemental data, including descriptions of the root structures found at the test site. Concluding remarks appear in Section 5.

2.0 GPR Measurements with a Ground-Contacting Antenna

A team from ESL visited Site C62 at Eglin AFB, FL during December 10-12, 2001 to perform radar measurements and to collect samples of soil and roots. The area is covered with tufts of grass and short scrub oak trees that are periodically cut back to ground level (see Figure 1). At the time of these measurements, the average height of those trees was less than 24 inches. Using the local density of trees as a guide, it was postulated that the regions in Figure 1(a) and (b) would have relatively high and low root densities respectively. All of the results documented in this report were acquired at these locations, which are separated from one another by only a few tens of meters at Site C62. At each location we selected regions of size two meters square for our study. The region with high root density is referred to hereafter as "Site 1" and the low root density region is designated "Site 2".

(a) Site 1 (high root density) (b) Site 2 (low root density)

Figure 1. Test locations at Eglin AFB, Site C62

2.1 GPR Description

An ultra-wide bandwidth, multi-polarization, ground penetrating radar (GPR) was used to collect data at Sites 1 and 2. The "radar" comprises a commercial RF vector network analyzer (HP8753C) for collecting reflection data (via the S parameters $S_{11}$and S_{22}) and transmission data (S_{21}) and a dual-polarized antenna utilizing a dielectric-loaded horn design developed at OSU/ESL. The horn section is filled with an artificial dielectric with a relative dielectric constant of five, which is well matched to the local soil. The complete radar and a conceptual view of the antenna are shown in Figure 2. The antenna was oriented such that one of the two dipole-elements was parallel to the direction of scan. The return from the parallel arm comprises channel 2 and the return from the perpendicular arm comprises channel 1. Data were collected over the frequency range 0.05 to 2.0 GHz.

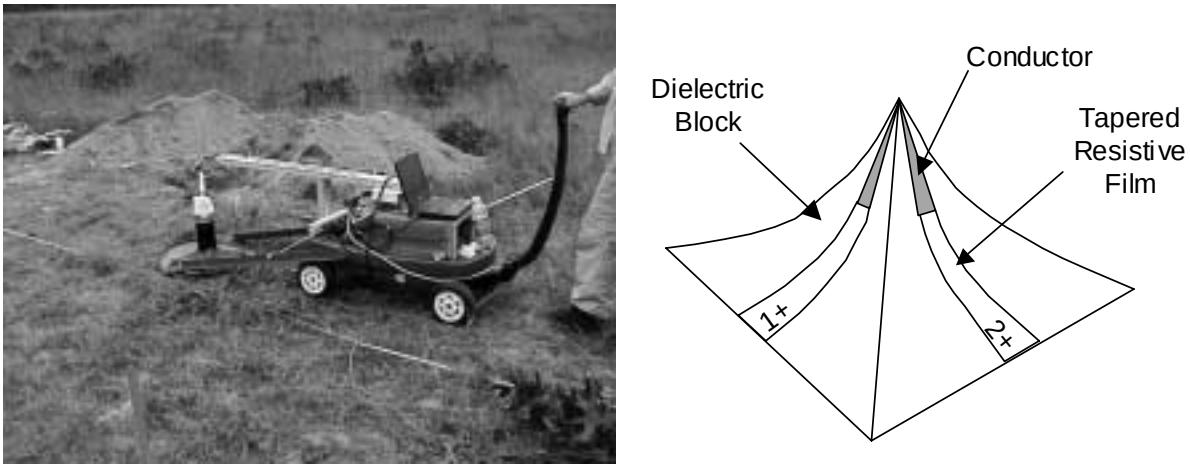

(a) horn antenna and cart-mounted GPR (b) horn antenna schematic

Figure 2. Ground-contacting GPR system with dielectric-loaded horn antenna. The horn is made from two folded bow-tie elements terminated in resistive film.

The radar's control and data collection functions were performed by a laptop computer using OSU-developed software operating over a GPIB connection. The configuration of the components is illustrated in Figure 3 and Figure 4. The network analyzer and laptop were mounted on a non-metallic wheeled platform. The antenna was placed on a circular sled attached to the back of the wagon by two trailing arms.

Data were acquired using this system at 41 positions spaced at three-inch intervals. Herein we refer to this spatial sampling as a "scan". At each position in the scan three polarimetric components were sampled as S_{11}, S_{22} and S_{21}. Each sample comprised measurements at 401 frequency steps from 0.05 to 2.0 GHz (step size=4.875 MHz). The IF bandwidth was set to 300 Hz, and the power level was set to 0 dBm. The real and imaginary parts of the measured *S* parameters were stored as binary files using the format described in the Appendix.

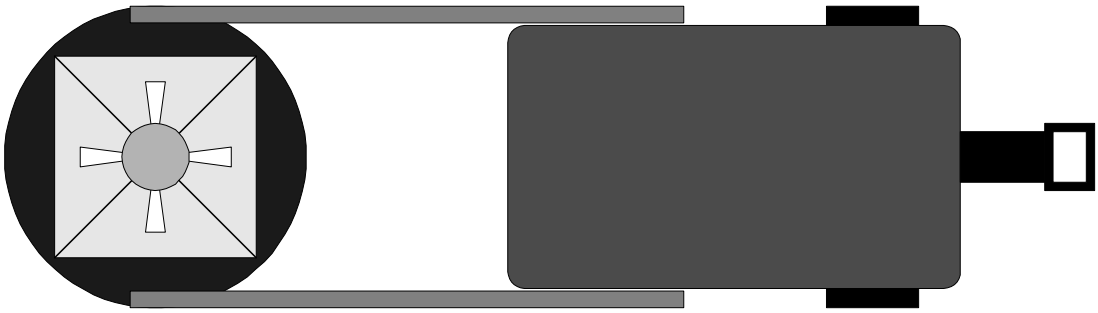

Figure 3. GPR system (top view). A small wheeled platform is used to drag the ground-contacting antenna, which is mounted on a circular plastic sled.

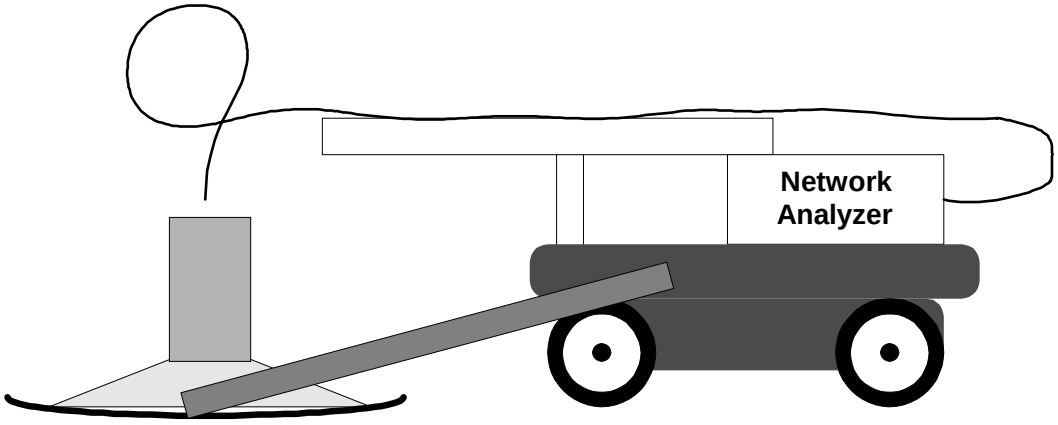

Figure 4. GPR system (side view). The antenna is connected to the network analyzer via a semi-rigid coaxial cable. Trailing arms connect the antenna platform and the wheeled cart.

Prior to making any measurements, we removed the large surface vegetation (primarily the low scrub oak trees). Local EOD personnel then performed a sweep of the areas using magnetometers and metal detectors. (Site C62 is known to contain unexploded ordnance.) At Site 1 no foreign objects were found, but at Site 2 a length of wire and some metal fragments were located and removed. Site 2 also contained a segment of steel rebar that had been buried in a vertical orientation for use as a fiducial marker. That rebar was temporarily removed during our measurements and later returned to its original location.

We next dug an access trench to permit a steel rod to be inserted into each test area as shown in Figure 5. The target rod was 3 meters long with a 0.875-inch diameter. The access trench was located adjacent to the midline of each test area and had a depth of approximately 5 feet.

For each of the two sites, seven separate scans were performed as indicated in Table 1. The first scan was performed prior to inserting the test rod. The radar path was perpendicular to the axis of the (absent) rod. After this initial work, the steel rod was inserted at a depth of three feet. With the rod inserted, the GPR was scanned over the rod twice: first through the centerline of the rod and a second time offset from the center away from the access trench. Hereafter we refer to these scans as “centered” and “offset”, respectively. The offset path is offset approximately three feet from the rod’s centerline in the direction away from the trench. The rod was then removed and re-inserted at a depth of two feet. The centered and offset scans were repeated. Finally, the centered and offset scans were repeated for the rod at one foot depth.

(Note the use of decreasing target depth to avoid disturbing the soil between the radar and the target.)

Table 1 GPR measurement scans taken at Eglin AFB.

Center Measurement Pass	Offset Measurement Pass
Rod at one-foot depth	Rod at one-foot depth
Rod at two-foot depth	Rod at two-foot depth
Rod at three-foot depth	Rod at three-foot depth
No Rod	

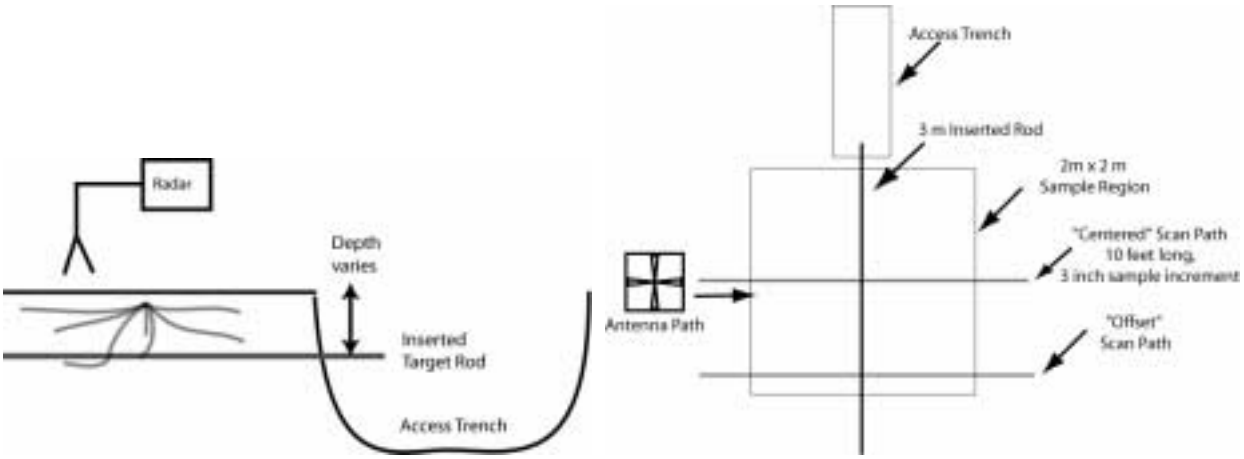

(a) Side view (b) Plan view

Figure 5 GPR measurement paths (not to scale).

2.2 Results

The GPR data was processed using software developed in Matlab to remove the "background" response (i.e., reflections from the antenna, cabling, and other components in the system). This was accomplished in the frequency domain by computing the average response over all 41 spatial positions, and subtracting that response from the entire scan. Examples of this "background-subtracted" data are shown in Figure 6, Figure 7, and Figure 8 for a scan over the center of the one-foot-depth rod at Site 2. A large amount of high frequency (>1.5 GHz) clutter appears in the S_{22} channel (see Figure 7) and, as noted above, the frequency domain data were truncated at 1.5 GHz to eliminate this clutter.

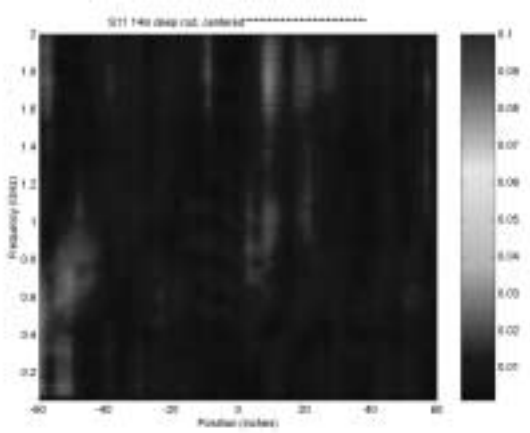

Figure 6 S_{11} Site 2, frequency-domain one-foot-depth rod, centered

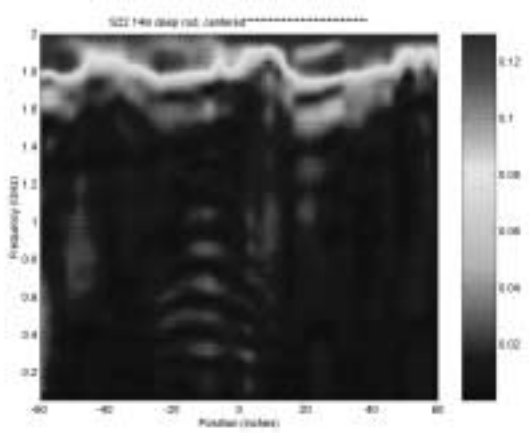

Figure 7 S_{22} Site 2, frequency-domain one-foot-depth rod, centered

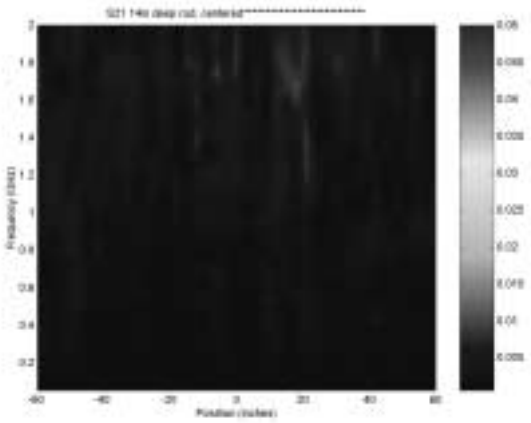

Figure 8 S_{21} Site 2, frequency-domain one-foot-depth rod, centered

The complete set of time-domain responses for Sites 1 and 2 are shown in Figure 9 through Figure 50 for the frequency band 50-1500 MHz. The response of the rod at three feet is shown in Figure 9 through Figure 20, the two-foot rod results appear in Figure 21 through Figure 32, and the one-foot rod results are found in Figure 33 through Figure 44. The response of the empty sites are presented in Figure 45 through Figure 50. The same amplitude scale is used in all figures.

The time of the surface return is approximately -6.5 ns in these Figures. To suppress strong near-surface returns, the first 6.5 ns of the time domain returns have been attenuated by a factor that varies linearly from –40 dB to 0 dB over the time interval 0 to -6.5 ns. (Data after 6.5 ns are not affected by this processing.) The soil dielectric constant at this location is roughly five (see Part 2 of this report), which implies a round-trip propagation velocity of 2.6 inches per nanosecond. From subsequent excavations of the site (described in Section 4), we know that the roots reside primarily at depths of less than 12 inches, which correspond to times of -6.5 to -11.1 ns.

The position of the rod is indicated by arrows in Figure 9 through Figure 12. The Site 1, center-scan data contain an artifact (a strong ringing that persists at all depths) near the -35 inch position. The source of that artifact is unknown, but is probably the result of scattering from a small piece of metal (e.g., a dropped screw) buried just below the surface at that location.

As an example of these data, consider the response of the rod at three-foot depths. The relevant data for Site 1 are found in Figure 9, Figure 13, and Figure 17. The arcs that appear in the time interval -20 to -30 ns at positions –30 to +40 inches are the back-scattered target response, which have the hyperbolic shape characteristic of a point scatterer. The S_{22} channel has the strongest response, since that antenna arm is co-polarized with the target rod. The response of the cross-polarized (S_{21}) channel is relatively weak. As expected, rods at shallower depths produce stronger responses.

The response of the roots appears to be weak and not easily characterized. There is little difference between the early-time (-6 to -10.6 ns) responses at Sites 1 and 2. The Site 1 data do show somewhat more scattering in the region occupied by the roots, but there are no clear isolated point-like scatterers. The early-time response at Site 1 is comparable for both polarizations, as one would expect for randomly oriented targets. Since early-time responses are also seen at Site 2, those returns might be attributed to antenna mismatch caused by the rough ground (i.e., randomly placed tufts of grass) or inhomgeneities in soil. The modeling analysis presented in Part 2 will offer evidence that these returns are due to the roots.

The cross-polarized (S_{21}) return offers perhaps the best visible indication of roots. The results show that while this component is weak, the cross-polarized early-time response for Site 2 is consistently weaker than the response from Site 1. This finding has a plausible physical explanation: since roots have a specific but random orientation, roots would tend to produce a random, but non-zero cross-polarized response.

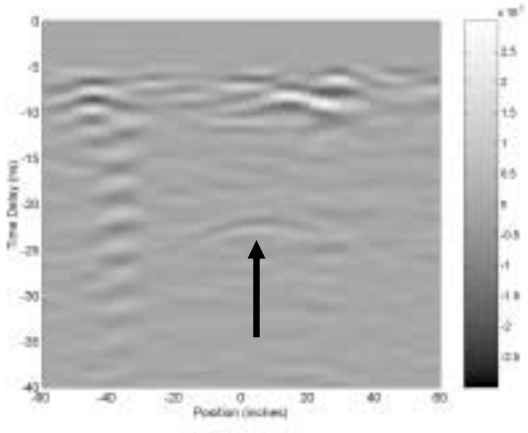

Figure 9 S_{11} Site 1, center scan of three-foot-depth rod .

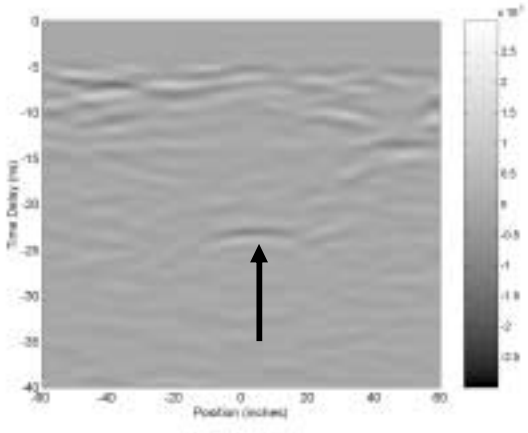

Figure 10 S_{11} Site 1, offset scan of three-foot-depth rod .

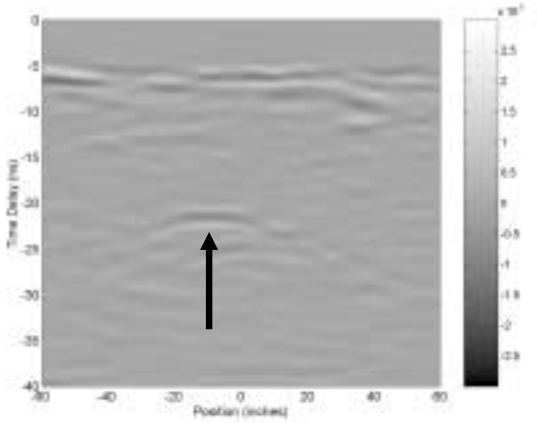

Figure 11 S_{11} Site 2, center scan of three-foot-depth rod.

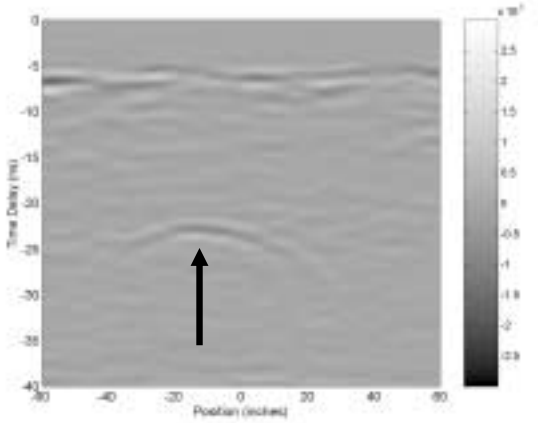

Figure 12 S_{11} Site 2, offset scan of three-foot-depth rod.

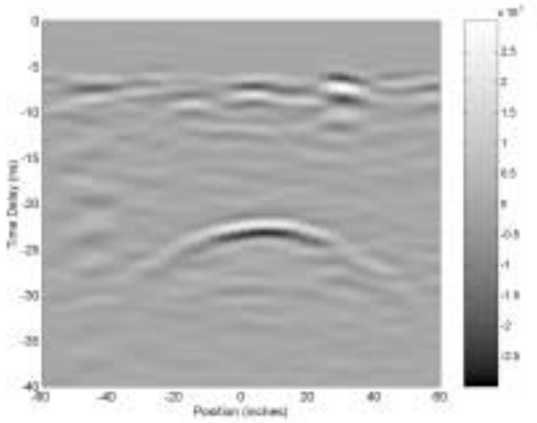

Figure 13 S_{22} Site 1, center scan of three-foot-depth rod .

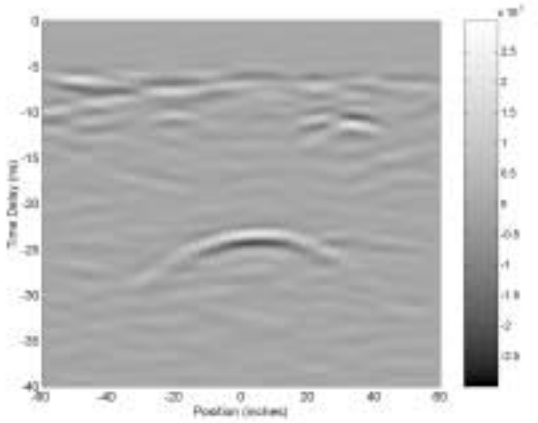

Figure 14 S_{22} Site 1, offset scan of three-foot-depth rod .

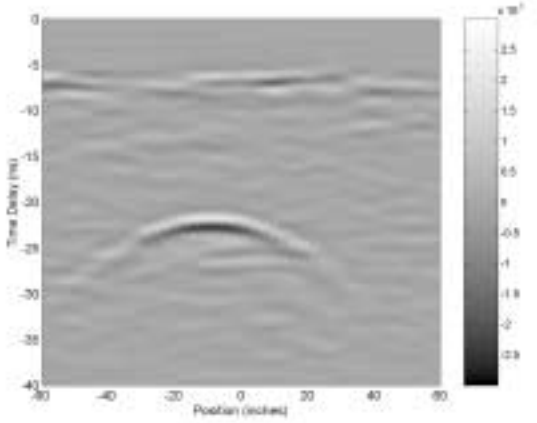

Figure 15 S_{22} Site 2, center scan of three-foot-depth rod .

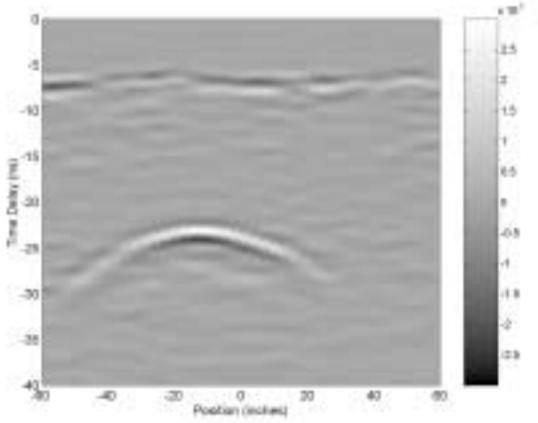

Figure 16 S_{22} Site 2, offset scan of three-foot-depth rod .

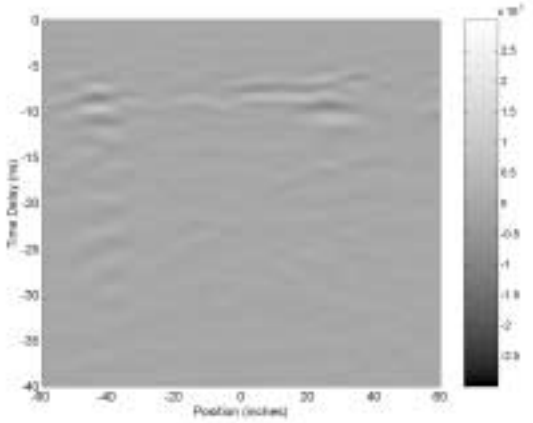

Figure 17 S_{21} Site 1, center scan of three-foot-depth rod .

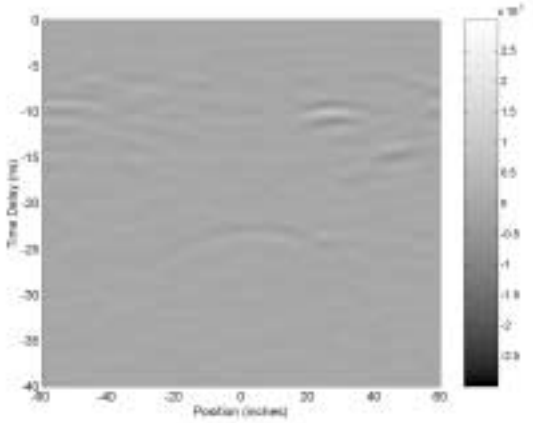

Figure 18 S_{21} Site 1, offset scan of three-foot-depth rod .

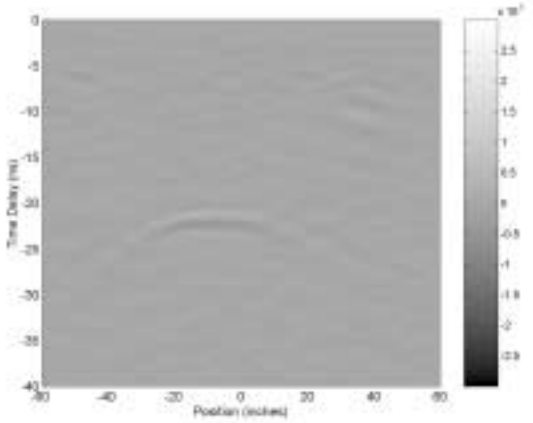

Figure 19 S_{21} Site 2, center scan of three-foot-depth rod .

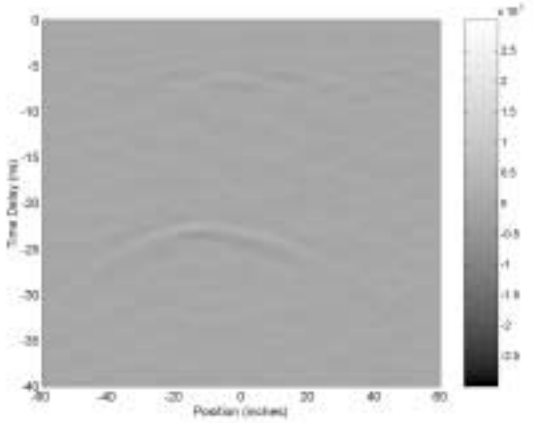

Figure 20 S_{21} Site 2, offset scan of three-foot-depth rod .

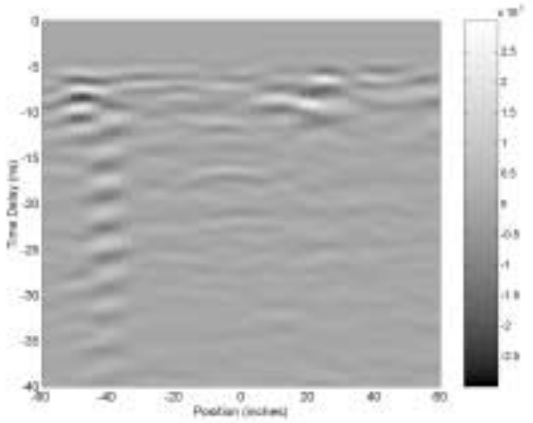

Figure 21 S_{11} Site 1, center scan of two-foot-depth rod .

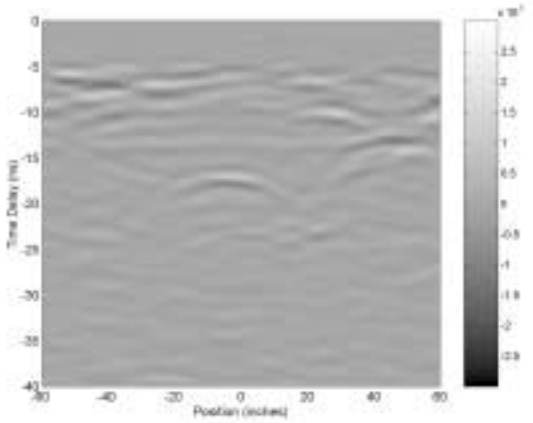

Figure 22 S_{11} Site 1, offset scan of two-foot-depth rod .

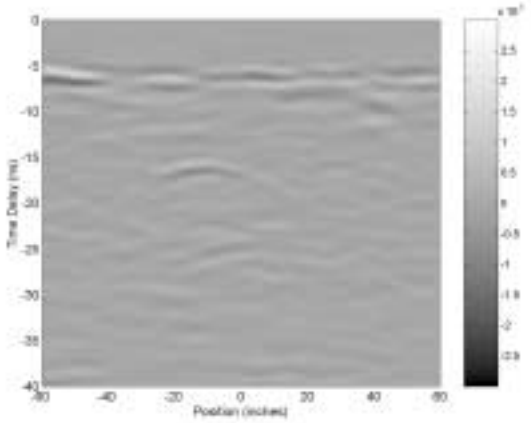

Figure 23 S_{11} Site 2, center scan of two-foot-depth rod .

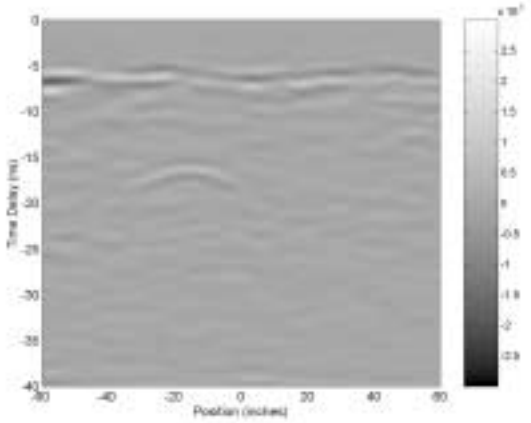

Figure 24 S_{11} Site 2, offset scan of two-foot-depth rod .

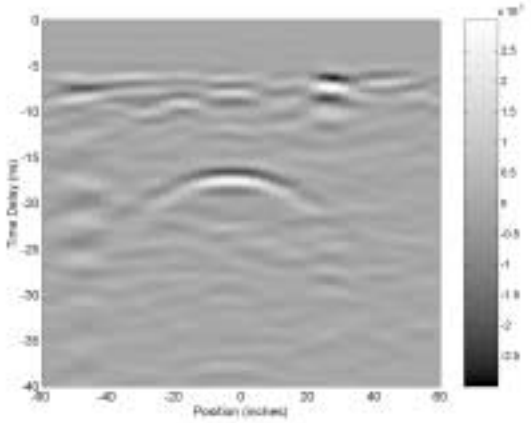

Figure 25 S_{22} Site 1, center scan of two-foot-depth rod .

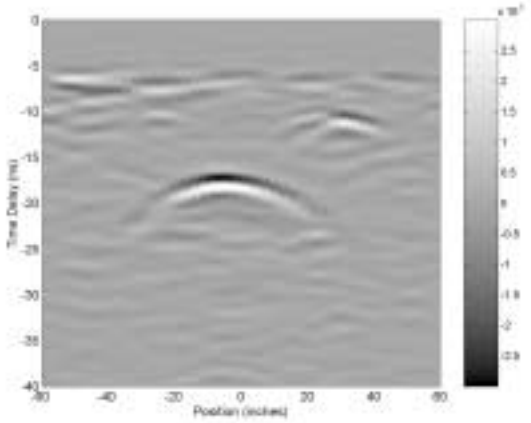

Figure 26 S_{22} Site 1, offset scan of two-foot-depth rod .

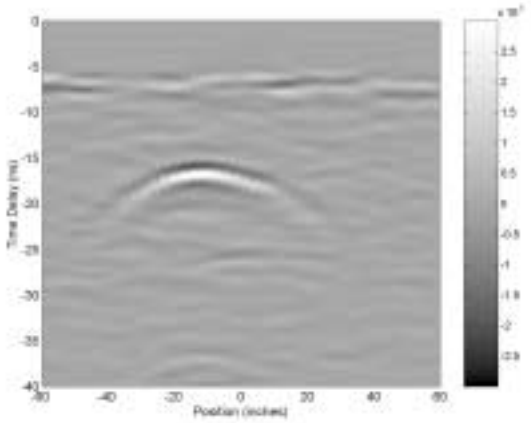

Figure 27 S_{22} Site 2, center scan of two-foot-depth rod .

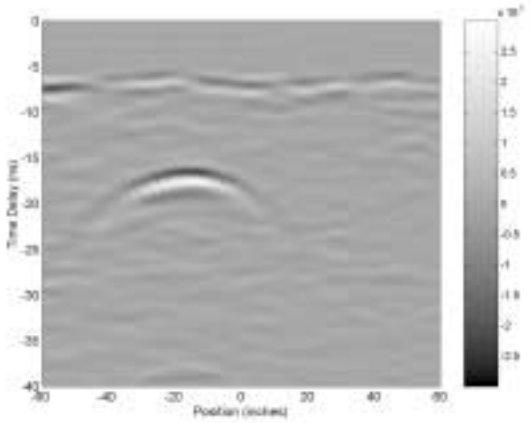

Figure 28 S_{22} Site 2, offset scan of two-foot-depth rod .

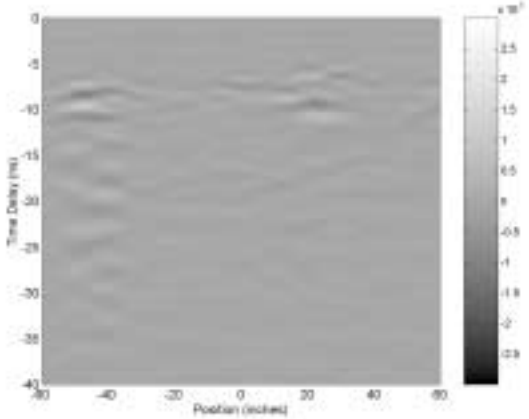

Figure 29 S_{21} Site 1, center scan of two-foot-depth rod .

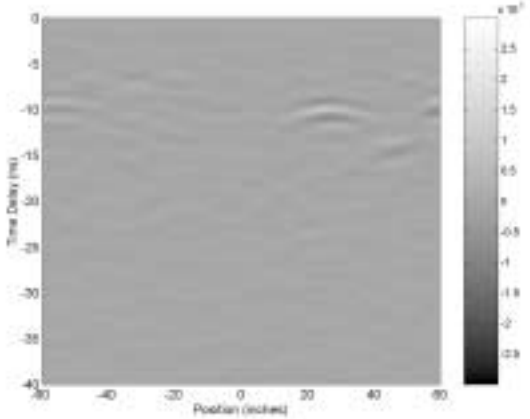

Figure 30 S_{21} Site 1, offset scan of two-foot-depth rod .

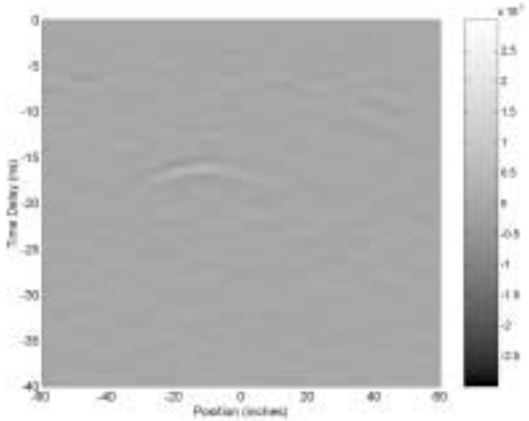

Figure 31 S_{21} Site 2, center scan of two-foot-depth rod .

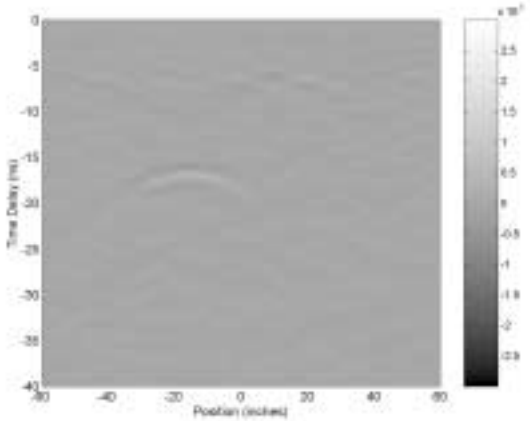

Figure 32 S_{21} Site 2, offset scan of two-foot-depth rod .

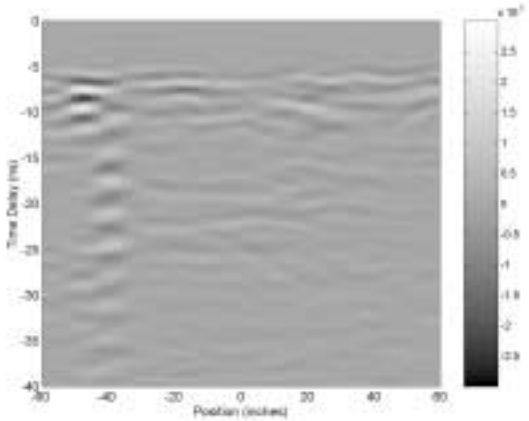

Figure 33 S_{11} Site 1, center scan of one-foot-depth rod .

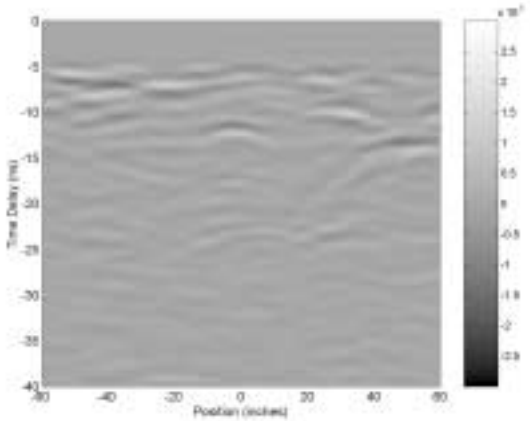

Figure 34 S_{11} Site 1, offset scan of one-foot-depth rod .

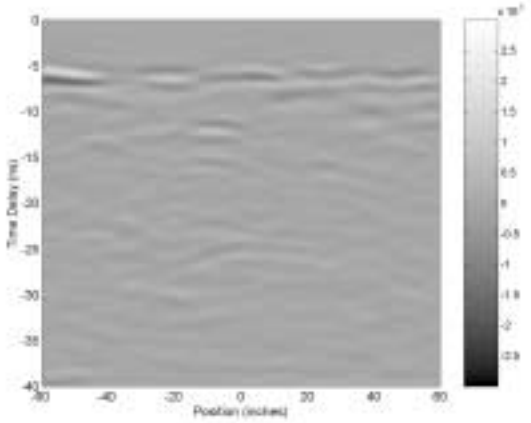

Figure 35 S_{11} Site 2, center scan of one-foot-depth rod .

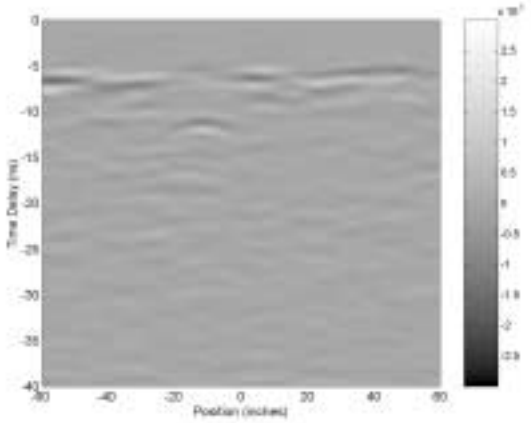

Figure 36 S_{11} Site 2, offset scan of one-foot-depth rod .

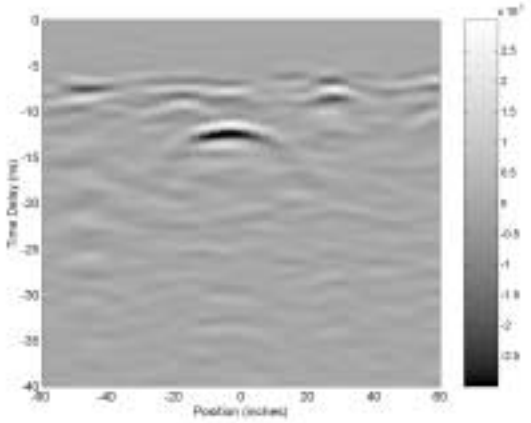

Figure 37 S_{22} Site 1, center scan of one-foot-depth rod .

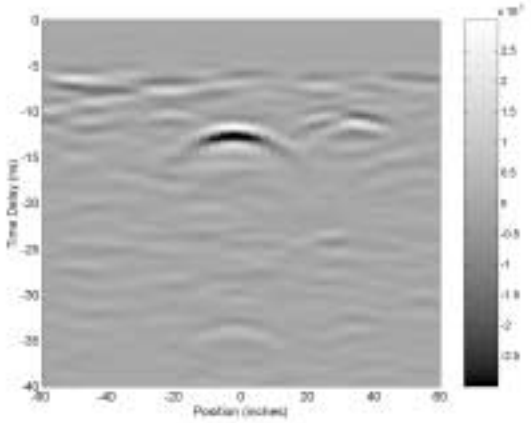

Figure 38 S_{22} Site 1, offset scan of one-foot-depth rod .

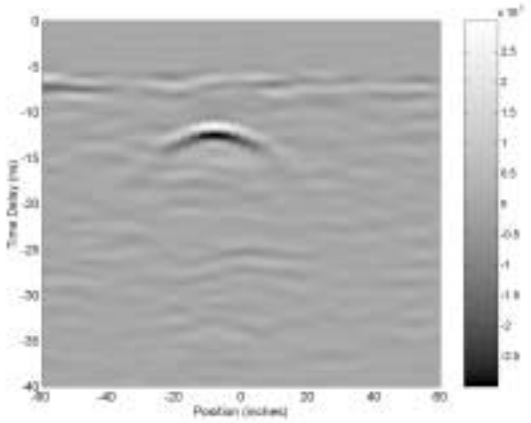

Figure 39 S_{22} Site 2, center scan of one-foot-depth rod .

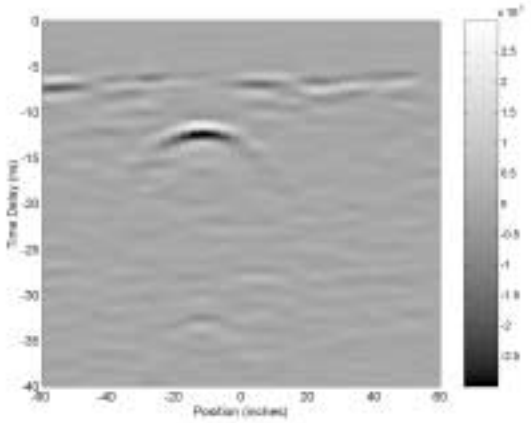

Figure 40 S_{22} Site 2, offset scan of one-foot-depth rod .

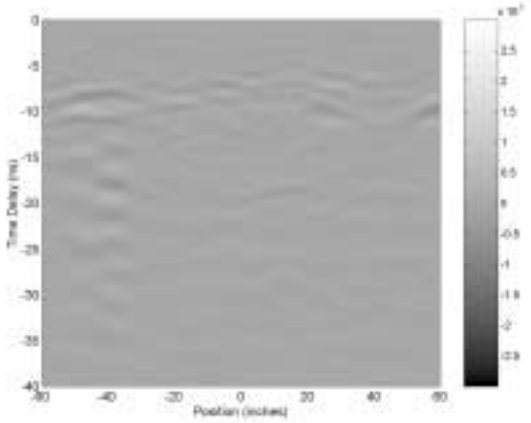

Figure 41 S_{21} Site 1, center scan of one-foot-depth rod .

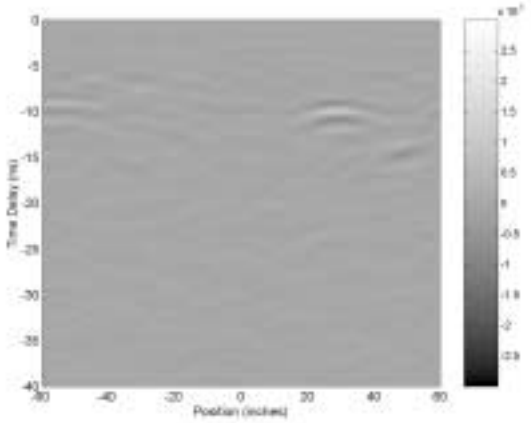

Figure 42 S_{21} Site 1, offset scan of one-foot-depth rod .

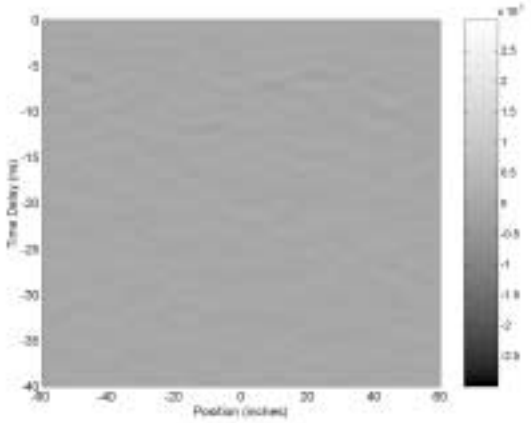

Figure 43 S_{21} Site 2, center scan of one-foot-depth rod .

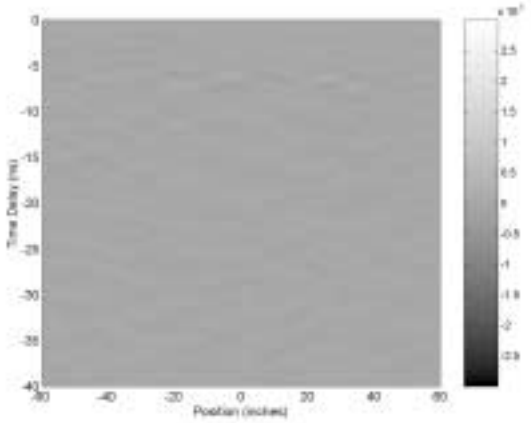

Figure 44 S_{21} Site 2, offset scan of one-foot-depth rod .

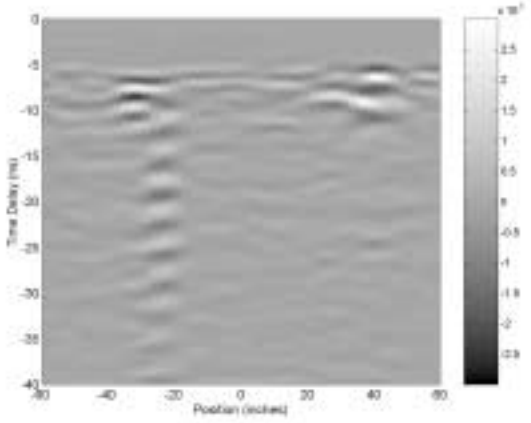

Figure 45 S_{11} Site 1, time-domain empty site

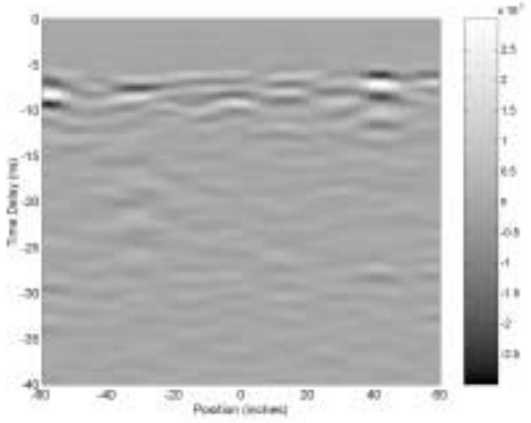

Figure 46 S_{22} Site 1, time-domain Empty Site

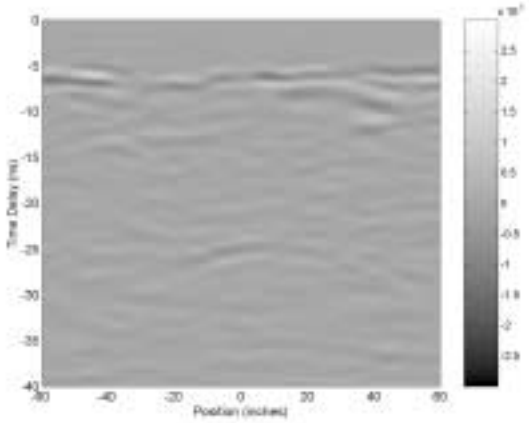

Figure 47 S_{11} Site 2, time-domain empty site

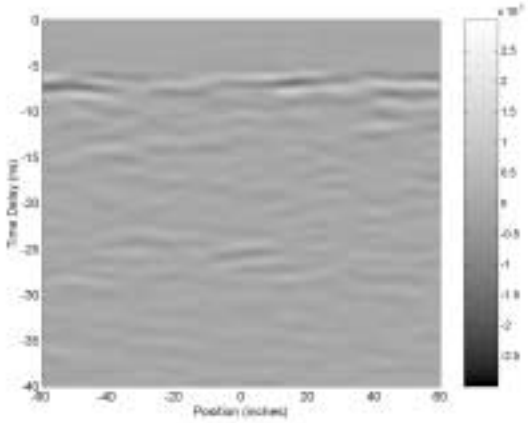

Figure 48 S_{22} Site 2, time-domain empty site

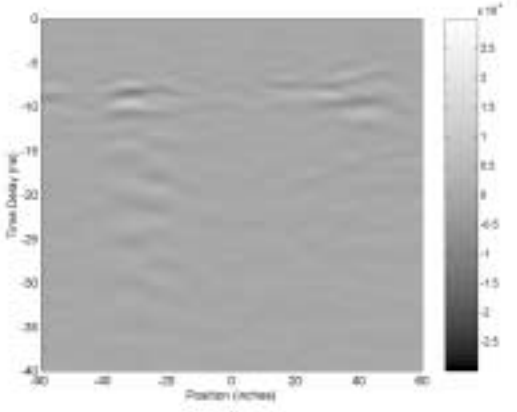

Figure 49 S_{21} Site 1, time-domain empty site

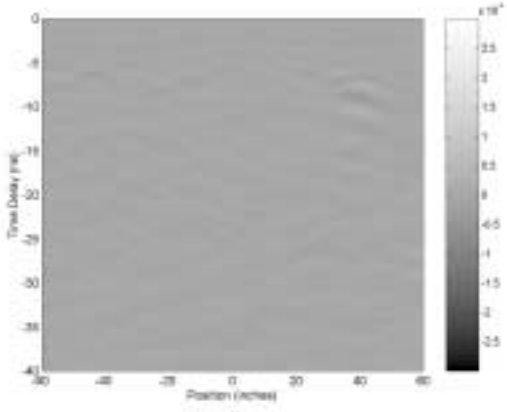

Figure 50 S_{21} Site 2, time-domain empty site

2.3 Statistical Characterization of Clutter

As noted above, the root response is not distinct in the measurements. To better characterize early-time clutter in these time-domain GPR returns, they were examined statistically. In this effort the 41 time-domain returns for the S_{11}, S_{21}, and S_{22} channels over the interval from 6 ns (ground surface location) to 13.5 ns were treated as realizations of stochastic processes. The standard deviations of these returns (also time functions) were then computed. The implicit assumption here is that scattering from randomly placed roots would tend to produce higher standard deviations at depths where they were present. The calculation was repeated for the empty site, the two-foot-depth rod, and the three-foot-depth rod. The one-foot-depth data was not used because the target response begins at approximately 11 ns and would interfere with the distribution. The standard deviations of the S_{11}, S_{22}, and S_{21} channels are shown in Figure 51, Figure 52, and Figure 53, respectively. As noted previously, the surface scattering appears at roughly time=6.5 ns. The frequency range used for the plots was 0.05-1.5 GHz. It is interesting to observe that the standard deviation values corresponding to the top 12 inches of soil (i.e., prior to t=12 ns) are higher in magnitude for Site 1 (the high root density site) than for Site 2 (the low root density location) by 6 to 12 dB for all polarizations. As noted above (and shown in Section 4) the roots are found overwhelmingly in the top 12 inches of soil and, hence, the increased clutter is evidence for root scattering.

An analysis of scattering in various frequency bands revealed that the largest difference in the Site and Site 2 scattering standard deviations occurs between 250 and 750 MHz, as shown in Figure 54 through Figure 56. At lower frequencies the dimensions of the roots are probably too small to cause significant scattering. At higher frequencies, increased soil absorption reduces the penetration depth, making the radar insensitive to the roots. The standard deviation curves for lower and higher frequency bands appear in Figure 57 through Figure 62. It is worth noting that the largest percentage changes (and the weakest signal levels) occur for the cross-polarized results.

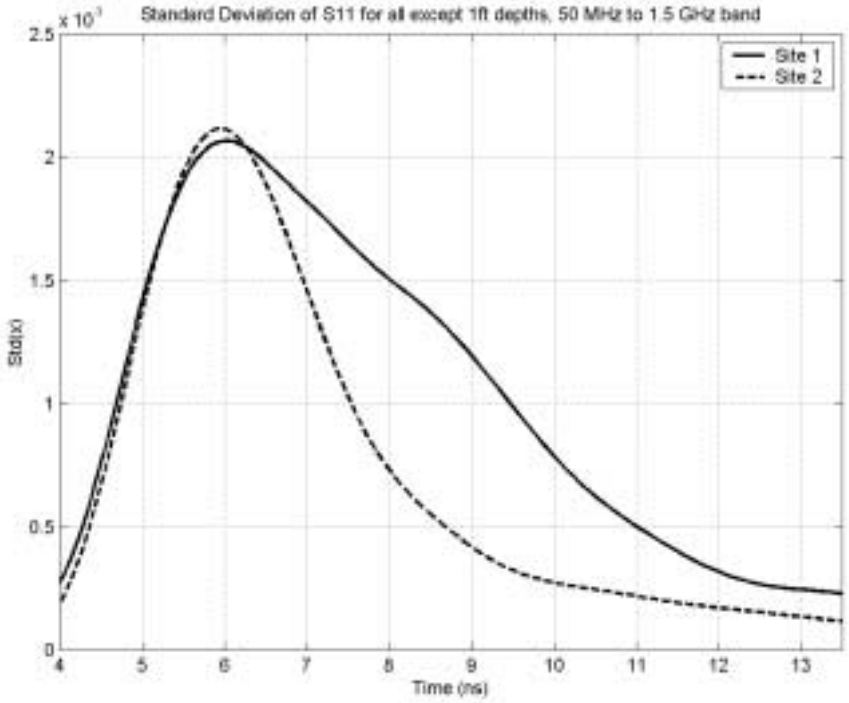

Figure 51 S_{11} Standard deviation for the full band (50 to 1500 MHz)

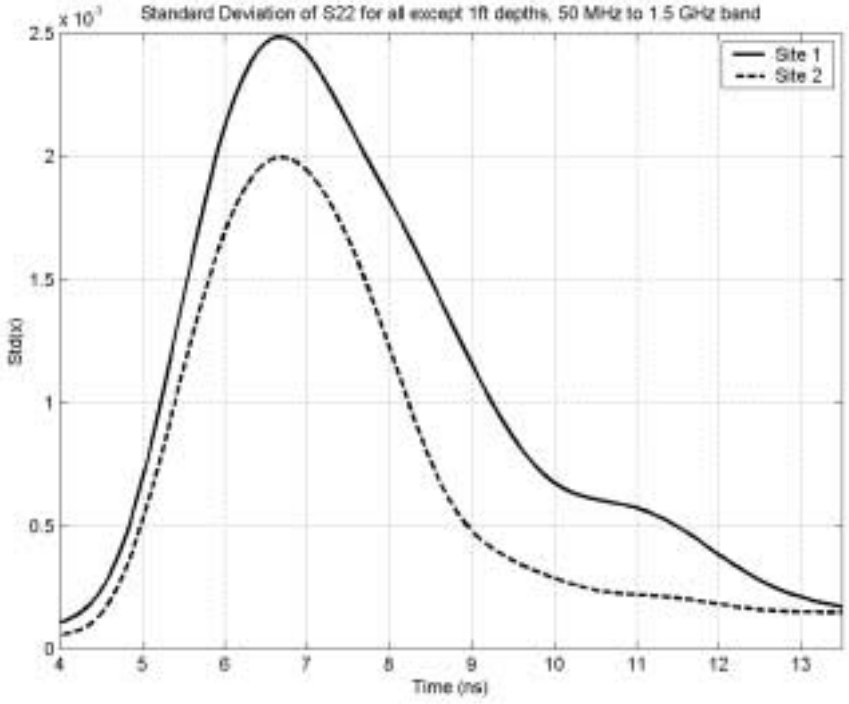

Figure 52 S_{22} standard deviation for the full band (50 to 1500 MHz)

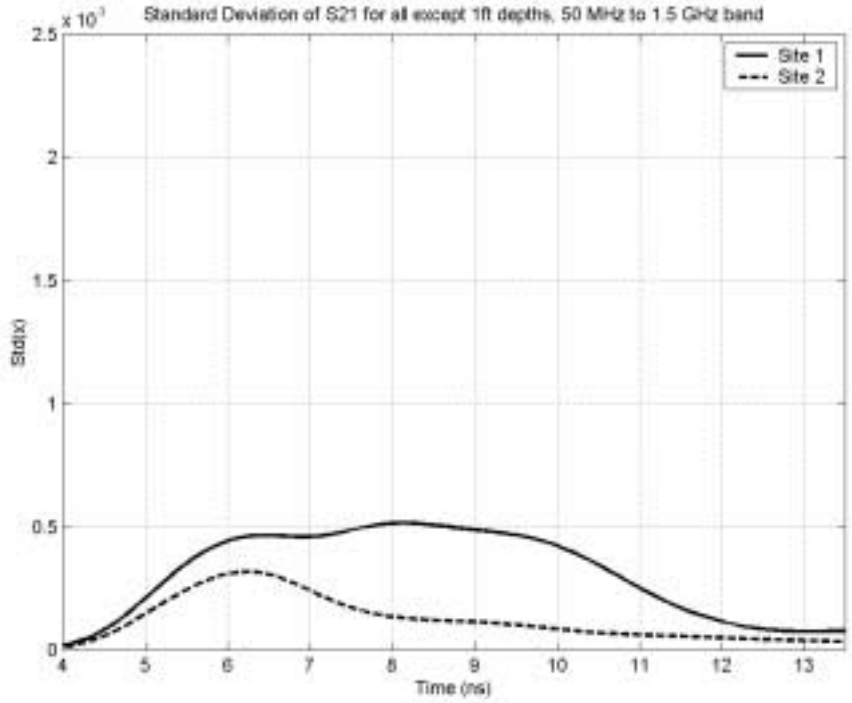

Figure 53 S_{21} standard deviation for the full band (50 to 1500 MHz)

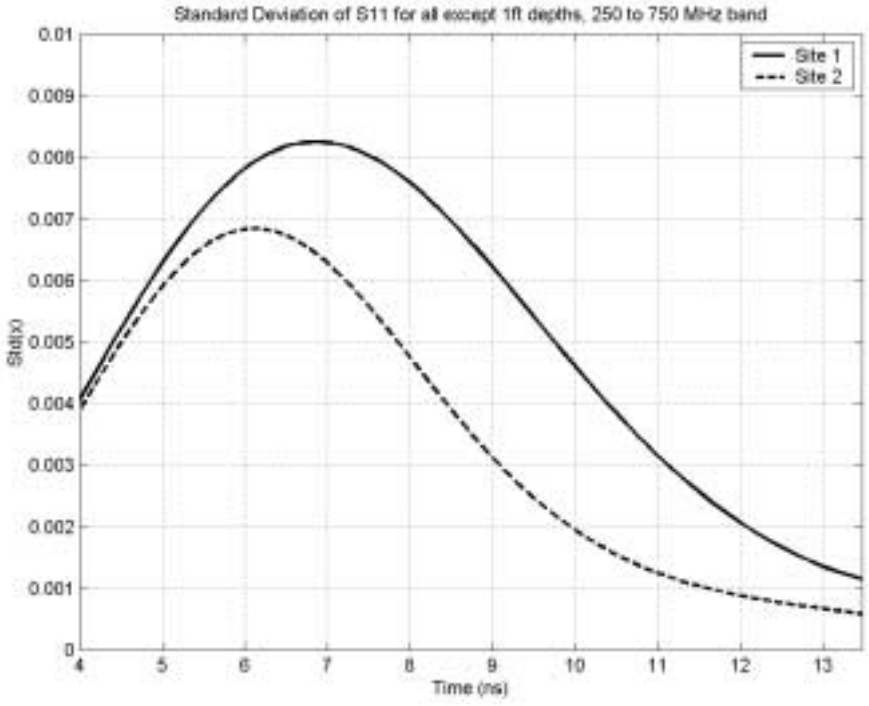

Figure 54 S_{11} standard deviation for the band 250 to 750 MHz

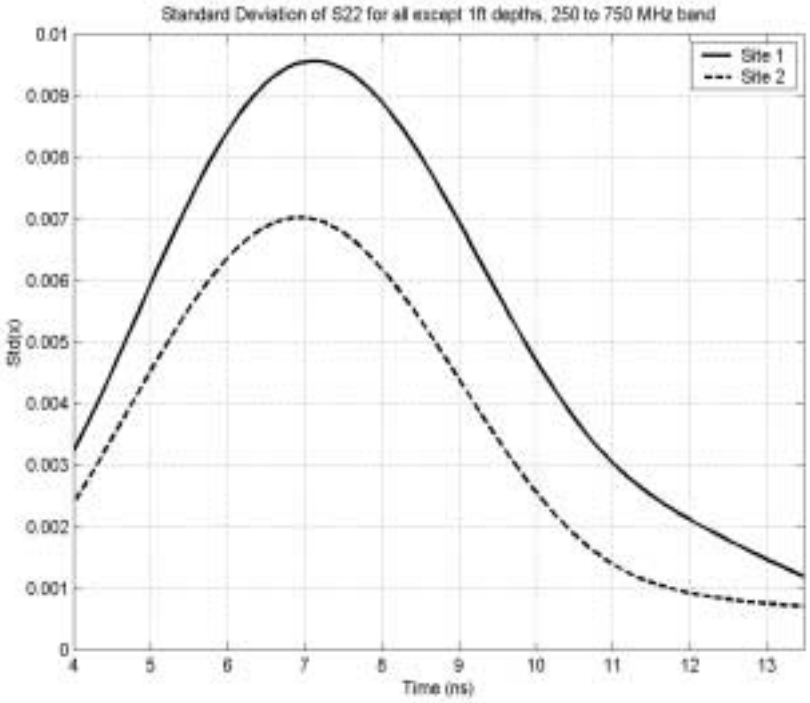

Figure 55 S_{22} standard deviation for the band 250 to 750 MHz

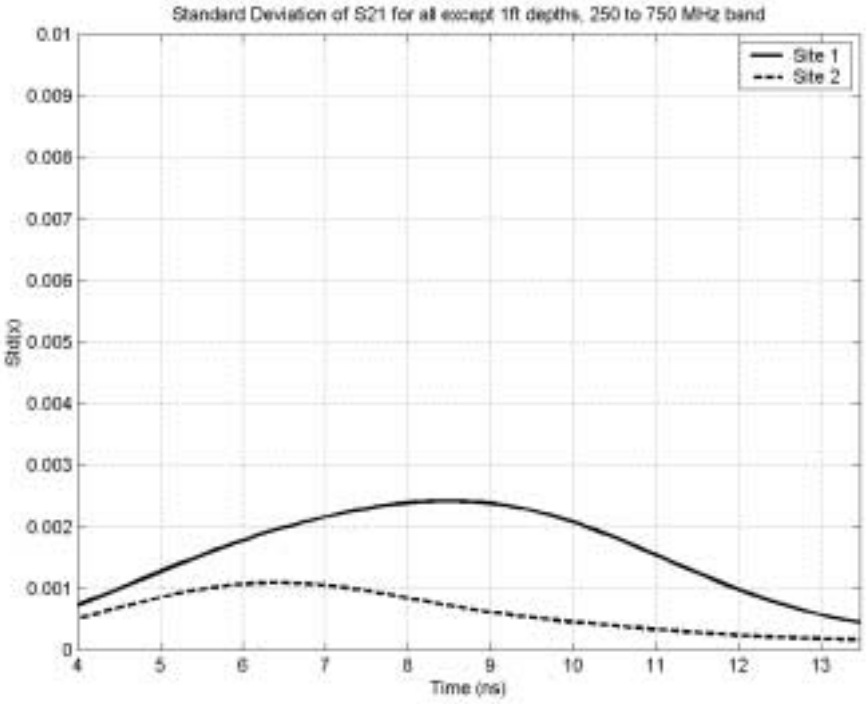

Figure 56 S_{21} standard deviation for the band 250 to 750 MHz

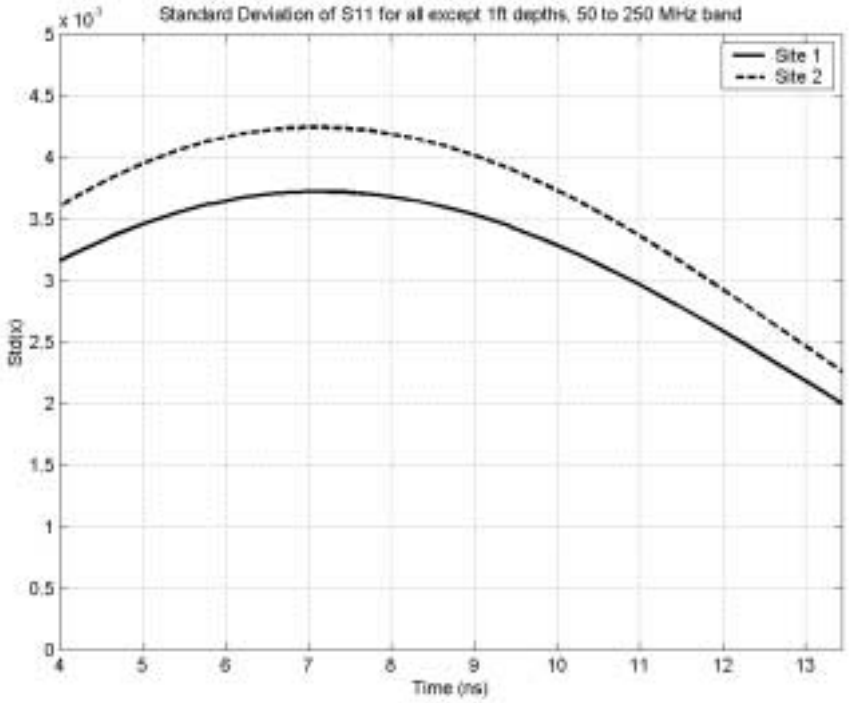

Figure 57 S_{11} standard deviation for the band 50 to 250 MHz

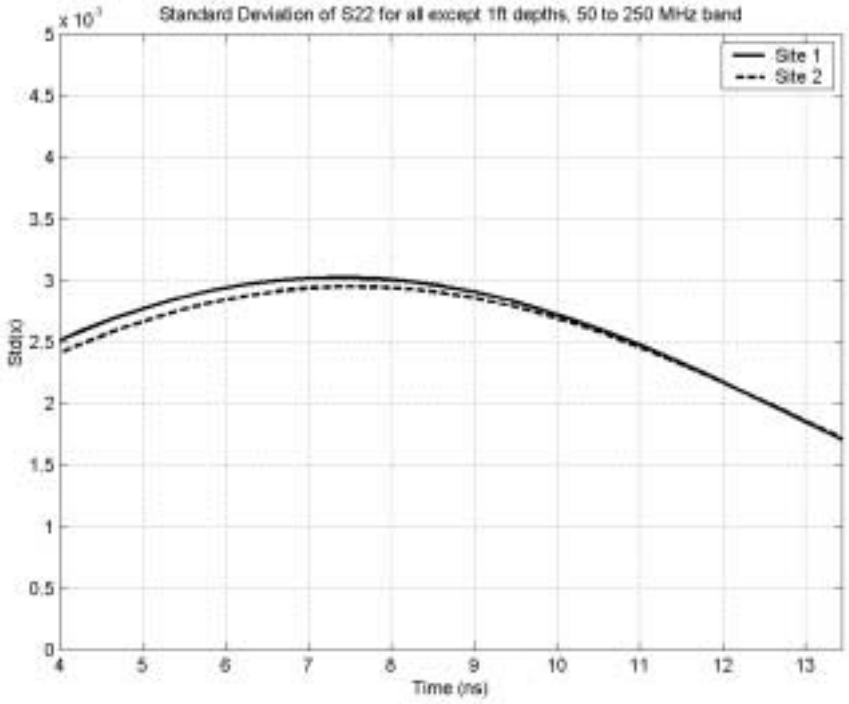

Figure 58 S_{22} standard deviation for the band 50 to 250 MHz

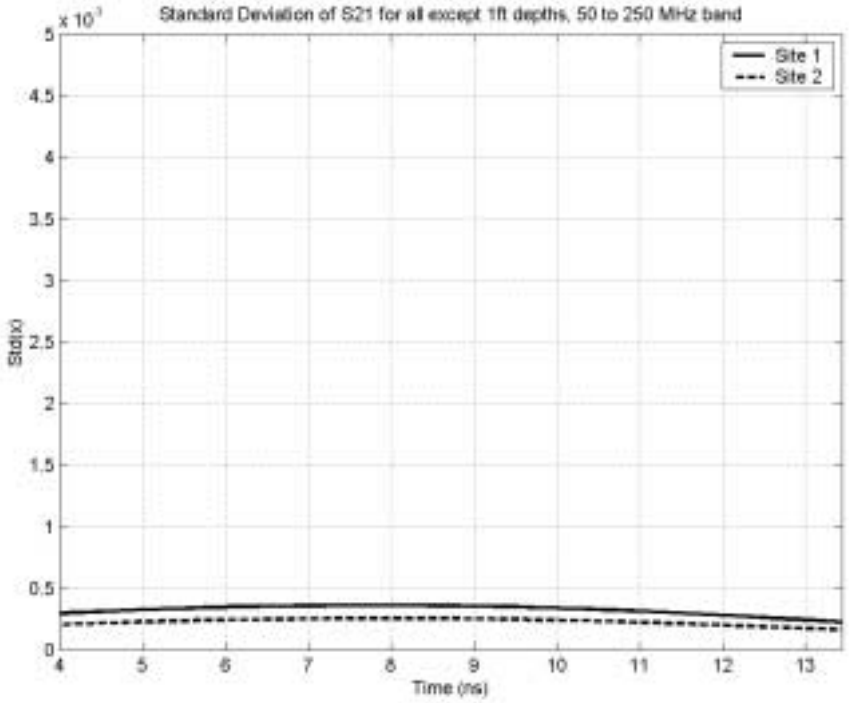

Figure 59 S_{21} standard deviation for the band 50 to 250 MHz

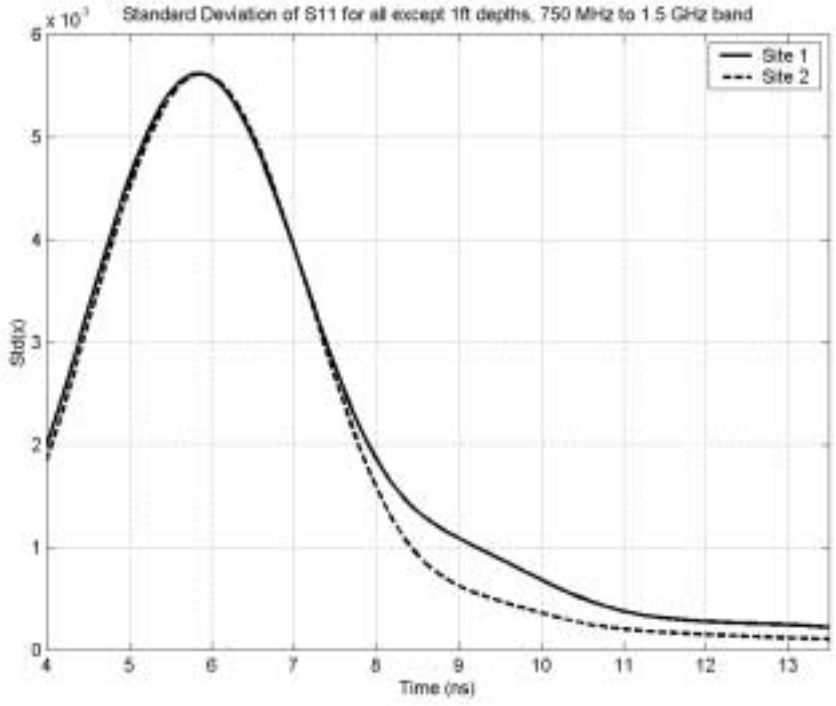

Figure 60 S_{11} standard deviation for the band 750 to 1500 MHz

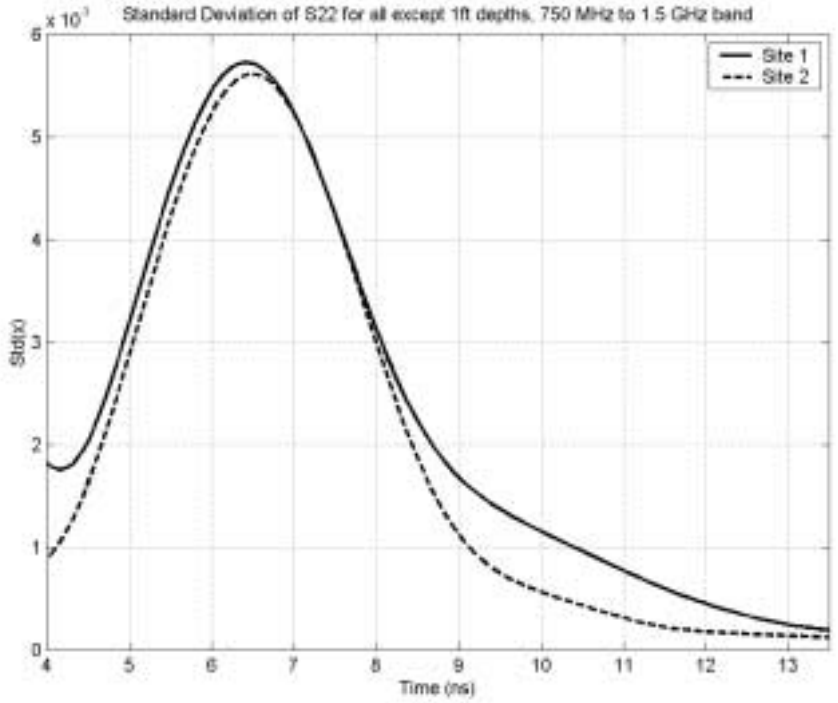

Figure 61 S_{22} standard deviation for the band 750 to 1500 MHz

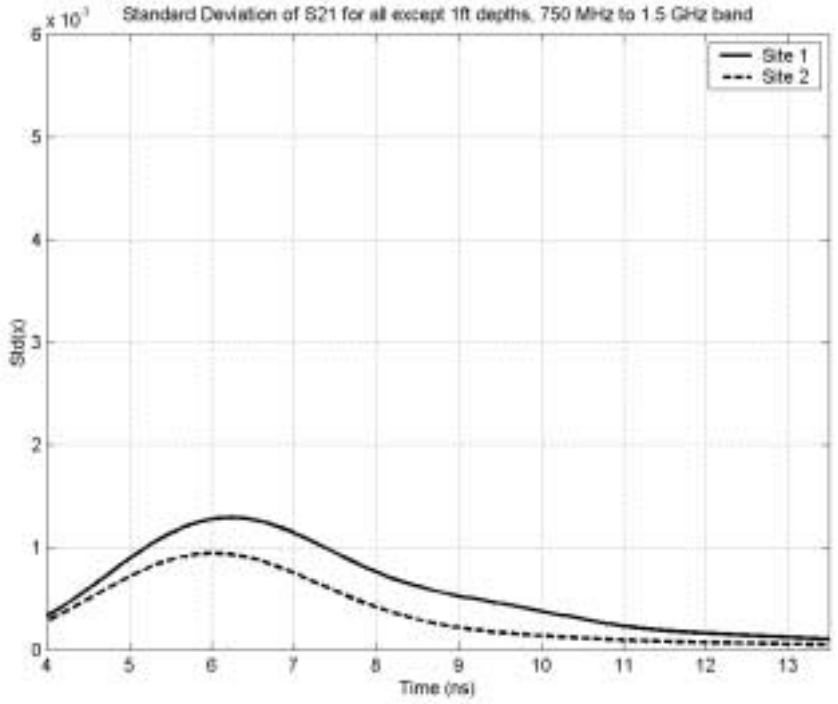

Figure 62 S_{21} standard deviation for the band 750 to 1500 MHz

3.0 Surface Scattering Measurements from Elevated Horn

Near-surface roots could produce surface clutter that would be visible to a radar using an elevated antenna. For a radar that views the ground at an oblique angle, surface clutter cannot be separated from clutter at depth, which makes it particularly troubling and a possible source of confusion. We performed experiments to characterize surface clutter at the Eglin site prior to the ground-contacting measurements described in Section 2. Because of the logistical difficulties of fielding an elevated radar, the scope of this effort was limited. In this section we review the procedure used in those measurements and the results obtained.

3.1 Measurement Setup

A commercial RF vector network analyzer (HP8753C) and a standard horn antenna (AEL model H-1734) were used for collecting reflection (S_{11}) data over the frequency band from 0.05 to 2.0 GHz. Both parallel and perpendicular polarization data were collected, but no cross-polarized returns were acquired. The antenna was attached to the end of a wood 4x4 beam and placed on the roof of a rental truck, as shown in Figure 63. The relevant dimensions are shown in Figure 64. The radar control and data collection was done from a laptop computer located inside the truck. Stepped-frequency data were collected from 0.05 to 2.0 GHz with 401 steps and a step size of 4.875 MHz. The IF bandwidth was set to 300 Hz, and the system power level was set to 0 dBm.

Figure 63 Surface scattering measurement setup with calibration sphere.

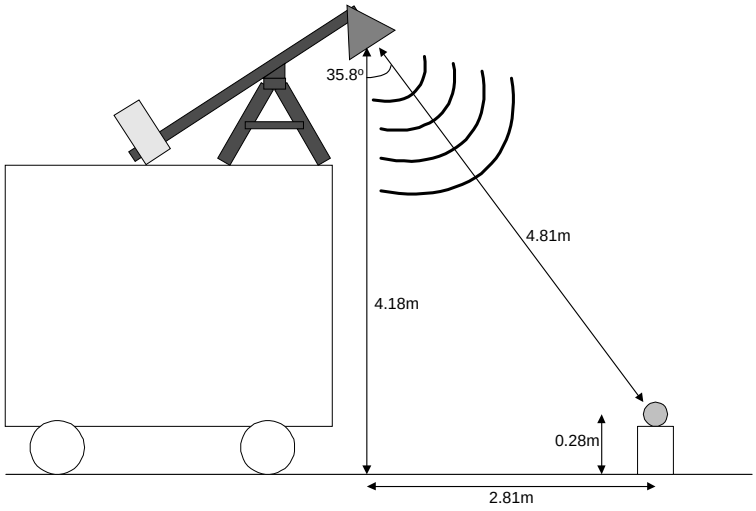

Figure 64 Dimensions relevant to the surface scattering measurement.

These data were calibrated using a 4-inch diameter conducting sphere placed on a 9-inch high Styrofoam stand and positioned on the horn's boresight. In addition to this calibration measurement, a "background" measurement was also made with the horn pointed to the sky. The latter measurement provides an estimate of the system response, which was used in subsequent processing.

At both Site 1 and Site 2 four frequency-swept measurements were performed: the parallel-polarization response of the empty site, the perpendicular-polarization response of the empty site, the parallel-polarization response of a calibration sphere, and the perpendicular-polarization response of a calibration sphere.

3.2 Results

The surface scattering data were processed to remove the system response by subtracting the background (sky) measurements. The data were then transformed to the time-domain. Time t=0 corresponds to the horn input connector. From Figure 64 we see that the first reflection from the ground appears at t=27.9 ns. Returns prior to this time may be contaminated by changes in the background, which included cable motion occurring when the operator got in and out of the truck to remove the calibration sphere. A linearly decreasing attenuation (from –40 dB to 0 dB) was applied to the first 20 ns of the results shown in the following plots to emphasize the surface scattering phenomena.

The background-subtracted sphere returns (i.e., sphere – no sphere data) are shown in Figure 65 and Figure 66 for parallel and perpendicular polarization, respectively. The sphere response is the peak observed between 32 and 33 ns. The empty site, i.e. no sphere, measurements for Site 1 and Site 2 are shown in Figure 67 and Figure 68.

The results do not show a clear difference between the sites, and we believe that they are generally inconclusive. There is a large difference in the early-time perpendicular polarization return of Figure 66, which we attributed to the aforementioned cable motion. The remaining results do not show a clear difference between the two sites. Between 45 and 55 ns the

magnitude of the reflected signal from Site 1 is approximately 5 dB above the signal from Site 2, but that factor is not consistent over a larger time interval. A larger sample size will be required before a definitive assessment of surface scattering can be done.

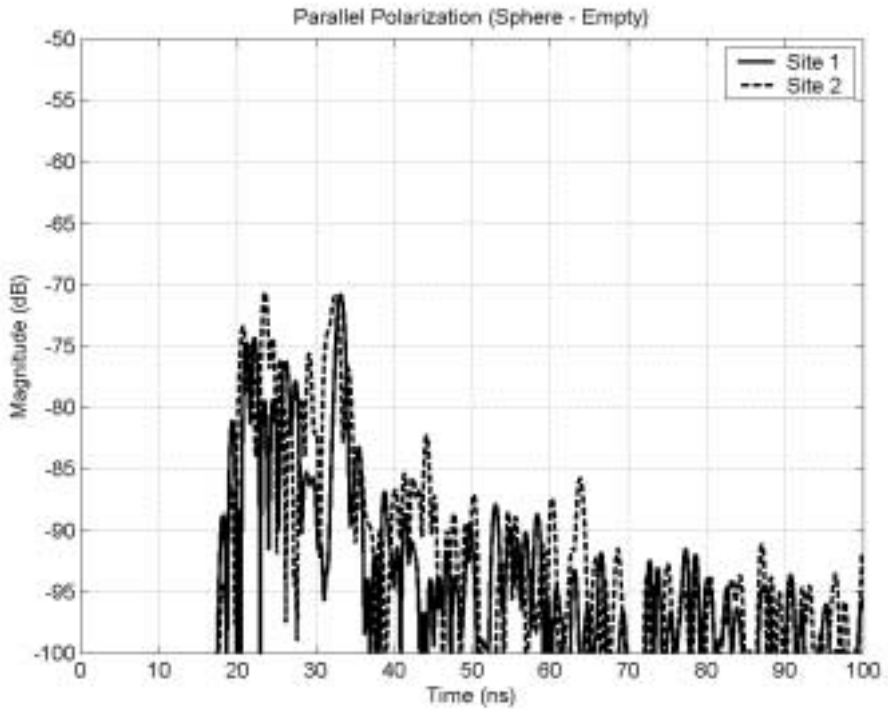

Figure 65. Background-suppressed data (i.e., sphere – no sphere) for the parallel polarization plotted in the time-domain for the frequency band 50 – 2000 MHz.

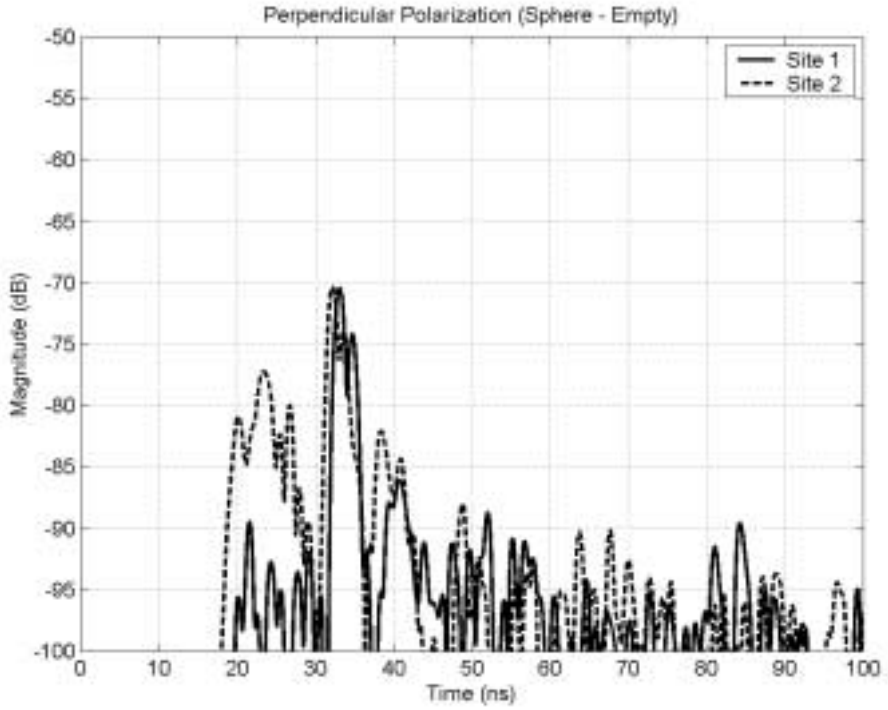

Figure 66. Background-suppressed data (i.e., sphere – no sphere) for the perpendicular polarization plotted in the time-domain for the frequency band 50 – 2000 MHz

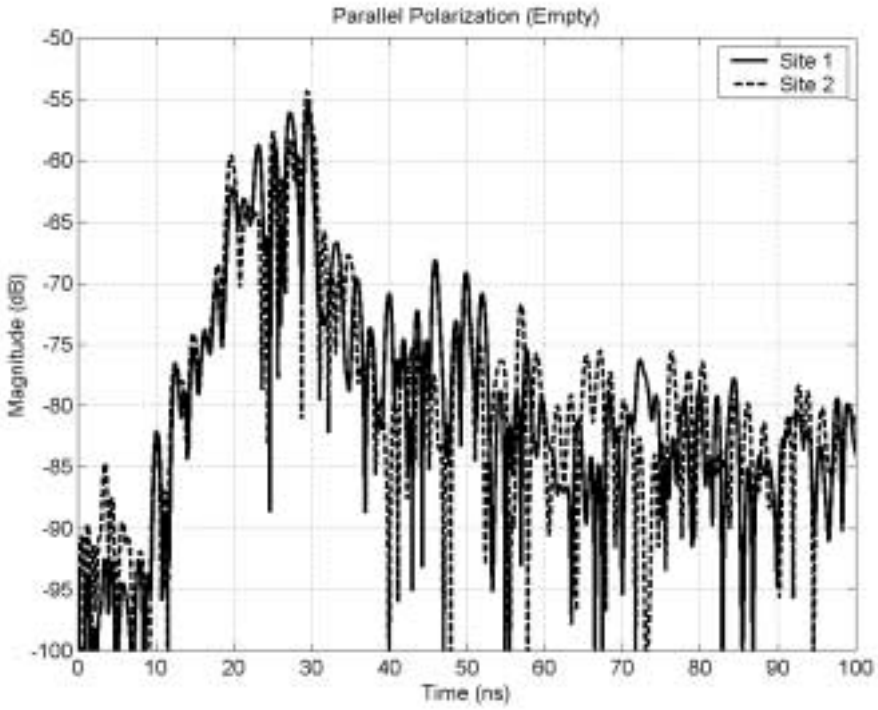

Figure 67 Parallel polarization return for the empty site (50 – 2000 MHz)

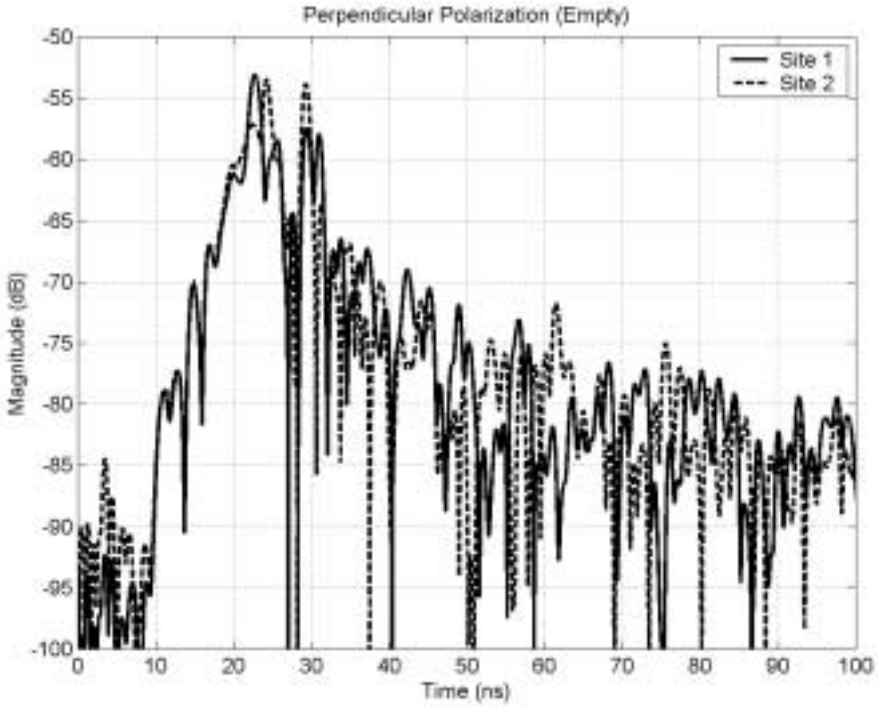

Figure 68 Perpendicular polarization return for the empty site (50 – 2000 MHz)

4.0 Supplemental Measurements

In addition to the scattering measurements documented in Sections 2 and 3, measurements of various site characteristics were made. In this section we document those measurements.

4.1 Root Structure and Properties

After completing all radar measurements, Sites 1 and 2 were excavated to a depth of 24 inches. Care was taken to preserve any roots found. Figure 69 shows the root structures found at Sites 1 and 2. In both cases the roots have been painted red to increase their photographic contrast. It is evident that there are essentially no roots present at Site 2. Since the sample locations had to be chosen prior to their excavation, this finding was a welcome discovery. It also suggests that surface shrub density is a good predictor of subsurface density.

(a) Site 1 (b) Site 2

Figure 69. The test sites after excavation to a depth of 24 inches. The roots were left intact and painted red for better visibility. String lines mark 1 meter square sections

Several features of the roots at Site 1 require additional discussion. A number of overlapping photos of that location were taken, and the results were ortho-rectified to produce the plan-view image shown in Figure 70, in which the image distances approximate the true plan distances. The large root mass shown near the center of the figure was not evident from the surface, but it was probably the nucleus of a vigorous shrub. Roots radiate from it in essentially all directions. That object, which is approximately 10 cm in diameter, comprises the largest object seen in our study, and it features prominently in the analysis in Part 2 of this report. Unfortunately, as indicated in the figure, the GPR scan did not traverse the large root mass. (The "centered" scan path is shown. The "offset" path would be below the bottom edge of the image.)

The entire root structure shown in Figure 70 was exhumed and returned to our Laboratory for additional study. Root diameters were measured, and a histogram of the results (normalized per unit length) appears in Figure 71. Very small roots were common, but did not survive excavation and are unlikely to affect the GPR measurements. The distribution suggests a modal diameter of about 1.5 cm. Several root samples were also excavated and immediately sealed for further analysis.

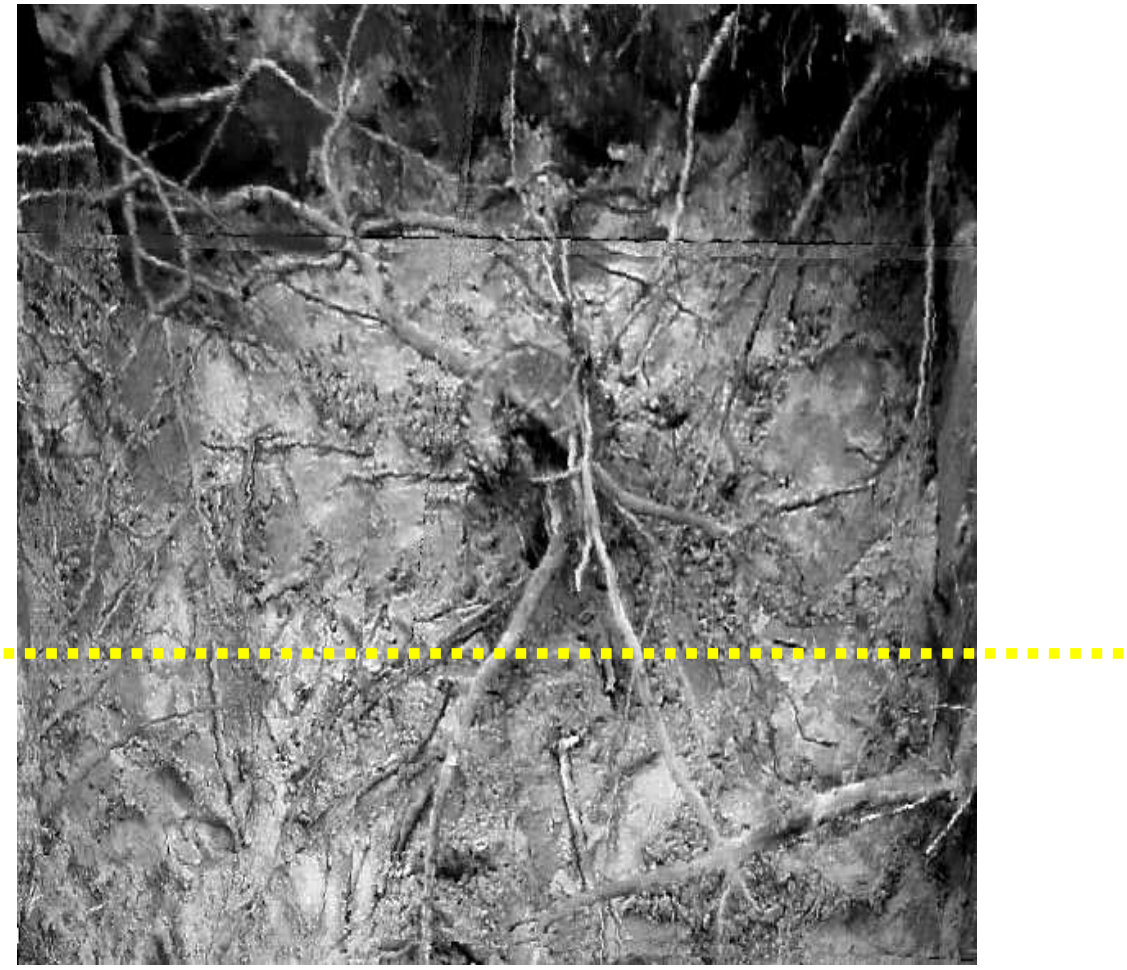

Figure 70. Top view of the root distribution at Site 1. The approximate radar path is shown by the dashed line.

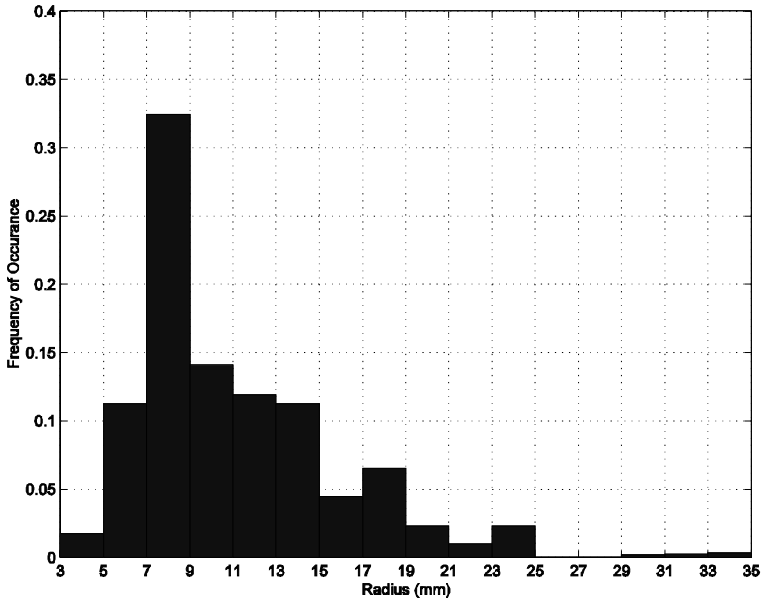

Figure 71 Histogram of root diameters.

Soil samples were obtained every six inches to a depth of three feet. Those samples were double-bagged in sealed plastic bags and returned to our facility for moisture measurements and dielectric property measurements. Results of those measurements appear in Part 2 of this report. The local soil was very sandy, but the top surface had a somewhat different composition. Figure 72 shows that roughly the top six inches of soil has a markedly darker color than the deeper soil, possibly as a result of decayed organic matter.

Figure 72. Near-surface soil shows darker color than deeper soil.

4.2 Shrub density.

Finally, the spatial density of shrubs in the region of our experiments was measured. A total of six 30 foot square regions (arranged as a 2x3 grid) were marked, and the shrubs within those areas were counted. The counts appear in Table 2, which shows a mean density of one shrub per 30.5 square feet, or a mean distance of 5.5 feet between shrubs.

Table 2. Shrub counts for adjacent 30 foot square regions.

Region	Count
1	**25**
2	**21**
3	**40**
4	**26**
5	**39**
6	**26**

5.0 Summary and Conclusions

A combination of experiment and theory was used to study scattering from buried roots. In this document, we present the experimental aspects of the work. A number of measurements were performed by the Ohio State University ElectroScience Laboratory (OSU ESL) at Site C62, Eglin AFB, FL. Wideband, multi-polarization GPR measurements were made with a radar that uses a ground-contacting antenna. The frequency band examined in this work was 50-2000 MHz, although unexpected clutter in one polarization forced us to use only results below 1500 MHz.

Some interesting results were gleaned from time-domain ("waterfall") plots of the radar output as it is scanned over sites with and without roots. A comparison of the co-polarized returns for sites with and without roots showed very similar phenomena, including scattering from largely random objects in the top foot of soil. These scattering events were weaker than the return from a steel rod inserted into the site from a distant access trench. A statistical analysis of the returns showed that the site with roots had a generally higher clutter level than the site without roots. The difference between the sites is perhaps most evident for the cross-polarized returns. Sites with roots produce a significantly more cross-polarized return than sites without roots. The statistical analysis confirmed this finding. For both co-polarized and cross-polarized returns, root clutter was found to be strongest in the frequency band from 250 to 750 MHz.

Measurements of surface clutter were also made using an elevated antenna. Because of the difficulty of fielding an elevated radar, the scope of those measurements was limited. An analysis of the results yielded no obvious difference, but it is difficult to draw compelling conclusions from them because of the small data set (only two sites were examined.)

Additional investigation of this scattering from biomass appears in Part 2 of this report. In that document we describe a numerical model developed by OSU and capable of predicting many of the results shown herein.

Appendix: File Formats

GPR data files

The data for system-calibrated frequency-domain radar data was stored in binary files that use the naming convention "`aydddaa.cdt`", where "`a`" is a letter in the range a-z used for file ordering. The letter "`y`" indicates the last digit of the year. For example, "0" represents the year of 2000. The three-digit number, "`ddd`" , indicates the Julian date when the data was stored. Each file contains two-dimensional (space and frequency) data taken at multiple target locations. Frequency responses are stored column-wise with the first frequency (10 MHz) stored in the first row, the second frequency (12 MHz) data stored in the second row, etc. Table 3 illustrates the new format of multiple GPR data. Data collected at each position is contained in one vertical block that comprises six columns corresponding to the real and imaginary parts of S_{11}, S_{21} and S_{22}, respectively, as illustrated in Table 4. For each radar file, "`*.cdt`", there is an associated comment file called "`*.txt`" to store the system information and comments. There is also an associated processed file called "*.mat" file that stores the processed results and all processing parameters. All of these files are available upon request.

Table 3 Format for multiple-position GPR data.

Data(f_1,X_1)	Data(f_1,X_2)		Data(f_1,X_n)
Data(f_2,X_1)	Data(f_2,X_2)		Data(f_2,X_n)
Data(f_m,X_1)	Data(f_m,X_2)		Data(f_m,X_n)

An example of the format for Data(f_m,X_n) is shown below.

Table 4 Data format for a single frequency at a single position.

Re(S_{11})	**Im(S_{11})**	**Re(S_{21})**	**Im(S_{21})**	**Re(S_{22})**	**Im(S_{22})**

"Re()" and "Im()" indicate the real and imaginary parts, respectively.

Comment (Text) Files

The comment text files contain information about measurement conditions (i.e. position, direction, etc.) and any comments the user entered during the measurements. For example, the comment file a0348ag.txt is printed below:

```
Start Time: 511/Stop Time: 519/Target #: A2/Start f: 10/Stop f: 410/Num of
Points: 201/Antenna Orientation: 92/Num of Scans: 41/Antenna Position:
xstart: -60/delta x: 3/yoffset: 0/Relative Permitivity: 20/User Comments: /$
```

The file contains the time, in minutes after midnight, at which the scan was started and finished. It also contains the information necessary to recreate the frequency vector and the position vector, i.e. number of positions of data taken and the spacing between them.

REPORT DOCUMENTATION PAGE (SF298)
(Continuation Sheet)

GPR Performance in the Presence of Buried Biomass

Part 2: Simulation and Analysis

Final Report

for the period

15 September 2001 – 14 September 2002

Contract: DAAD19-01-1-0760
Project: E-43042-EL-000-01234-1

Prepared for

Dr. Russell Harmon
The US Army Research Office
P.O. Box 12211
Research Triangle Park, NC 27709-2211

Prepared by

Mr. N. Niltawach
Prof. J. T. Johnson
Dr. C.-C. Chen
Dr. B. A. Baertlein

The Ohio State University
ElectroScience Laboratory
1320 Kinnear Road
Columbus, OH 43212

4 October 2002

TABLE OF CONTENTS

LIST OF FIGURES V

1.0 INTRODUCTION 1

2.0 COMPUTING ROOT SCATTERING 3

2.1 Formulation of Volume Integral Equation 3

2.2 Computation of $\overline{\overline{A}}(\bar{r}_i, \bar{r}_j)$ 9

2.3 Solving Equation (2.15) 9

2.4 Representing Thick Cylinders with DDA 10

2.5 Validation with Other Codes 10

2.6 Limitations of DDA 13

2.7 Summary 16

3.0 SCATTERING FROM LONG ROOTS APPROXIMATED BY INFINITELY LONG CYLINDERS 17

3.1 Scattering from a Dielectric Circular Cylinder: TM_z Polarization 17

3.2 Scattering from a Dielectric Circular Cylinder: TE_z Polarization 22

3.3 Comparisons of Magnitude of Scattered Fields from TM_z and TE_z Cases 27

3.4 Summary 28

4.0 IMPLEMENTATION OF DDA TO MODEL THE GPR SYSTEM 29

4.1 Modeling of the GPR System 29

4.2 Verification of the Model 31

4.3 Finding the Antenna Response $H_B(\omega) H_F(\omega)$ 38

4.4 Comparison of Experiment and DDA Predictions for T(ω) 40

4.5 Summary 43

5.0 CASE STUDIES OF EFFECTS OF ROOTS ON GPR 44

5.1 Properties of Root Scattering **44**

5.2 Approximations to Reduce Model Complexity **46**

5.3 Comparison Between Modeled and Measured GPR Data **48**

5.4 Case Studies of the Effects of Roots on GPR Systems **50**

5.5 Target Detection in the Presence of Roots **50**

5.6 Target Signature Attenuation **55**

5.7 Imaging of Simulated GPR Data **58**

5.8 Summary **62**

6.0 CONCLUSIONS AND FUTURE WORK **63**

APPENDIX A : FREQUENCY RESPONSE OF AN INFINITELY LONG PERFECTLY CONDUCTING WIRE IN THE FREQUENCY RANGE FROM 0.05-1.5 GHZ **65**

APPENDIX B: DIELECTRIC CONSTANT OF TREE ROOTS **67**

APPENDIX C: DIELECTRIC CONSTANT OF SOILS **69**

REFERENCES **76**

List of Figures

Figure 1.1. "Site 1" area..... 2
Figure 2.1. Comparison between the original and discretized root structures. (a) Experimental image. (b) Model representation..... 4
Figure 2.2. A plane wave incident on a scatterer with permittivity ε, permeability μ_o and volume V. The scatterer resides in a region denoted V_m, which contains a medium with parameter (ε_m , μ_o)..... 5
Figure 2.3. (a) A thin cylinder with radius a and length L. (b) Segmentation of the cylinder into small cells of length l..... 8
Figure 2.4. Approximations for cylinders with different radii for a_{max} = 0.015 m. (a) a = 0.030 m. (b) a = 0.0396 m..... 10
Figure 2.5. Plane waves incident on a cylinder with angle θ..... 11
Figure 2.6. Comparisons of radar cross sections computed by DDA and BOR at frequency 1 GHz for a 0.3 m long, 0.015 m radius, cylinder with permittivity 2 (1 component cylinder, i.e., $a < a_{max}$). (a) VV. (b) HH..... 11
Figure 2.7. Same as Figure 2.6 but with radius = 0.030 m (4 component cylinder, see Figure 2.4(a)). (a) VV. (b) HH..... 12
Figure 2.8. Same as Figure 2.6 but with radius = 0.0396 m (7 component cylinder, see Figure 2.4(b)). (a) VV. (b) HH..... 12
Figure 2.9. Comparison of VV radar cross section computed by DDA and ESP. The geometry of the problem in shown in Figure 2.5 with θ = 90 degrees. The cylinder is 0.2 m in length and 0.0667 m in radius..... 13
Figure 2.10. Cylinder geometries used to test the effects of gaps. (a) Cylinder with a 1 cm gap. (b) Cylinder without a gap..... 14
Figure 2.11. Comparison of fields backscattered from a cylinder with and without a gap for relative permittivities of 2 and 4. The polarization of the incident field is vertical. (a) Frequency domain (RCS). (b) Time domain..... 15
Figure 2.12. Same as Figure 2.11 but for horizontal polarization. (a) Frequency domain (RCS). (b) Time domain..... 15
Figure 3.1. TM_z plane wave impinges on a dielectric circular cylinder..... 17
Figure 3.2. Comparisons between scattered field intensity computed by the exact solution and the small radius approximation at $\rho = \lambda$ and $\phi = 180°$. Vertical arrows indicate the point at which $\beta_d a$ = 0.1. TM_z case. (a) Magnitude. (b) Phase..... 20
Figure 3.3. Scattered field intensity at distance $\rho = \lambda$ as a function of effective radius for TM_z polarization..... 21
Figure 3.4. Scattered field intensity at distance $\rho = \lambda$ as a function of ε_c for TM_z polarization..... 22
Figure 3.5. TE_z plane wave impinges on a dielectric circular cylinder..... 22
Figure 3.6. Comparisons between scattered field intensity computed by the exact solution and the small radius approximation at $\rho = \lambda$ and $\phi = 180°$. Vertical arrows indicate the point at which $\beta_d a$ = 0.1. TE_z case. (a) Magnitude. (b) Phase..... 25
Figure 3.7. Scattered field intensity at distance $\rho = \lambda$ as a function of effective radius for TE_z polarization..... 26
Figure 3.8. Scattered field intensity at distance $\rho = \lambda$ as a function of ε_c for TE_z polarization..... 26
Figure 3.9. Relative magnitude of scattered fields for the TM_z and TE_z polarizations as a function of relative permittivity and radius..... 27
Figure 4.1. (a) GPR system from top view. (b) GPR system from side view. (c) Dielectric-loaded horn antenna..... 29
Figure 4.2. (a) Geometry of the GPR system over the soil. (b) GPR system when the air-ground interface is removed..... 30
Figure 4.3. The initial experimental set-up. (a) Top view. (b) Side view..... 32
Figure 4.4. Comparison of the time domain responses of a 1" diameter rod. (a) Measured data. (b) DDA calculated data..... 33

Figure 4.5. The set-up of the experiment. 34
Figure 4.6. The set-up of the experiment. (a) GPR collects data from a background. (b) GPR collects data from a background and a cylinder. 35
Figure 4.7. Frequency response of the background in the absence of a rod ($R_1(\omega)$). 36
Figure 4.8. Frequency response of the background and a rod ($R_2(\omega)$). 37
Figure 4.9. Difference between $R_2(\omega)$ and $R_1(\omega)$ ($R_{sub}(\omega)$). 37
Figure 4.10. Subtracted data in the time domain and a late-time window to remove early 38
Figure 4.11. Response from a long thin wire at the surface, which is proportional to the antenna response $H_B(\omega)H_F(\omega)$. 39
Figure 4.12. The frequency response of the rod $T(\omega)$, obtained by applying the window in the time domain and dividing by the antenna response. 40
Figure 4.13. Comparison of measured and DDA-calculated backscatterer for two rods with the same permittivity and different diameters. (a) Frequency response. (b) Time-domain response. 41
Figure 4.14. Comparison of measured and DDA-calculated backscatterer for two rods with the same diameter and different permittivities. (a) Frequency response. (b) Time domain response. 42
Figure 4.15. Dielectric rods used in the experiment. Note that "*d*" stands for diameter. 43
Figure 5.1. Configuration of the GPR scan used to study the scattering characteristics of a long, thin root with dielectric constant 20+10i. (a) Front view. (b) Side view. 44
Figure 5.2. Magnitude of the scattered field intensity (in dB) as a function of root diameter in wavelengths and dielectric constant. 45
Figure 5.3. Only roots in a circular cone shape are considered in the scattering compu-tation. 46
Figure 5.4. Comparison of scattered field intensities computed when considering all roots discretized using Equation (5.1) and only those roots that fall within the circular cone discretized using Equation (5.2). 47
Figure 5.5. GPR scan path and root structure 48
Figure 5.6. Comparison of measurements and model predictions. (a) Experimental data. (b) Model simulation. 49
Figure 5.7. Sixteen chosen root locations 51
Figure 5.8. Sixteen examples of clutter spectra computed over known root locations 52
Figure 5.9. (a) Detectability calculations for a 105 mm shell in roots. The indicated line is the decision threshold for a false alarm rate of 0.01/m2. (b) Orientation of 105 mm shell as a function of θ. 54
Figure 5.10. UXO-shaped target modeled with cylinders 55
Figure 5.11. Comparison of responses from a target when roots are and are not present. (a) Frequency domain. (b) Time domain. 56
Figure 5.12. Distortion of the incident field magnitude at the depth 0.3 m for 0.1 GHz. 57
Figure 5.13. Distortion of the incident field magnitude at the depth 0.3 m for 0.6 GHz. 57
Figure 5.14. Distortion of the incident field magnitude at the depth 0.3 m for 1.0 GHz. 58
Figure 5.15. (a) Time domain response of a UXO-shaped lossy dielectric target. (b) Image of Figure 5.15(a). 60
Figure 5.16. Image of the lossy dielectric target 61
Figure 5.17. Image of Figure 5.5(b) 61
Figure A1. TM_z plane wave impinges on a conductive circular cylinder 65
Figure B1. Real and imaginary parts of ε_v of a root with gravimetric moisture content = 0.58. 68
Figure C1. Moisture content of soil from Site 1 and Site 2 70
Figure C2. Characteristic parameters for soil with moisture content 0% at different depths. (a) Dielectric constant. (b) Conductivity. 71
Figure C3. Characteristic parameters for soil with moisture content 5% at different depths. (a) Dielectric constant. (b) Conductivity. 72
Figure C4. Characteristic parameters for soil with moisture content 10% at different depths. (a) Dielectric constant. (b) Conductivity. 73
Figure C5. Dielectric constant of the soil samples with moisture content 5% from different depths. 74
Figure C6. Conductivity of the soil samples with moisture content 5% from different depths. 75

1.0 Introduction

This document comprises Part 2 of the final report for the research effort entitled "GPR performance in the presence of buried biomass" (Contract DAAD19-01-1-0760, Project No.: E-43042-EL-000-01234-1). There is extensive anecdotal evidence that biomass (i.e., plant and tree roots) adversely affects ground-penetrating radar (GPR) performance. In this effort the Ohio State University (OSU) ElectroScience Laboratory (ESL) described the physics that govern the propagation and scattering of GPR waveforms in the presence of buried biomass. This work is being performed in collaboration with the US Army Research Laboratory.

This report is presented in two parts. In Part 1 we document the results of experimental GPR measurements performed at Site C62 at Eglin, AFB, FL. In Part 2 we describe numerical modeling work that permits us to simulate and interpret many of the results presented herein.

Ground penetrating radar (GPR) has been used extensively to detect and discriminate unexploded ordnance (UXO), because of its ability to penetrate soil. Recent data suggest that the performance of GPR may be impaired by buried biomass. Specifically, problems were observed during measurements by the U.S. Army Research Laboratory (ARL) at Eglin AFB using the BoomSAR—an ultra-wideband (UWB) synthetic aperture radar (SAR) mounted on a mobile lift platform. It is known that there is a high density of roots at that site, and those roots were thought to affect the penetration of electromagnetic energy into the soil.

A team from OSU/ESL visited Eglin AFB during December 10-12, 2001 to perform additional tests. A detailed discussion of the OSU measurements appears in a separate report [1]. GPR briefly, measurements were performed in areas roughly 2 m by 2 m in size. One of those areas had a high density of roots and is referred to as "Site 1." This area is shown in Figure 1.1 after the soil was removed. Most of the roots were found in the top 12 inches of soil. The measurements comprised scans over the roots with a ground-contacting GPR antenna.

The root structure shown in Figure 1.1 was removed and taken to OSU for further study. All of the roots simulations presented here are based on the root structure shown in that figure.

Figure 1.1. "Site 1" area

In this report we present a combination of experiments, theory and modeling that was used to gain additional insight into root scattering. The report is organized in five major chapters. In Chapter 2 we describe the discrete dipole approximation (DDA), an algorithm that can be used to compute fields scattered from tree roots. In Chapter 3 the exact solutions and small argument approximations for scattering from infinitely long cylinders are reviewed. The use of the DDA as a model for the GPR system is presented in Chapter 4. Case studies of the effects of roots on GPR are presented in Chapter 5. The report concludes with a discussion of the results in Chapter 6.

2.0 Computing Root Scattering

Scattering from buried objects has been studied extensively, because of its many applications including biomedical imaging, remote sensing, and geological exploration [2]. The targets of interest are both dielectric and conducting objects. Many papers relevant to this topic have been published in the last few decades, and only a few key works will be cited here. Homogeneous dielectric cylinders in a lossy half-space were considered by Mahmoud *et al*. [3]. Zhuck *et al*. [4] investigated inhomogeneous dielectric cylinders embedded in a stratified medium. Three-dimensional (3-D) objects buried in a dielectric half-space were studied by Lombardi *et al*. [2]. Butler *et al*. investigated conducting cylinders of arbitrary cross sections partially buried between two media [5],[6]. Perfectly conducting objects of arbitrary shape in multilayered media were explored by Michalski *et al*. [7]. 3-D dielectric and conducting objects buried under a one-dimensional (1-D) multilayered medium were studied by Cui *et al*. [8]. Since buried-target problems involve Sommerfeld-like integrals, which are time-consuming to evaluate, fast algorithms have been developed, e.g., Cui *et al*. [9],[10].

Although many studies of scattering from dielectric objects under a half-space have appeared, few of these specifically address tree roots. Sullivan [11] modeled tree roots as an ensemble of connected cylinders without including interaction between each root. El-Shenawee *et al*. [11] modeled a dielectric clutter object (which could be a tree root) close to an antipersonnel mine-like object under a rough surface.

In the present chapter we present a novel approach to the root scattering problem. A formulation of the underlying integral equation and its discretization based on the "Discrete Dipole Approximation (DDA)" [13] are described. Computational details are also discussed. A validation of the DDA code is presented, and its limitations are explained.

2.1 Formulation of Volume Integral Equation

As noted in Chapter 1, all of the analysis presented herein is based on the root structure shown in Figure 1.1. The root structure has been modeled by an ensemble of cylindrical segments. A comparison of the original and discretized versions is shown in

Figure 2.1. The cylinder diameters, which range from 0.3 – 4 cm, were obtained from measurements of the structure. A large root mass appears near the center of the figure. For reasons that will be discussed later, that mass was represented by a group of densely packed cylinders.

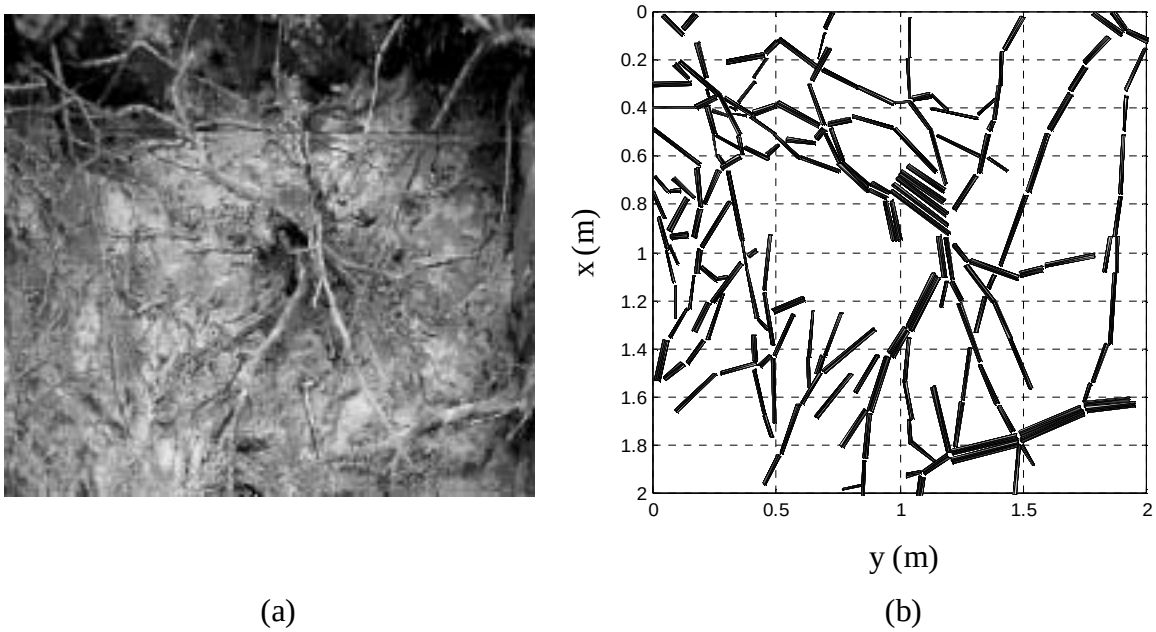

(a) (b)

Figure 2.1. Comparison between the original and discretized root structures. (a) Experimental image. (b) Model representation.

Each root segment is described by several variables, and from Figure 2.1(b) it is evident that we have to deal with a large number of unknowns. Also, we try to simulate GPR data, which require computation of fields at multiple frequencies and positions. This led us to investigate efficient algorithms. Note that herein, we will neglect the air-ground interface (explain in Chapter 4) so that the CPU and memory requirements can be reduced.

In the following a formulation of the electric-field volume integral equation is discussed using a discretization based on the DDA [13],[14]. The DDA is used because of its efficiency in computing fields scattered from complicated dielectric bodies. Furthermore, it includes interactions all parts of the bodies. In using the DDA we will approximate a continuum dielectric target by a finite array of dipoles. Hence, we expect

accurate results only if the array can describe the shape of the target satisfactorily. Tests are presented that quantify the algorithm's performance.

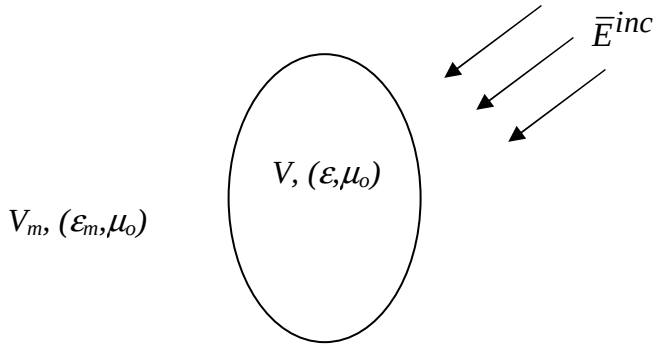

Figure 2.2. A plane wave incident on a scatterer with permittivity ε, permeability μ_o and volume V. The scatterer resides in a region denoted V_m, which contains a medium with parameter (ε_m , μ_o).

Consider a plane wave incident on a scatterer with permittivity ε (Figure 2.2). For the above geometry, Maxwell's equations can be written as

$$\nabla \times \bar{E} = +i\omega\mu_o \bar{H} \tag{2.1}$$

$$\nabla \times \bar{H} = -i\omega\varepsilon_p(\bar{r})\bar{E} \tag{2.2}$$

where

$$\varepsilon_p(\bar{r}) = \begin{cases} \varepsilon & if\ \bar{r} \in V \\ \varepsilon_m & if\ \bar{r} \in V_m \end{cases}. \tag{2.3}$$

The time dependence $e^{-i\omega t}$ is implied and suppressed through out the derivation.

Taking the curl of equation (2.1), using equation (2.2) and subtracting $k^2\bar{E}$ yields the vector Helmholtz equation

$$\nabla \times \nabla \times \bar{E} - k^2\bar{E} = k^2(\varepsilon_c - 1)\bar{E} \tag{2.4}$$

where $\varepsilon_c = \varepsilon / \varepsilon_m$ and $k^2 = \omega^2\mu_o\varepsilon_m$. Throughout this work, the term "relative permittivity" will refer to ε_c, which is computed for a background medium ε_m. The well-known solution of equation (2.4) can be expressed as

$$\bar{E}(\bar{r}) = \bar{E}^{inc} + \int_V d^3x \bar{\bar{G}}(\bar{r},\bar{r}') \cdot k^2(\varepsilon_c - 1)\bar{E}(\bar{r}') \tag{2.5}$$

where

$$\overline{\overline{G}}(\bar{r},\bar{r}') = \left(\bar{\bar{I}} + \frac{\nabla\nabla}{k^2}\right) g(\bar{r},\bar{r}') \tag{2.6}$$

and

$$g(\bar{r},\bar{r}') = \frac{e^{-ik|\bar{r}-\bar{r}'|}}{|\bar{r}-\bar{r}'|}. \tag{2.7}$$

The dyadic Green's function $\overline{\overline{G}}$ has a singularity given by [15],[16]

$$\overline{\overline{G}}(\bar{r},\bar{r}') = PV\,\overline{\overline{G}}(\bar{r},\bar{r}') - \frac{\overline{\overline{L}}\,\delta(\bar{r}-\bar{r}')}{k^2} \tag{2.8}$$

where *PV* is an abbreviation for the principal value, and $\delta(\bar{r}-\bar{r}')$ is the three-dimensional Dirac delta function. The integral of the first term in (2.8) is performed over the volume of the scatterer excluding an infinitesimal volume V_δ about the observation point $\bar{r}$. Although V_δ is infinitesimal, its shape must be specified, and that shape affects the dyad $\overline{\overline{L}}$. Substituting (2.8) into (2.5), the volume integral equation becomes

$$\overline{E}(\bar{r}) = \overline{E}^{inc}(\bar{r}) + \int_{V-V_\delta} d^3x\; \overline{\overline{G}}(\bar{r},\bar{r}')\cdot(\varepsilon_c - 1)\; k^2\; \overline{E}(\bar{r}') - (\varepsilon_c - 1)\overline{\overline{L}}\cdot\overline{E}(\bar{r}). \tag{2.9}$$

Equation (2.9) will now be discretized and evaluated numerically using the DDA algorithm.

The induced polarization density $\overline{P}$ can be expressed as a function of $\overline{E}$ as

$$\frac{\overline{P}(\bar{r})}{\varepsilon_m} = (\varepsilon_c - 1)\,\overline{E}(\bar{r}). \tag{2.10}$$

The volume *V* is discretized into volumes ΔV_j with centers at $\bar{r}_j$, $j = 1, 2, \ldots, N$ (*N* is the number of dipoles). The field $\overline{E}_j$ inside ΔV_j is further approximated as a constant ("pulse expansion") to obtain

$$\frac{\overline{P}(\bar{r})}{\varepsilon_m} = \frac{\overline{P}_j}{\varepsilon_m} = (\varepsilon_c - 1)\,\overline{E}(\bar{r}), \qquad \bar{r} \in \Delta V_j. \tag{2.11}$$

Then,

$$\bar{E}(\bar{r}_i) \approx \bar{E}^{inc}(\bar{r}_i) + \frac{k^2}{\varepsilon_m} \sum_{j=1,\, j\neq i}^{N} \bar{\bar{G}}(\bar{r}_i, \bar{r}_j) \cdot \bar{P}_j \Delta V_j + k^2 \int\limits_{V_i - V_\delta} d^3x \bar{\bar{G}}(\bar{r}_i, \bar{r}\,')(\varepsilon_c - 1)\bar{E}(\bar{r}_i)$$

$$-(\varepsilon_c - 1)\bar{\bar{L}} \cdot \bar{E}(\bar{r}_i) \qquad (2.12)$$

where we have approximated the *PV* integral away from $\bar{r}_i$ by its mean value, and we have taken $PV\int\limits_{V_i}(\,)\,d^3x \approx \int\limits_{V_i - V_\delta}(\,)\,d^3x$ for a finite V_δ. Let $\hat{R}$ be the unit vector from $\bar{r}_j$ to $\bar{r}_i$, let $R = \left|\bar{r}_i - \bar{r}_j\right|$ and let $\bar{\bar{I}}$ be the unit dyad. For $\bar{r}_i \neq \bar{r}_j$, $\bar{\bar{G}}(\bar{r}_i, \bar{r}_j)$ can be found from (2.6) by direct differentiation

$$\bar{\bar{G}}(\bar{r}_i, \bar{r}_j) = \left\{ (-1 + ikR + k^2R^2)\bar{\bar{I}} + (3 - 3ikR - k^2R^2)\,\hat{R}\hat{R} \right\} \frac{e^{ikR}}{4\pi k^2 R^3}. \qquad (2.13)$$

Define $\bar{\bar{A}}(\bar{r}_i, \bar{r}_j) = -\frac{k^2}{\varepsilon_m}\bar{\bar{G}}(\bar{r}_i, \bar{r}_j)$, $\bar{\bar{D}} = \int\limits_{V_i - V_\delta} d^3x \bar{\bar{G}}(\bar{r}_i, \bar{r}\,')$, and let the polarization $\bar{p}_j$ be given by $\bar{P}_j \Delta V_j$. Using the relation in (2.11), (2.12) becomes

$$\bar{\bar{\alpha}}^{-1} \cdot \bar{p}_i + \sum_{j=1,\, j\neq i}^{N} \bar{\bar{A}}(\bar{r}_i, \bar{r}_j) \cdot \bar{p}_j = \bar{E}^{inc}(\bar{r}_i) \qquad (2.14)$$

where $\bar{\bar{\alpha}}^{-1} = \frac{1}{\varepsilon_m(\varepsilon_c - 1)\Delta V_i}\left[\bar{\bar{I}} - k^2\left(\bar{\bar{D}} - \frac{\bar{\bar{L}}}{k^2}\right)(\varepsilon_c - 1)\right]$. If $\bar{\bar{A}}(\bar{r}_i, \bar{r}_i)$ is defined as $\bar{\bar{\alpha}}^{-1}$, (2.14) can be written as

$$\sum_{j=1}^{N} \bar{\bar{A}}(\bar{r}_i, \bar{r}_j) \cdot \bar{p}_j = \bar{E}^{inc}(\bar{r}_i). \qquad (2.15)$$

From (2.15) it is evident that the scattering problem reduces to finding the polarizations $\bar{p}_j$ that satisfy a system of 3N complex linear equations $[\bar{\bar{A}}] \cdot [\bar{p}] = [\bar{E}^{inc}]$. Once $\bar{p}_j$ is found, one can approximate the scattered fields by

$$\bar{E}_s(\bar{r}) \approx \sum_{j=1}^{N} \bar{\bar{A}}(\bar{r}, \bar{r}_j) \cdot \bar{p}_j. \qquad (2.16)$$

The polarization $\bar{p}_j$ in (2.15) can be found only if $\bar{\bar{D}}$ and $\bar{\bar{L}}$ are known. Note that both $\bar{\bar{D}}$ and $\bar{\bar{L}}$ depend on the shape of the exclusion volume. Since scattering from

cylinders is of interest here, it is natural to take the shape of the exclusion volume to be a circular cylinder.

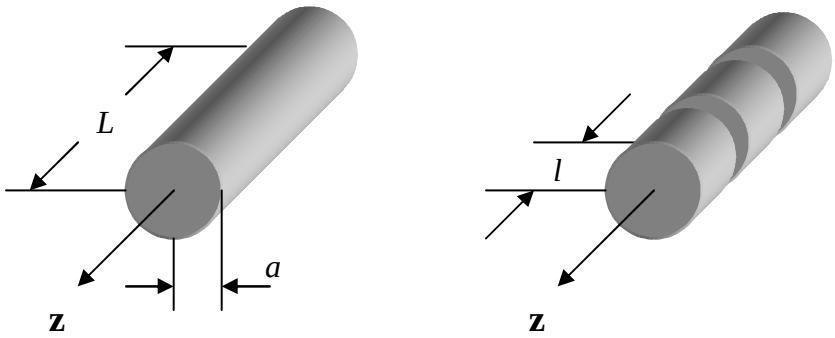

Figure 2.3. (a) A thin cylinder with radius *a* and length *L*. (b) Segmentation of the cylinder into small cells of length *l*.

Calculation of these dyads proceeds as follows: First, consider a thin cylinder with radius *a* and length $L >> a$ as shown in Figure 2.3(a). If the cylinder is also electrically thin with $(ka) << 1$, the current over each cross section is approximately uniform, and only the longitudinal variation in $\bar{p}$ is of interest. The cylinder may be segmented into small cells of length *l* as shown in Figure 2.3(b). We define an exclusion volume V_δ to be a cell with radius *a* and length *l*. It can be shown [14] that $\overline{\overline{D}}$ and $\overline{\overline{L}}$ for a circularly cylindrical cell with axis $\hat{z}$ are as follows.

$$\overline{\overline{L}} = L_x \hat{x}\hat{x} + L_y \hat{y}\hat{y} + L_z \hat{z}\hat{z} \tag{2.17}$$

$$\overline{\overline{D}} = D_x \hat{x}\hat{x} + D_y \hat{y}\hat{y} + D_z \hat{z}\hat{z} \tag{2.18}$$

$$L_x = L_y = \frac{l}{2\sqrt{4a^2 + l^2}} \tag{2.19}$$

$$L_z = 1 - \frac{l}{\sqrt{4a^2 + l^2}} \tag{2.20}$$

$$D_x = D_y = \frac{ika^2 l}{6} + \frac{l}{8}\left\{\sqrt{l^2 + 4a^2} - l\right\} + \frac{a^2}{4}\ln\left(\frac{l + \sqrt{l^2 + 4a^2}}{2a}\right) \tag{2.21}$$

$$D_z = \frac{ika^2 l}{6} + \frac{a^2}{2}\ln\left(\frac{l + \sqrt{l^2 + 4a^2}}{2a}\right) \tag{2.22}$$

2.2 Computation of $\overline{\overline{A}}(\bar{r}_i, \bar{r}_j)$

For $\bar{r}_i \neq \bar{r}_j$ the above formulation assumes that the matrix element are given by

$$\overline{\overline{A}}_{ij} = \frac{-k^2}{\varepsilon_m} \int_{\Delta v_j} d^3x' \overline{\overline{G}}(r_i, \bar{r}') \approx \frac{-k^2}{\varepsilon_m} \overline{\overline{G}}(\bar{r}_i, \bar{r}_j) \Delta V_j = \overline{\overline{A}}(\bar{r}_i, \bar{r}_j) . \tag{2.23}$$

This approximation is not accurate if $\bar{r}_i$ and $\bar{r}_j$ are within some small distance r_d [17]. One can improve the accuracy by applying numerical integration over the volume V_j centered at $\bar{r}_j$. An improved evaluation of the matrix terms are then given by

$$\overline{\overline{A}}_{ij} = \begin{cases} \dfrac{1}{\Delta V_j} \displaystyle\int_{v_j} d\bar{r}' \overline{\overline{A}}(\bar{r}_i, \bar{r}') & for \left| \bar{r}_i - \bar{r}_j \right| < r_d \\ \overline{\overline{A}}(\bar{r}_i, \bar{r}_j) & for \left| \bar{r}_i - \bar{r}_j \right| \geq r_d \end{cases} \tag{2.24}$$

For a thin cylinder, a suitable limit is $r_d = \lambda_m / 8$ where λ_m is the wavelength in the medium.

Figure 2.1(b) indicates that many cylinders are necessary to represent the root structure, which corresponds to a very large number of dipoles. For *N* dipoles, storage of the complex matrix $[\overline{\overline{A}}]$ requires $3N \times 3N \times 8$ bytes for four-byte floating point values. As an example, 2000 dipoles requires 288 MB of memory.

To reduce the memory usage, only those terms $\overline{\overline{A}}_{ij}$ that require numerical integration are stored. Terms that can be expressed in closed form are recalculated every time they are used.

2.3 Solving Equation (2.15)

The system of complex linear equations in equation (2.15) must be solved to find the polarization $\bar{p}_j$. An iterative solver is used here instead of a direct method, because iteration is more efficient when the number of dipoles is large. The Bi-Conjugate Gradient Stabilized (Bi-CGSTAB) method was chosen here, since it has been shown to converge more rapidly than other methods (for DDA) [18]. The iterative solver terminates when achieving $\left| [\overline{\overline{A}}] \cdot [\bar{p}] - [\overline{E}^{inc}] \right| \leq e \left| \overline{E}^{inc} \right|$, where e is an error criterion, chosen to be 10^{-3} in this work.

2.4 Representing Thick Cylinders with DDA

The thin-cylinder criterion used in DDA requires that the length and diameter of each cell must be small compared to the wavelength of the incident field. Thus, we require

$$\left|\sqrt{\varepsilon_c}\right| k(2a_{\max}) \le 1 \tag{2.25}$$

and

$$\left|\sqrt{\varepsilon_c}\right| k\, l_{\max} \le 1. \tag{2.26}$$

For a cylinder with radius $a > a_{max}$, a number of thin cylinders of the same length can be used to approximate the larger one such that the volume is still the same. Examples of how to arrange the component cylinders are shown in Figure 2.4.

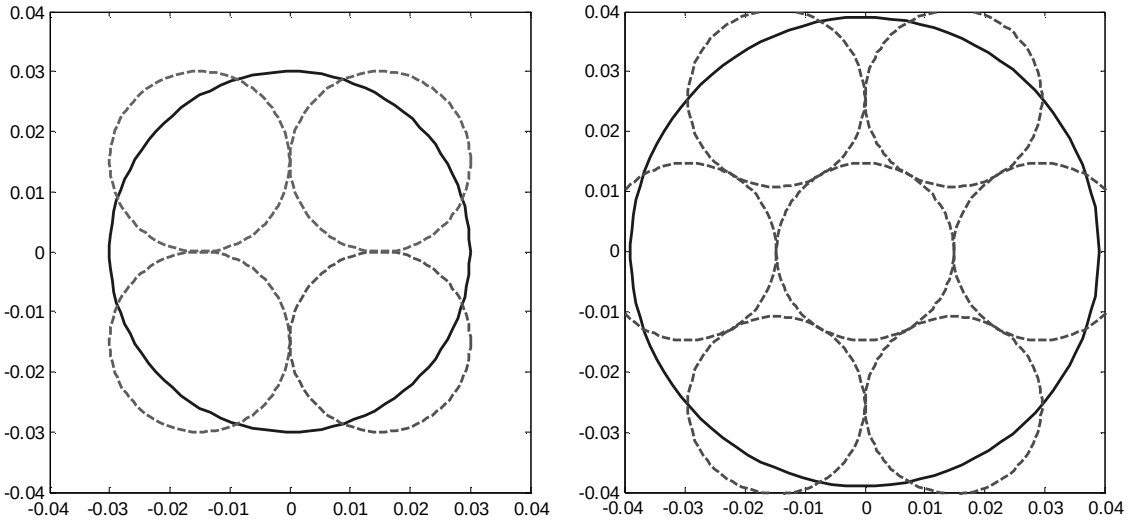

(a) (b)

Figure 2.4. Approximations for cylinders with different radii for a_{max} = 0.015 m. (a) a = 0.030 m. (b) a = 0.0396 m.

2.5 Validation with Other Codes

The DDA code has been compared with the Boeing "Body of Revolution (BOR)" code for cylinders with different radii. That code is based on research by Putnam *et al.* [19], Andreasen [20], and Mautz *et al.* [21]. The problem geometry, shown in Figure 2.5, comprises a plane wave impinging on a cylinder at different angles for vertical and

horizontal polarizations. Figures 2.6, 2.7 and 2.8 show good agreement of co-polarized (VV and HH) backscattered radar cross sections (RCS) for the DDA and BOR codes, even when thick cylinders are approximated by an ensemble of thinner cylinders.

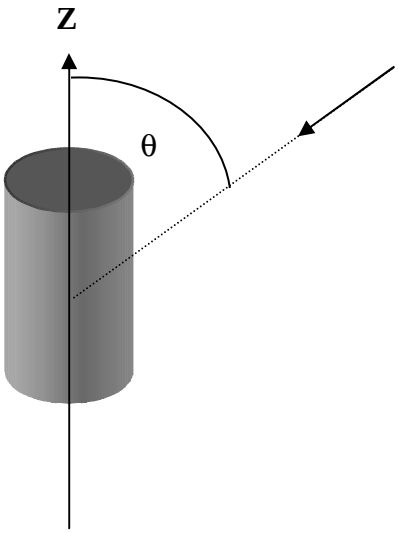

Figure 2.5. Plane waves incident on a cylinder with angle θ.

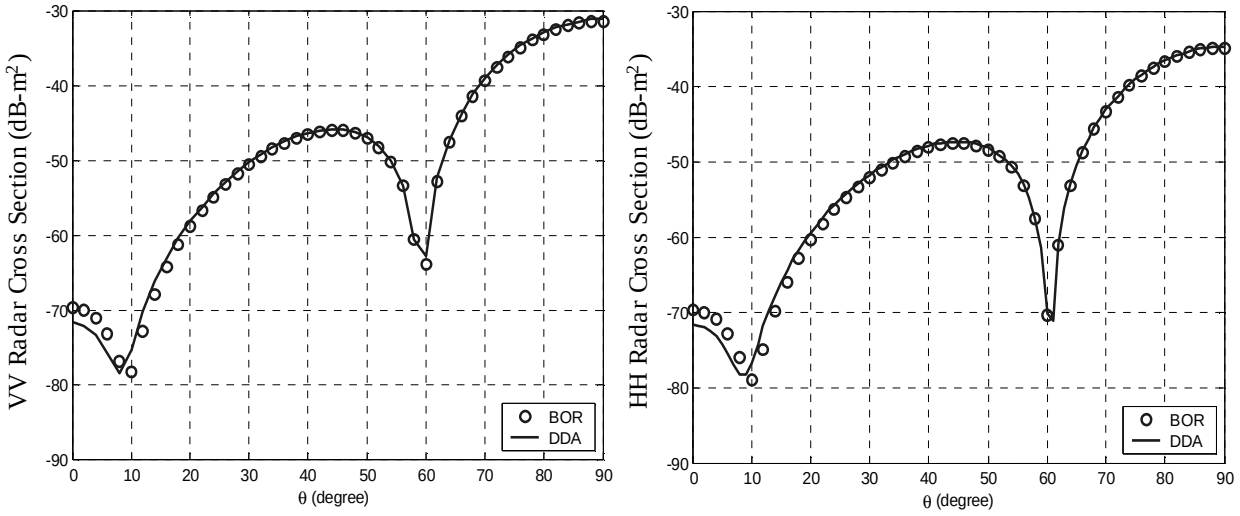

(a) (b)

Figure 2.6. Comparisons of radar cross sections computed by DDA and BOR at frequency 1 GHz for a 0.3 m long, 0.015 m radius, cylinder with permittivity 2 (1 component cylinder, i.e., $a < a_{max}$). (a) VV. (b) HH.

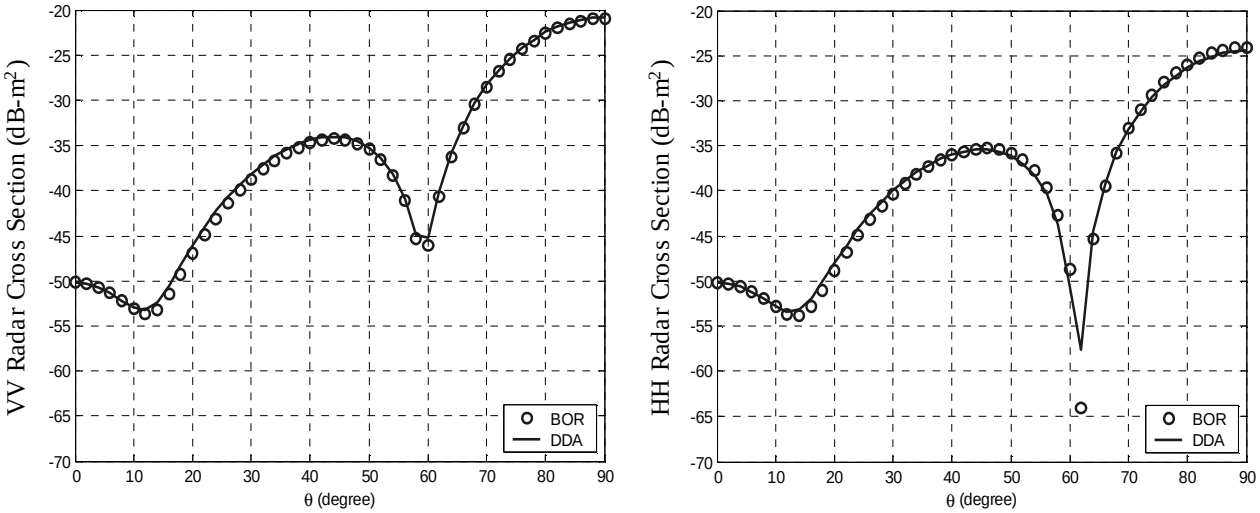

(a) (b)

Figure 2.7. Same as Figure 2.6 but with radius = 0.030 m (4 component cylinder, see Figure 2.4(a)). (a) VV. (b) HH.

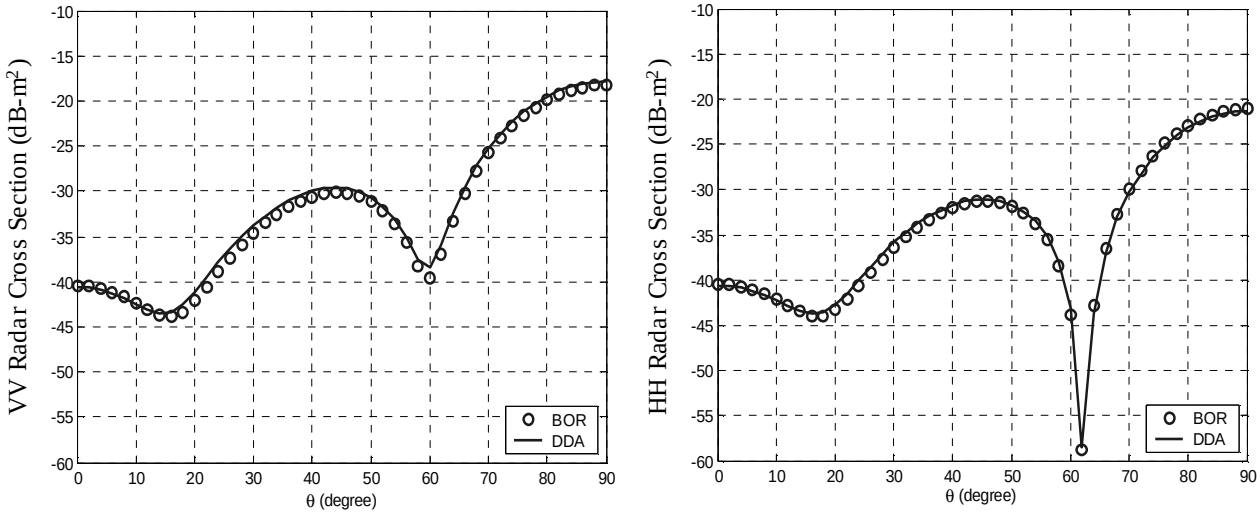

(a) (b)

Figure 2.8. Same as Figure 2.6 but with radius = 0.0396 m (7 component cylinder, see Figure 2.4(b)). (a) VV. (b) HH.

To quantify the efficiency of the DDA, we compared computational time with other codes. The geometry of the problem is exactly the same as Figure 2.5 with $\theta = 90$ degrees. The incident field is vertically polarized. The dimension of the cylinder is 0.2 m in length and 0.0667 m in radius with a dielectric constant of 2. We computed the

frequency response of this cylinder from 0.05 to 1.50 GHz. Since the BOR code mentioned before does not scan in frequency, the OSU's Electromagnetic Surface Patch (ESP) [22] code was used instead. Figure 2.9 shows good agreement of backscattered radar cross sections computed by the DDA and ESP codes. The time it takes for them to compute the above results is 17 minutes and 7.9 hours, respectively, on a Pentium 4 1.60 GHz computer with 256 MB memory. Note that this is probably not a fair comparison, because DDA uses an iterative method to solve the linear equations while ESP employs LU decomposition of the impedance matrix. Nonetheless, the large difference in time suggests that DDA is an obvious choice for handling large problems.

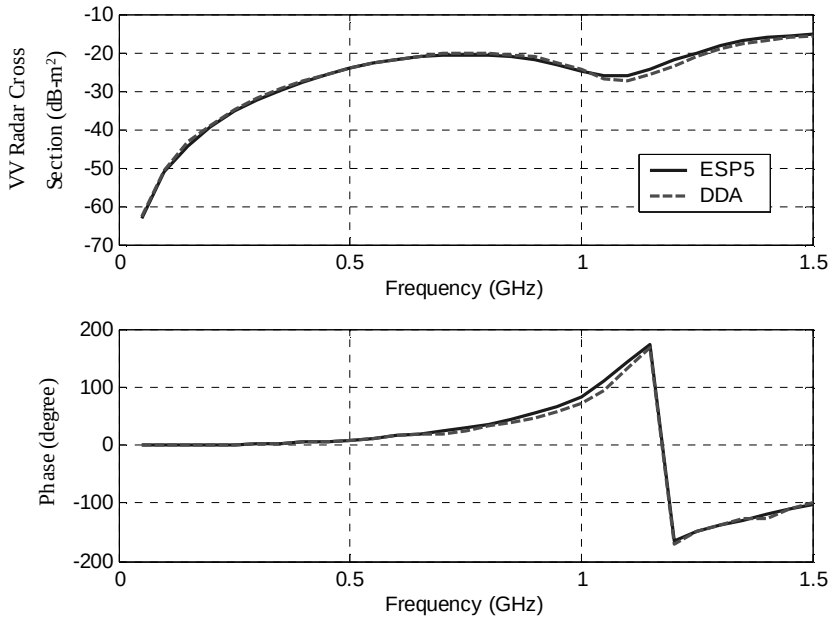

Figure 2.9. Comparison of VV radar cross section computed by DDA and ESP. The geometry of the problem in shown in Figure 2.5 with θ = 90 degrees. The cylinder is 0.2 m in length and 0.0667 m in radius.

2.6 Limitations of DDA

DDA has a few limitations, which are now described. First, in its current form DDA can only be used to compute fields scattered from a dielectric target with a dielectric constant that is not too large [13]. It has been found that the code is accurate when the relative permittivity magnitude is less than 5 to 6.

Second, there should be no intersections between the dielectric rods. Such intersections can result if dipoles from one cylinder are too close to dipoles from another cylinder. To prevent this, a small gap between adjacent cylinders is necessary, and Figure 2.1(b) shows how small gaps are included in the discretized root model. It is reasonable to question whether this gap produces significant errors in the calculation, we now show that these errors can be neglected.

The responses from a 2 cm-diameter cylinder with and without a 1 cm gap are calculated. The geometries of these two cases are shown in Figures 2.10(a) and 2.10(b), respectively. Note that the background is free space. Figures 2.11 and 2.12 compare the backscattered responses of the geometries in both the frequency and time domains for the broadside incident fields.

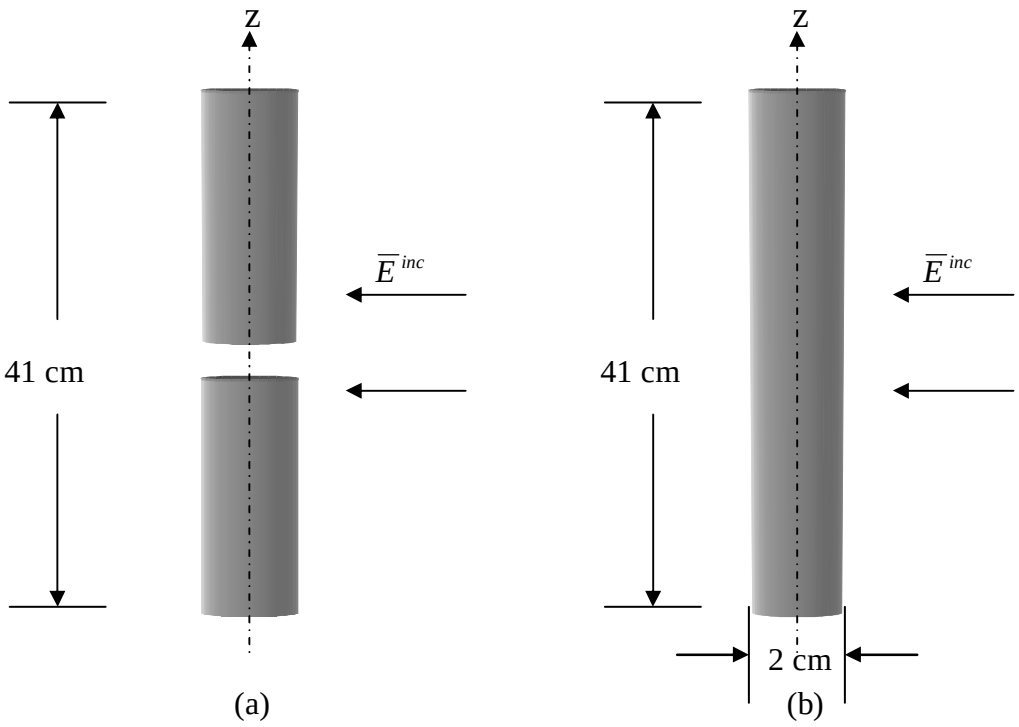

Figure 2.10. Cylinder geometries used to test the effects of gaps. (a) Cylinder with a 1 cm gap. (b) Cylinder without a gap.

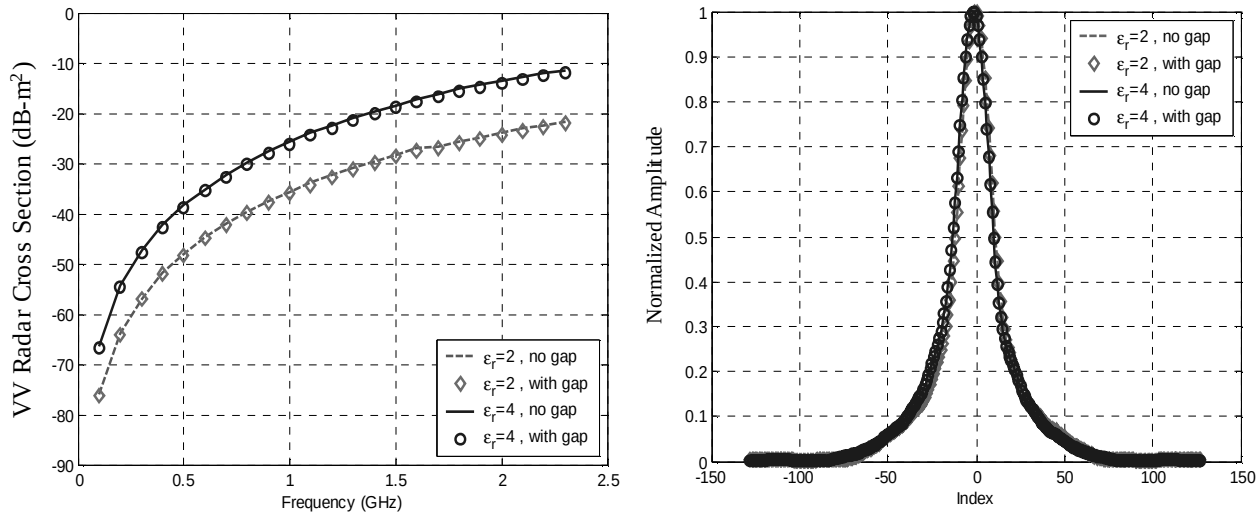

(a) (b)

Figure 2.11. Comparison of fields backscattered from a cylinder with and without a gap for relative permittivities of 2 and 4. The polarization of the incident field is vertical. (a) Frequency domain (RCS). (b) Time domain.

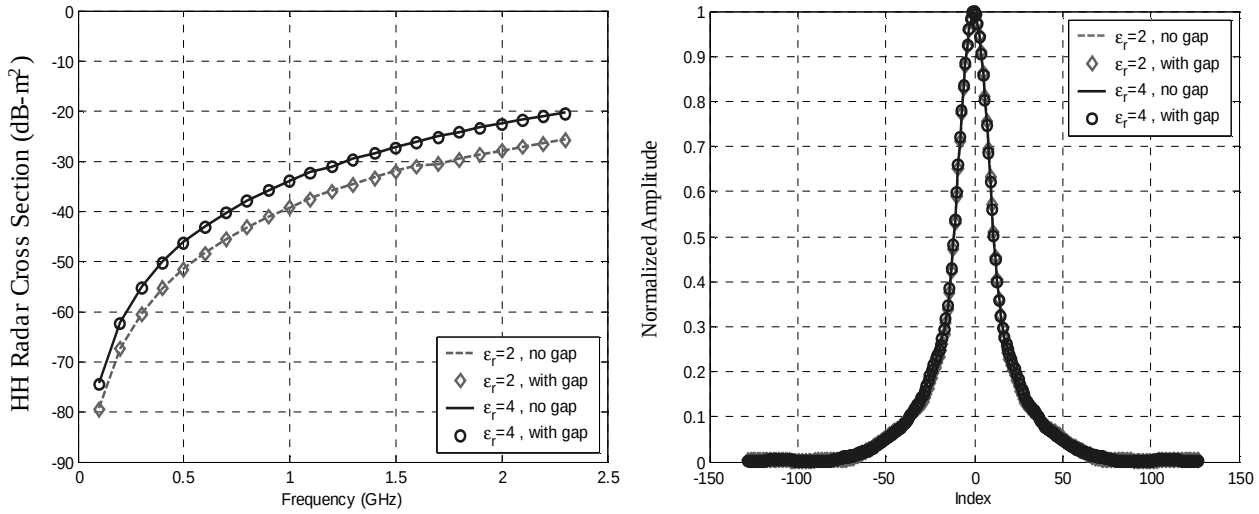

(a) (b)

Figure 2.12. Same as Figure 2.11 but for horizontal polarization. (a) Frequency domain (RCS). (b) Time domain.

The highest frequency considered here produces a wavelength that is comparable to that produced at 1 GHz in soil with a relative permittivity of 5. From Figures 2.11 and 2.12, it is clear that the effect of a gap can be neglected.

2.7 Summary

A root structure found at Eglin AFB, FL, was represented by an ensemble of dielectric cylinders for computational purposes. The formulation of the electric-field volume integral equation and its discretization based on the discrete dipole approximation (DDA) were described. The DDA code was validated against a body of revolution (BOR) code and OSU's Electromagnetic Surface Patch (ESP) code. It was shown that DDA can predict fields scattered from dielectric cylinders accurately. The efficiency of the DDA is illustrated by comparing the computational time with ESP. Limitations of DDA were discussed as well.

3.0 Scattering from Long Roots Approximated by Infinitely Long Cylinders

In the previous chapter it was shown that the DDA code can accurately compute scattering from finite, circular, dielectric cylinders. In this chapter we will study the exact solutions for scattering from a dielectric cylinder of infinite length and their approximations for a thin cylinder. The above approximations are interesting not only because tree roots usually resemble long, thin cylinders, but also because they show how the scattered field depends on the radius and relative permittivity of the cylinder. Here, the cylinders reside in a lossless homogeneous medium and normally incident plane waves with TM_z and TE_z polarizations are assumed. Comparisons of scattered fields for these two cases will be presented.

3.1 Scattering from a Dielectric Circular Cylinder: TM_z Polarization

Assume that a TM_z plane wave is normally incident on a dielectric circular cylinder with radius *a*, permittivity ε_d and permeability μ_0 as illustrated in Figure 3.1. The time dependence $e^{-i\omega t}$ is implied and suppressed throughout the derivation.

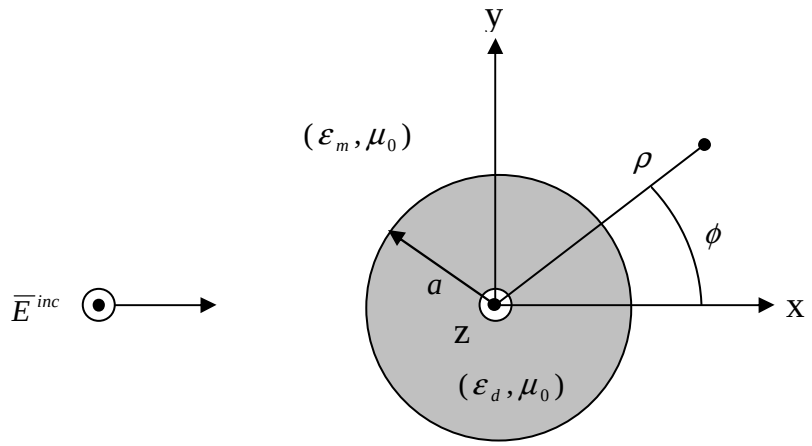

Figure 3.1. TM_z plane wave impinges on a dielectric circular cylinder.

It can be shown [23] that for this geometry, the expression for the scattered fields is

$$\overline{E}_s = \hat{z} E_0 \sum_{n=-\infty}^{\infty} c_n H_n^{(1)}(\beta_m \rho) e^{-in\phi} \tag{3.1}$$

where

$$c_n = (-i)^{-n} \frac{J_n'(\beta_m a) J_n(\beta_d a) - \sqrt{\varepsilon_c} J_n(\beta_m a) J_n'(\beta_d a)}{\sqrt{\varepsilon_c} J_n'(\beta_d a) H_n^{(1)}(\beta_m a) - J_n(\beta_d a) H_n^{(1)'}(\beta_m a)} \tag{3.2}$$

$J_n(.)$ = the Bessel function of the first kind of order n (n is an integer).

$J_n'(.)$ = derivative of $J_n(.)$ with respect to its argument.

$H_n^{(1)}(.)$ = the Hankel function of the first kind of order n.

$H_n^{(1)'}(.)$ = derivative of $H_n^{(1)}(.)$ with respect to its argument.

E_0 = magnitude of incident fields (set to 1).

$$\beta_m = \omega\sqrt{\mu_0 \varepsilon_m} \tag{3.3}$$

$$\beta_d = \omega\sqrt{\mu_0 \varepsilon_d} \tag{3.4}$$

$$\varepsilon_c = \varepsilon_d / \varepsilon_m \tag{3.5}$$

As noted previously, the term "relative permittivity" will refer to ε_c, which is computed for a background medium ε_m.

For a cylinder with an electrically small radius a, i.e., $\beta_d a << 1$, an approximation to c_n can be obtained by utilizing the small argument forms of the Bessel and Hankel functions as follows [24]:

$$J_n(x) \approx \begin{cases} (-1)^{|n|} \dfrac{1}{|n|!}\left(\dfrac{x}{2}\right)^{|n|} & \text{for } n < 0 \\ 1 & \text{for } n = 0 \\ \dfrac{1}{n!}\left(\dfrac{x}{2}\right)^{n} & \text{for } n > 0 \end{cases} \tag{3.6}$$

$$J_n'(x) \approx \begin{cases} (-1)^{|n|} \dfrac{1}{2(|n|-1)!}\left(\dfrac{x}{2}\right)^{|n|-1} & \text{for } n < 0 \\ -\dfrac{x}{2} & \text{for } n = 0 \\ \dfrac{1}{2(n-1)!}\left(\dfrac{x}{2}\right)^{n-1} & \text{for } n > 0 \end{cases} \tag{3.7}$$

$$H_n^{(1)}(x) \approx \begin{cases} (-1)^{|n|}\dfrac{1}{|n|!}\left(\dfrac{x}{2}\right)^{|n|} + i\left[\dfrac{-(|n|-1)!}{\pi}\left(\dfrac{2}{x}\right)^{|n|}(-1)^{|n|}\right] & \text{for } n < 0 \\ 1+\dfrac{2i}{\pi}\ln\left(\dfrac{1.781x}{2}\right) & \text{for } n = 0 \\ \dfrac{1}{n!}\left(\dfrac{x}{2}\right)^{n} + i\left[\dfrac{-(n-1)!}{\pi}\left(\dfrac{2}{x}\right)^{n}\right] & \text{for } n > 0 \end{cases} \quad (3.8)$$

$$H_n^{(1)\prime}(x) \approx \begin{cases} (-1)^{|n|}\dfrac{1}{2(|n|-1)!}\left(\dfrac{x}{2}\right)^{|n|-1} + i\,(-1)^{|n|}\dfrac{|n|!}{2\pi}\left(\dfrac{2}{x}\right)^{|n|+1} & \text{for } n < 0 \\ -\dfrac{x}{2}+\dfrac{2i}{\pi x} & \text{for } n = 0 \\ \dfrac{1}{2(n-1)!}\left(\dfrac{x}{2}\right)^{n-1} + i\left[\dfrac{n!}{2\pi}\left(\dfrac{2}{x}\right)^{n+1}\right] & \text{for } n > 0 \end{cases} \quad (3.9)$$

If ($\beta_m a$) is also small, i.e. $\beta_m a << 1$, then the term with index $n = 0$ dominates the series in (3.1). Substituting (3.6)-(3.9) into (3.2), c_0 can be approximated by

$$c_0 \approx \frac{-\pi(\beta_m a\sqrt{(\varepsilon_c - 1)})^2}{4i} \quad (3.10)$$

and $\overline{E}_s$ becomes

$$\overline{E}_s \approx \frac{-\pi H_0^{(1)}(\beta_m \rho)\,(\beta_m a\sqrt{(\varepsilon_c - 1)})^2}{4i}. \quad (3.11)$$

Figure 3.2 compares scattered field intensities computed via (3.1) and (3.11) for cylinders with different radii and relative permittivities (ε_c). As expected, the approximate solution works well when $\beta_d a << 1$ and $\beta_m a << 1$. In Figure 3.2, we show the results for relative permittivity $\varepsilon_c \le 7.5$. It is found that the approximate solution agrees with the exact solution for $\beta_m a \le 0.15$.

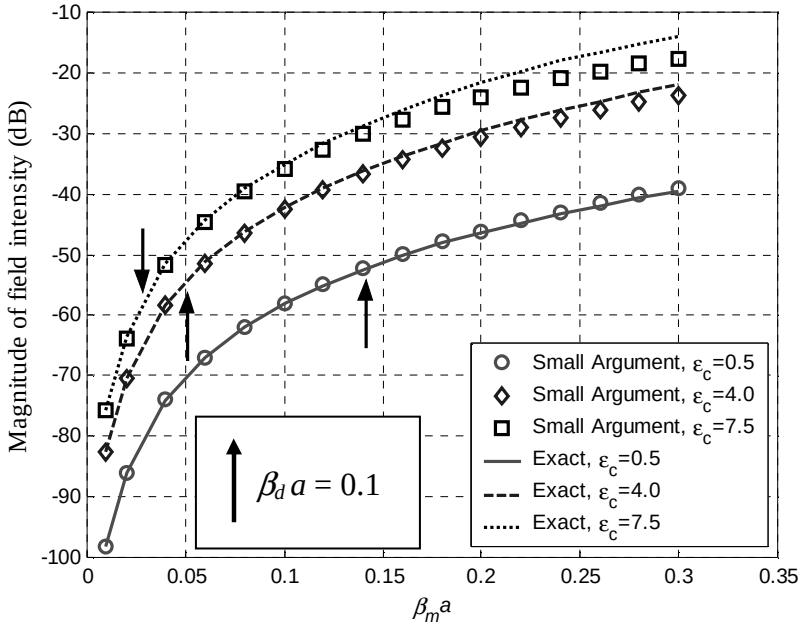

(a)

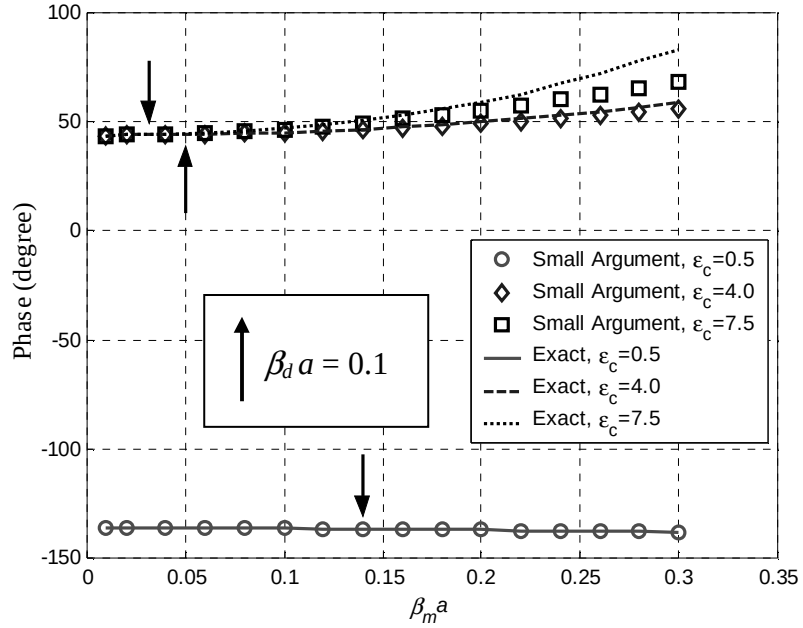

(b)

Figure 3.2. Comparisons between scattered field intensity computed by the exact solution and the small radius approximation at $\rho = \lambda$ and $\phi = 180°$. Vertical arrows indicate the point at which $\beta_d a = 0.1$. TM_z case. (a) Magnitude. (b) Phase.

From (3.11), we can write

$$\left|\overline{E}_s\right| = \pi\beta_m^2 \left| H_0^{(1)}(\beta_m \rho)\right| \left[a\sqrt{\left|\varepsilon_c - 1\right|}\right]^2 . \tag{3.12}$$

We find that the result is proportional to the cross-sectional area of the cylinder (expressed in square wavelengths) and to the dielectric contrast. If we define an effective radius $a_{e,TM} = a\sqrt{\left|\varepsilon_c - 1\right|}$ and let β_x = max(β_m , β_d), then all the results in Figure 3.2 can be summarized by a single universal curve shown in Figure 3.3. If the medium permittivity, operating frequency, radius and cylinder permittivity are known, the scattered fields can be found from Figure 3.3 directly. Note that the universal curve is valid when $\beta_x a << 1$.

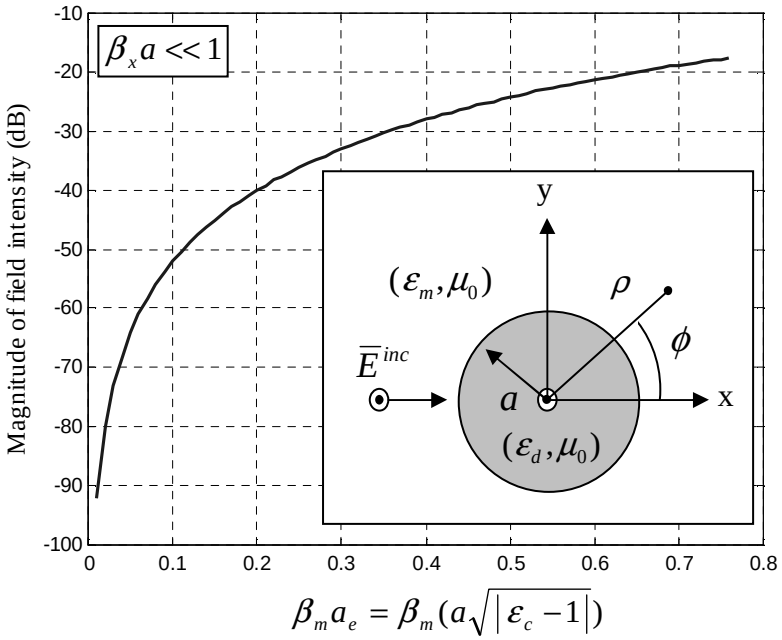

Figure 3.3. Scattered field intensity at distance $\rho = \lambda$ as a function of effective radius for TM_z polarization.

Furthermore, the scattered field intensity can also be plotted as a function of ε_c as shown in Figure 3.4. This figure shows that if the cylinder's relative permittivity approaches unity, the scattered fields will vanish, as expected.

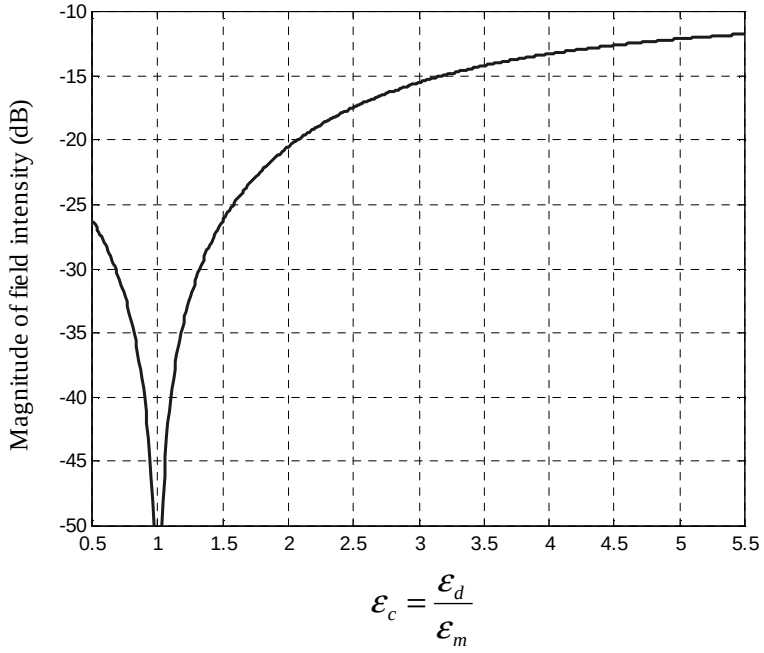

Figure 3.4. Scattered field intensity at distance $\rho = \lambda$ as a function of ε_c for TM_z polarization.

3.2 Scattering from a Dielectric Circular Cylinder: TE_z Polarization

The foregoing analysis is now repeated for a TE_z plane wave normally incident on a dielectric cylinder with radius a, permittivity ε_d and permeability μ_0 (see Figure 3.5).

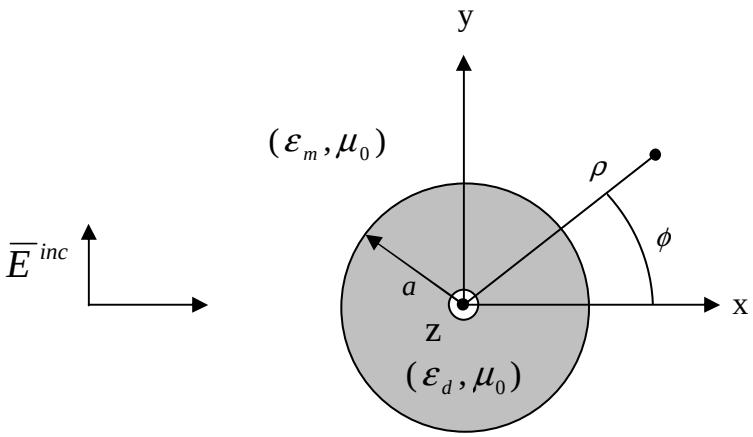

Figure 3.5. TE_z plane wave impinges on a dielectric circular cylinder.

For this geometry the scattered fields is [23]

$$\overline{E}_s = \hat{\rho} E_\rho + \hat{\phi} E_\phi \tag{3.13}$$

where

$$E_\rho = \frac{E_0}{(-i)\omega\varepsilon_m \rho \eta_m} \sum_{n=-\infty}^{\infty} n(-i)\ f_n H_n^{(1)}(\beta_m \rho) e^{-in\phi} \tag{3.14}$$

$$E_\phi = \frac{-\beta_m E_0}{(-i)\omega\varepsilon_m \eta_m} \sum_{n=-\infty}^{\infty} f_n H_n^{(1)'}(\beta_m \rho) e^{-in\phi} \tag{3.15}$$

$$f_n = (-i)^{-n} \frac{\sqrt{\varepsilon_c} J_n'(\beta_m a) J_n(\beta_d a) - J_n(\beta_m a) J_n'(\beta_d a)}{J_n'(\beta_d a) H_n^{(1)}(\beta_m a) - \sqrt{\varepsilon_c}\, J_n(\beta_d a) H_n^{(1)'}(\beta_m a)} \tag{3.16}$$

E_0 = magnitude of incident fields (set to 1).

$\eta_m = \sqrt{\dfrac{\mu_0}{\varepsilon_m}}$

For the electrically small cylinder case (i.e., $\beta_d a << 1$ and $\beta_m a << 1$), the small argument approximations of the Bessel and Hankel functions given in (3.6)-(3.9) permits us to simply the coefficients f_n as

$$f_n = \begin{cases} 0 & \text{for } n = 0 \\ (-i)^{-n} \left[\dfrac{(\varepsilon_c - 1)}{\dfrac{(-i)|n|!\,(|n|-1)!}{\pi}\left(\dfrac{2}{\beta_m a}\right)^{2|n|}(\varepsilon_c + 1)} \right] & \text{for } n \neq 0 \end{cases} \tag{3.17}$$

Thus, for a small radius cylinder, $E_\rho << E_\phi$, and the first two terms (n= +1 and -1) dominate the series of (3.14), so $\overline{E}_s$ becomes

$$\overline{E}_s = \hat{a}_\phi \left(\frac{(-i)\pi}{2}\right) H_1^{(1)'}(\beta_m \rho) \left(\beta_m a \sqrt{\frac{\varepsilon_c - 1}{\varepsilon_c + 1}}\right)^2. \tag{3.18}$$

Figure 3.6 compares scattered field intensities computed via (3.13) and (3.18) for cylinders with different radii and ε_c. As expected, the approximate solution works well when $\beta_d\ a$ <<1 and $\beta_m\ a$ <<1. Figure 3.6 shows that for TE case with relative permittivities $\varepsilon_c \le 7.5$, the approximate solution agrees with the exact for $\beta_m\ a \le 0.3$. From (3.18) one can write

$$\left|\overline{E}_s\right| = \frac{\pi\beta_m^2}{2}\left|H_1^{(1)'}(\beta_m\rho)\right|\left[a\sqrt{\left|\frac{\varepsilon_c - 1}{\varepsilon_c + 1}\right|}\right]^2. \qquad (3.19)$$

Once again, we can express these results using a single universal curve (Figure 3.7) if the effective radius is defined as $a_{e,TE} = a\sqrt{\left|\varepsilon_c - 1\right|/\left|\varepsilon_c + 1\right|}$ and we let β_x = max(β_m , β_d). Note that the universal curve is valid when $\beta_x a$ << 1.

Finally, the scattered field intensity can also be plotted as a function of ε_c as shown in Figure 3.8. As expected, if the relative permittivity of the cylinder approaches unity, the scattered fields vanish.

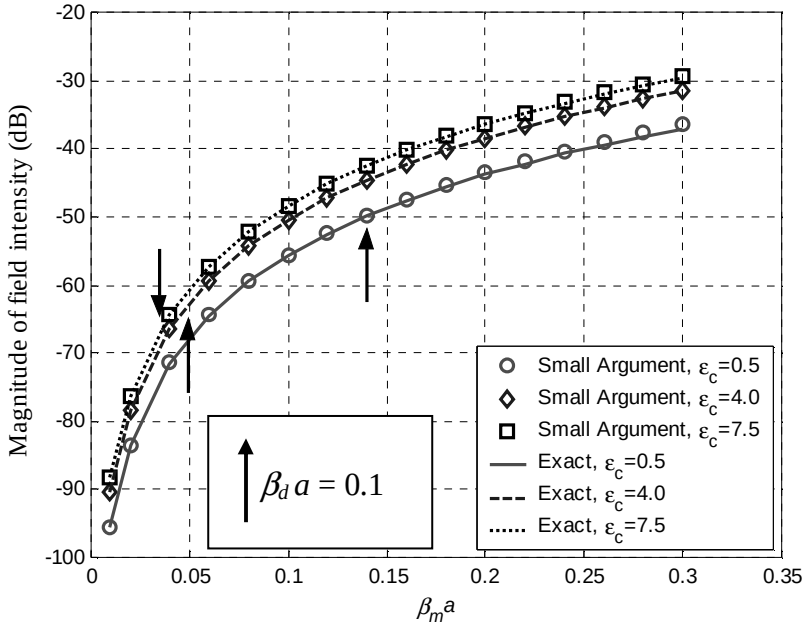

(a)

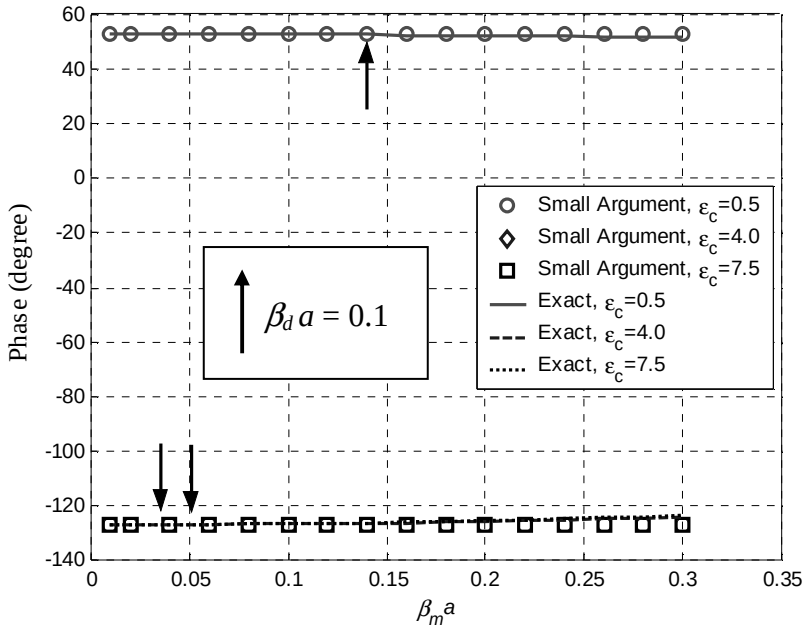

(b)

Figure 3.6. Comparisons between scattered field intensity computed by the exact solution and the small radius approximation at $\rho = \lambda$ and $\phi = 180°$. Vertical arrows indicate the point at which $\beta_d a = 0.1$. TE_z case. (a) Magnitude. (b) Phase.

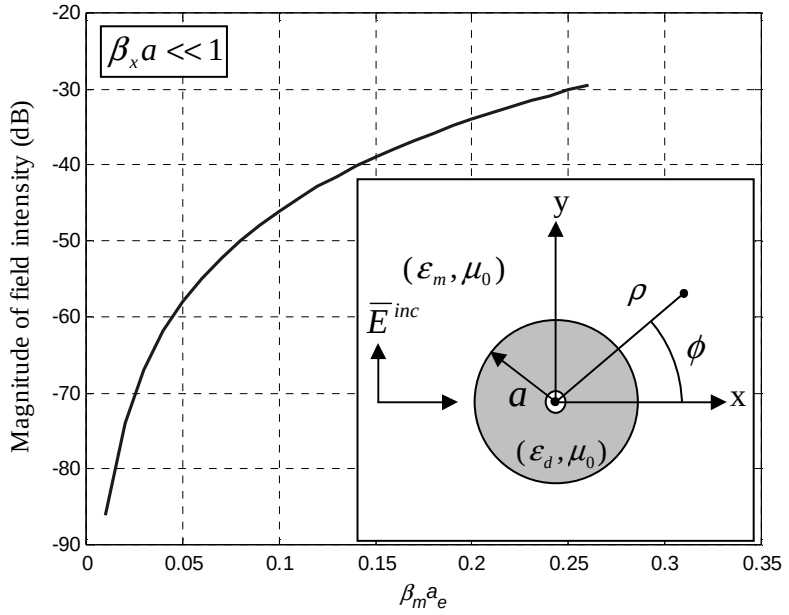

Figure 3.7. Scattered field intensity at distance $\rho = \lambda$ as a function of effective radius for TE_z polarization.

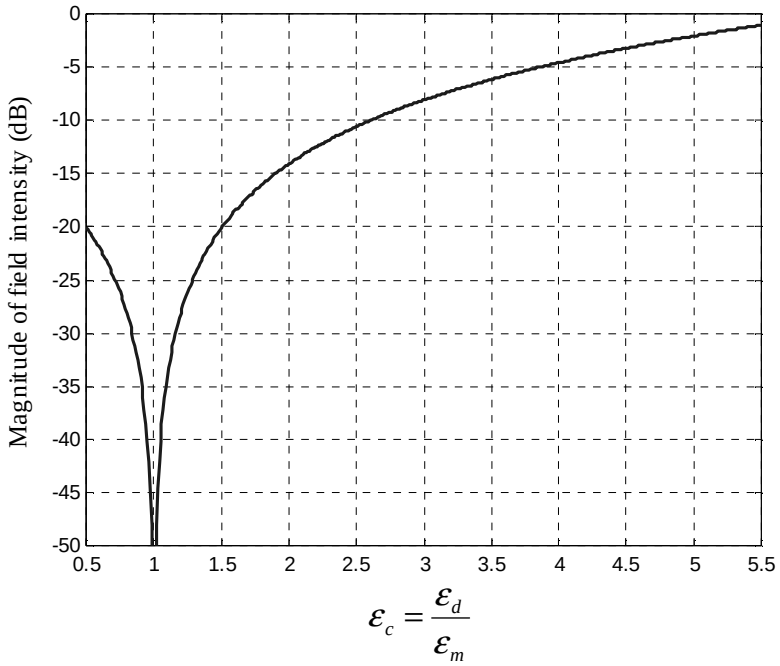

Figure 3.8. Scattered field intensity at distance $\rho = \lambda$ as a function of ε_c for TE_z polarization.

3.3 Comparisons of Magnitude of Scattered Fields from TM_z and TE_z Cases

We now use the foregoing approximations to predict GPR backscatterer from a long, thin linear root. The GPR is assumed to be far enough from the root to approximate a locally planar incident field. The root radius is assumed to satisfy the small radius approximation, $\beta_d a$ <<1, and is modeled by an infinitely long cylinder. Under these conditions, (3.11) and (3.17) may be used.

Figure 3.9 shows the relative magnitude of the scattered fields for parallel and perpendicular polarizations as a function of relative permittivity with respect to the medium (ε_c). It can be seen from these figures that as ε_c increases, fields backscattered by the perpendicular polarization can be neglected, which means that only roots in the same direction as the incident field need to be considered. When ε_c is relatively low, scattering from roots is less sensitive to both the incident polarization and the root radius. The intensity of the backscattered field, however, is relatively, small in that case.

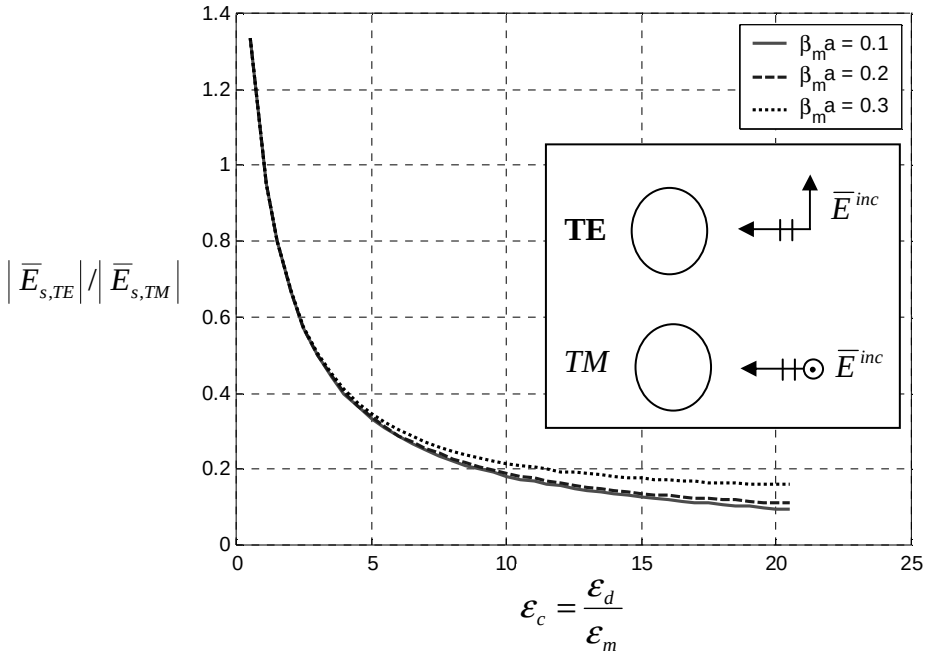

Figure 3.9. Relative magnitude of scattered fields for the TM_z and TE_z polarizations as a function of relative permittivity and radius.

3.4 Summary

This chapter has reviewed the exact solutions for scattering from an infinitely long dielectric circular cylinder. The small-radius approximations for plane-wave scattering from a cylinder for both TM_z and TE_z polarizations were described. The approximate solutions show how the scattered fields depend on the cylinder's radius and permittivity. It is also shown that for a root with a low relative permittivity the backscattered field is less dependent on the root orientation, although backscattering is much weaker in that case.

4.0 Implementation of DDA to Model the GPR System

In Chapter 2 it was shown that the DDA code can accurately calculate scattering from cylinders. In this chapter we use the DDA to simulate GPR data. Experiments and data-processing procedures for model validation are described. Comparisons of measured and calculated data are also presented.

4.1 Modeling of the GPR System

The GPR system used in the experiments was described previously in Part 1 of this report [1], and is illustrated in Figure 4.1(a) and 4.1(b). The radar functions are performed by a network analyzer controlled by a laptop computer. The system components are mounted on a low, wheeled, plastic cart. The antenna is a broadband, dual-polarization, dielectric-loaded horn antenna developed at OSU/ESL [25], and is further described below. The antenna and its dipole elements are shown in Figure 4.1(c).

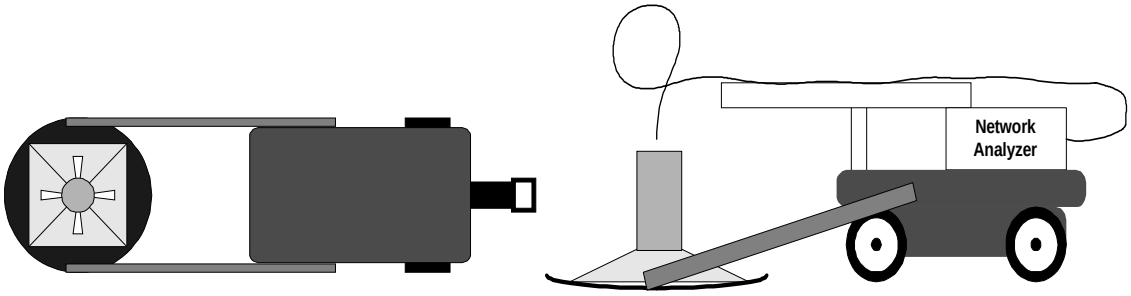

(a) (b)

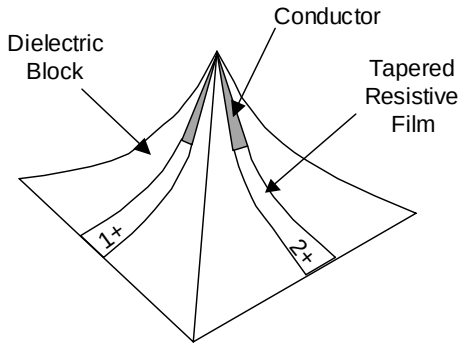

(c)

Figure 4.1. (a) GPR system from top view. (b) GPR system from side view. (c) Dielectric-loaded horn antenna

Reflections from the air-ground interface are typically strong and can overwhelm near-surface target returns. To reduce these surface reflections, the horn section of the antenna is filled with an artificial dielectric having a dielectric constant of five. If the soil permittivity is also near five, the antenna is matched to the ground, and the reflection coefficient is minimized. This fact simplifies modeling of the GPR, since the air-ground interface can be removed as shown in Figure 4.2.

A simple model for the GPR antenna is used here. The antenna is represented by two perpendicular dipole elements oriented in the x and y directions (assuming that the interface lies in the x-y plane). Note that the pattern of the real antenna may be different from a dipole, but it will be shown later that this simplification still works quite well. A complete model of this antenna on an air-ground interface using three-dimensional finite-difference time domain (3-D FDTD) has been presented by Kwan *et al*. [26].

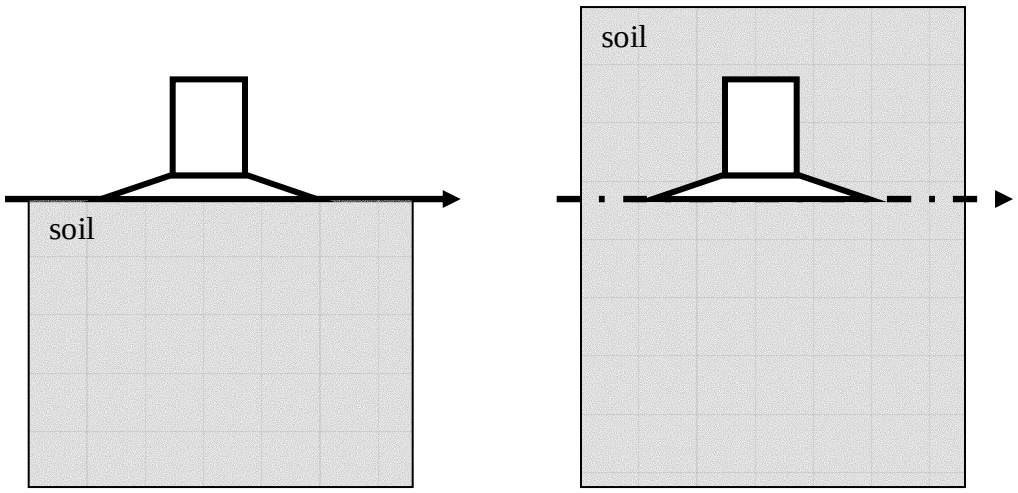

Figure 4.2. (a) Geometry of the GPR system over the soil. (b) GPR system when the air-ground interface is removed.

4.2 Verification of the Model

Experiments were performed to verify the above model. We first examined the response as a function of frequency and distance from a dielectric rod of length five feet and diameter one inch with a dielectric constant of 30. (The "rod" is actually a hose filled with the liquid, methanol.) The rod was buried at a depth of one foot in a pit filled with sand located at ESL. The GPR was scanned over the rod along a path perpendicular to the rod axis. The antenna was oriented such that the two dipole elements were parallel and perpendicular to the direction of the scan. Those elements are referred to as Channel 1 and Channel 2, respectively. The data were collected for frequencies from 0.05 to 1.5 GHz at 4.875 MHz increments. Position-scan data were acquired at 3 inch increments over a total range of 72 inches as shown in Figure 4.3. A comparison of measured and modeled time-domain responses for Channel 2 (parallel to the rod) is shown in Figure 4.4.

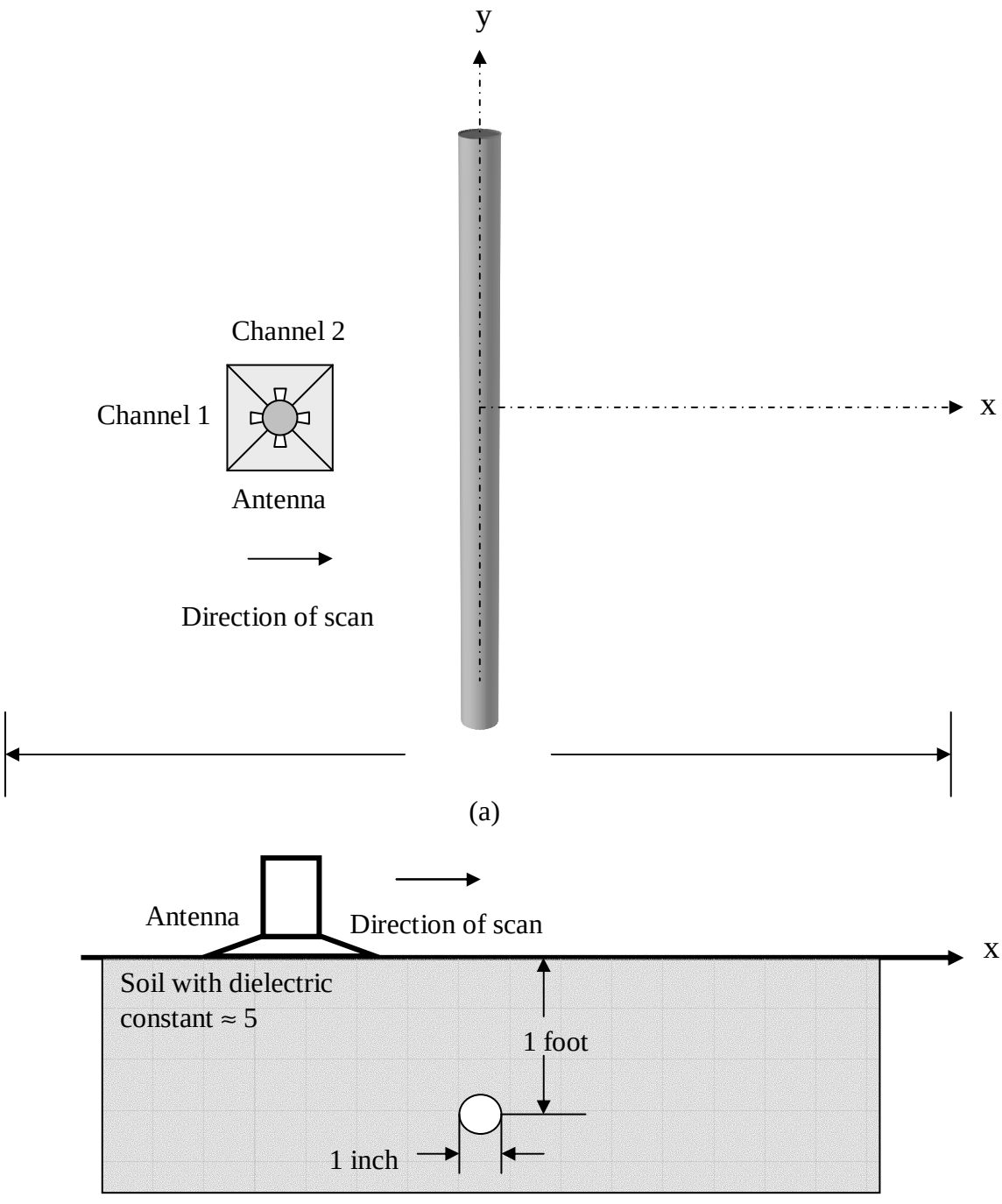

Figure 4.3. The initial experimental set-up. (a) Top view. (b) Side view

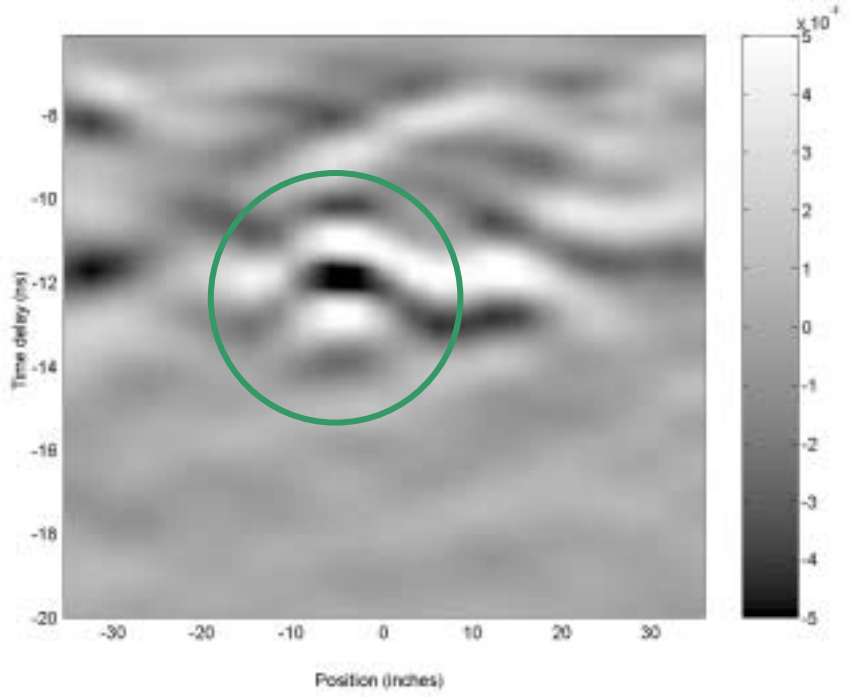

(a)

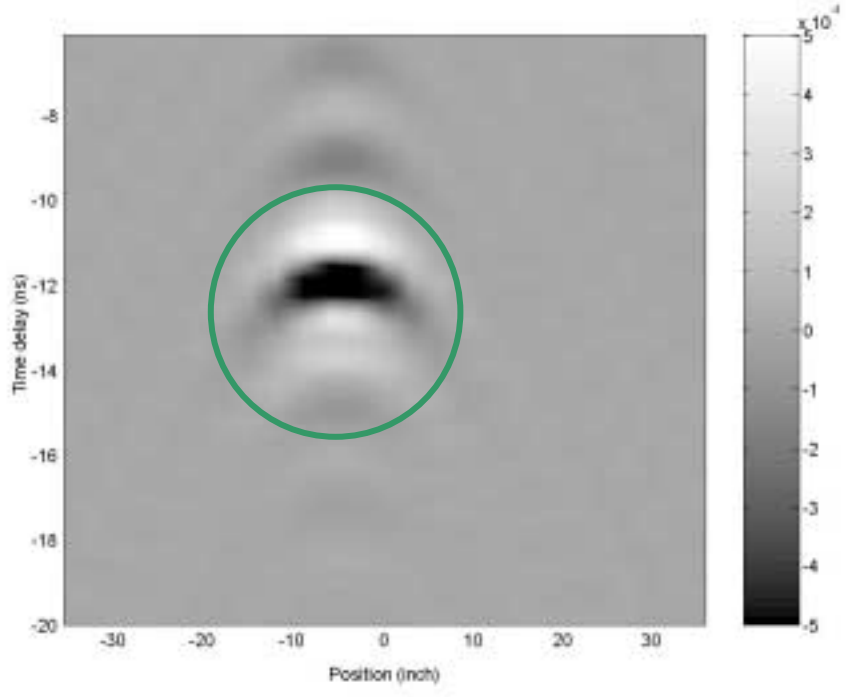

(b)

Figure 4.4. Comparison of the time domain responses of a 1” diameter rod. (a) Measured data. (b) DDA calculated data.

The measured and calculated responses have similar temporal and spatial characteristics (cf. Figures 4.4(a) and 4.4(b), respectively), but the former one has a lower signal-to-clutter ratio. This clutter is a result of soil inhomogeneities produced by digging and burial activities.

In order to obtain responses with reduced clutter, a second approach was used in subsequent measurements. The new experiment setup, shown in Figures 4.5 and 4.6, permits us to remove the majority of the clutter via background subtraction. A hole was made in a side of the test pit wall such that a rod could be inserted from the side without disturbing other parts of the soil. After acquiring the response of the background soil in the absence of the rod (see Figure 4.6(a)), rods with different dielectric constants and diameters were inserted into the hole for measurement one at a time. The data were collected from the polarimetric GPR antenna located directly above the rod. Figure 4.6(b) shows a diagram of the experiment after a rod was inserted.

Figure 4.5. The set-up of the experiment.

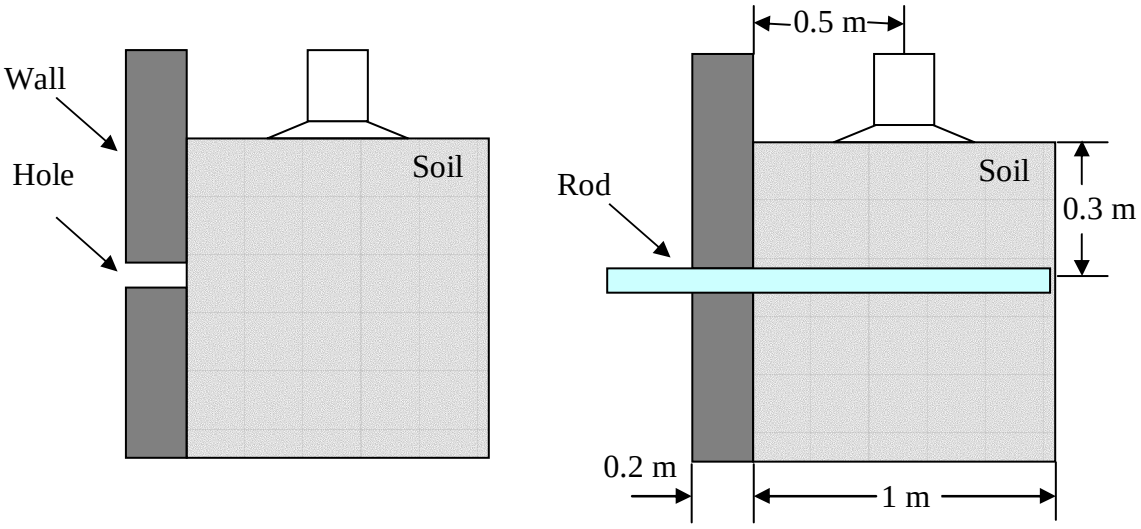

Figure 4.6. The set-up of the experiment. (a) GPR collects data from a background. (b) GPR collects data from a background and a cylinder.

The background subtraction process is straightforward. Define the frequency responses and transfer functions as follows:

$H_F(\omega)$ = Transfer function of the antenna when it radiates.

$B(\omega)$ = Frequency response of the background soil (including the interface) collected before the rod is inserted.

$H_B(\omega)$ = Transfer function of the antenna when it receives. (For a reciprocal antenna, $H_B(\omega) = H_F(\omega)$.)

$T(\omega)$ = Frequency response of fields backscattered from the rod.

ω = Angular frequency.

In the experiment the frequency-domain data were "S" parameters whose definition is [*V Output*] / [*V Input*] [27]. With the above definition, we can express the measured responses of the background ($R_1(\omega)$) and background with a rod ($R_2(\omega)$).

$$R_1(\omega) = \frac{[Output1]}{[Input]} = H_B(\omega) H_F(\omega) B(\omega) \tag{4.5}$$

$$R_2(\omega) = \frac{[Output2]}{[Input]} = H_B(\omega) H_F(\omega) (B(\omega) + T(\omega)) \tag{4.6}$$

where we have assumed that there is no interaction between the background soil and the rod. The differences of the measurements in then

$$R_{sub}(\omega) = R_2(\omega) - R_1(\omega) = H_B(\omega) H_F(\omega) T(\omega) . \tag{4.7}$$

Figures 4.7, 4.8 and 4.9 show examples of the collected and subtracted data for $R_1(\omega)$, $R_2(\omega)$ and $R_{sub}(\omega)$, respectively.

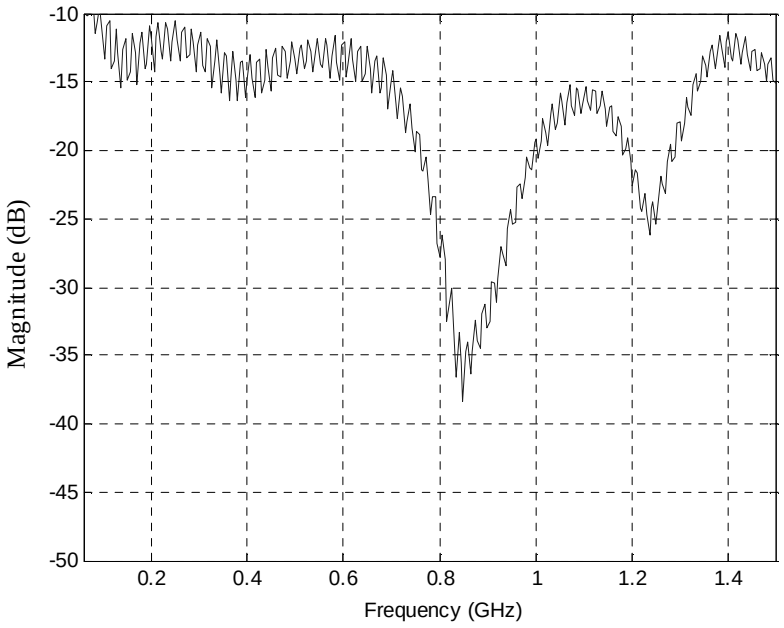

Figure 4.7. Frequency response of the background in the absence of a rod ($R_1(\omega)$).

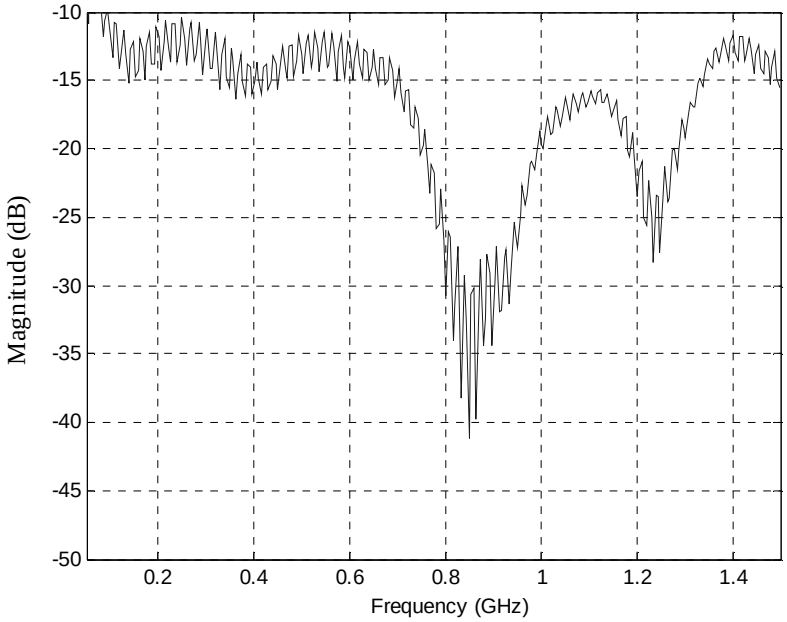

Figure 4.8. Frequency response of the background and a rod ($R_2(\omega)$).

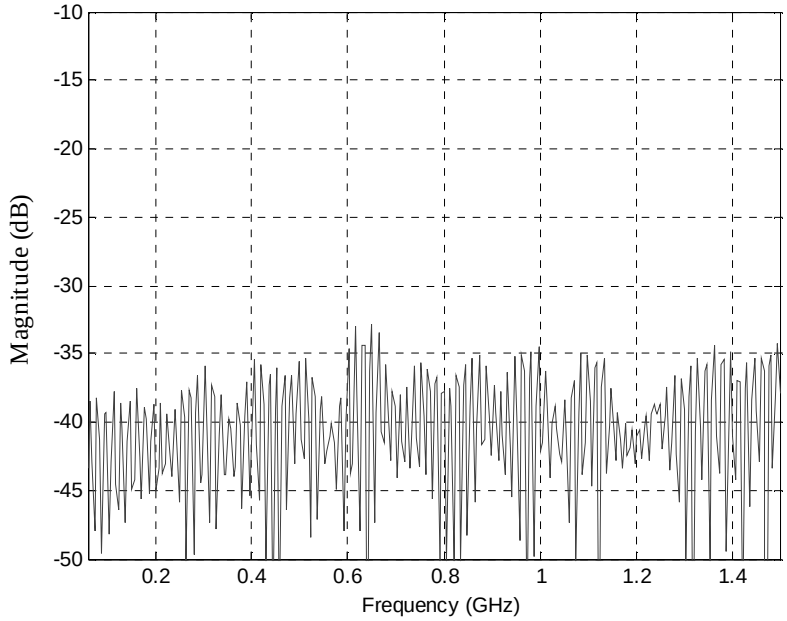

Figure 4.9. Difference between $R_2(\omega)$ and $R_1(\omega)$ ($R_{sub}(\omega)$).

From the above results, it is found that $R_1(\omega)$ and $R_2(\omega)$ are dominated by the responses from the antenna feed and the soil surface. As a result, the subtraction yields a very weak signal (approximately –30 dB below the raw data). Note that the fast variation in the data shown in Figures 4.7 and 4.8 is caused by the interference between the

multiple reflected signals in the cable connected between the network analyzer and the antenna.

In practice, the above subtraction is not perfect because there are variations in the system over time. To reduce this effect $R_{sub}(\omega)$ is inverse Fourier transformed to the time domain, and the residue from the subtraction at early time (due to the antenna feed and the background) is gated out as shown in Figure 4.10. The remaining signal is then Fourier transformed back to the frequency domain to obtain a better estimate for $H_B(\omega) H_F(\omega) T(\omega)$.

From (4.7) it follows that if $H_B(\omega) H_F(\omega)$ is known, $T(\omega)$ can be found, and a direct comparison with the DDA code is possible.

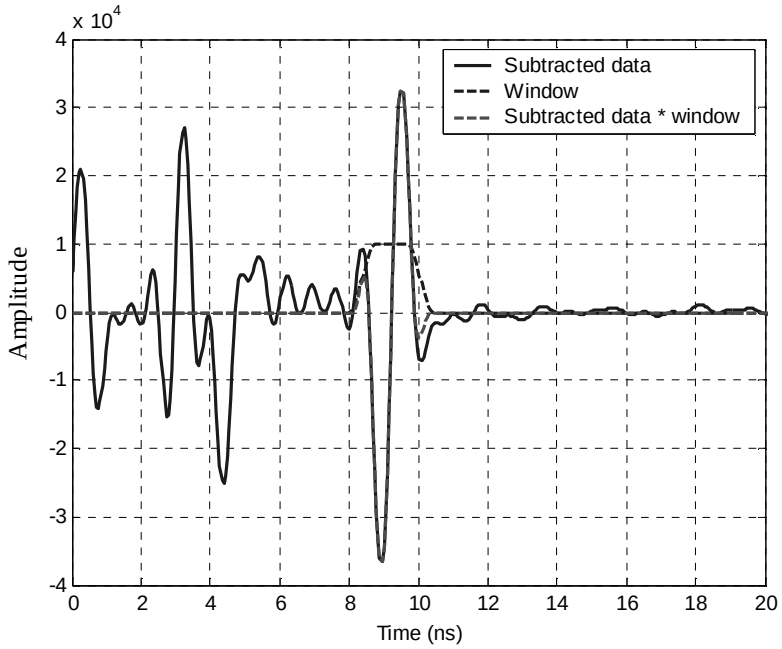

Figure 4.10. Subtracted data in the time domain and a late-time window to remove early time clutter

4.3 Finding the Antenna Response $H_B(\omega) H_F(\omega)$

An additional experiment must be done to obtain the antenna response. The setup and procedure are similar to those shown in Figures 4.6(a) and 4.6(b), except that a long, thin wire was used as the target. The frequency response of the wire is known to be

approximately independent of frequency (shown in Appendix A), which permits easy estimation of the antenna response.

The background measurement was done exactly the same as shown in Figure 4.6(a). For the response of the background and thin wire, the latter was placed between the antenna and the ground so that the angle between the thin wire and each of the antenna elements is 45 degrees.

If coupling between the ground and wire is ignored, subtraction yields

$$R_{sub,w}(\omega) = H_B(\omega) H_F(\omega) W(\omega) \tag{4.8}$$

where $W(\omega)$ (equal to a constant C) is the frequency response of a thin wire. When absolute measurements are not being performed, C can be set to be 1. The result is shown in Figure 4.11. By dividing (4.7) by (4.8), the frequency response of the rod $T(\omega)$ can be obtained as shown in Figure 4.12.

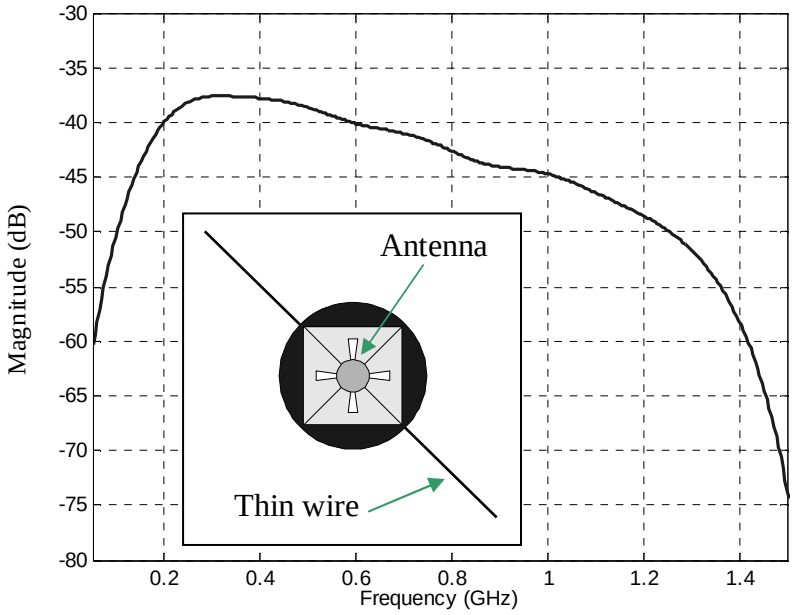

Figure 4.11. Response from a long thin wire at the surface, which is proportional to the antenna response $H_B(\omega)H_F(\omega)$.

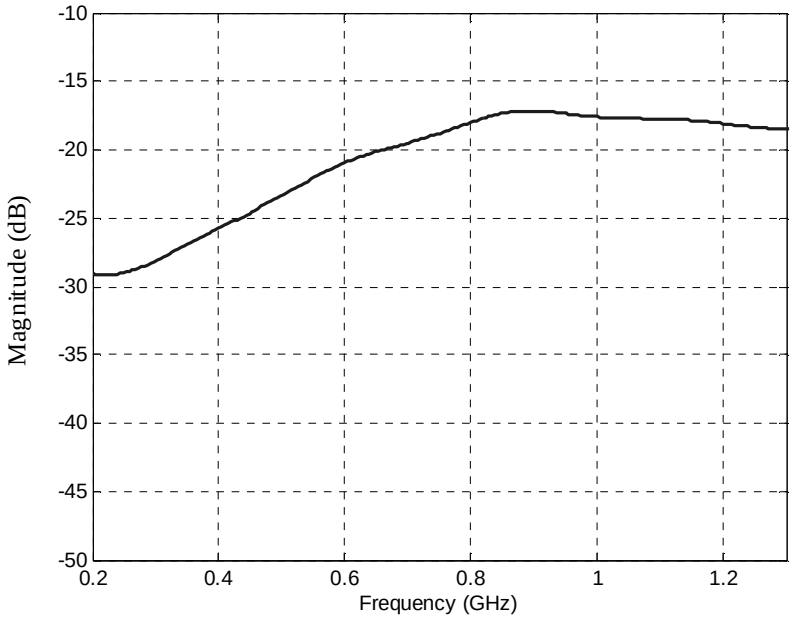

Figure 4.12. The frequency response of the rod $T(\omega)$, obtained by applying the window in the time domain and dividing by the antenna response.

4.4 Comparison of Experiment and DDA Predictions for $T(\omega)$

Figure 4.13 compares the DDA-calculated rod responses with $T(\omega)$ acquired via the above procedure for two rods of the same dielectric constant (30.0), but different diameters (0.5 and 1.0 inches). Figure 4.14 shows a similar comparison for two rods with the same diameter (1 inch), but different dielectric constants (2.4 and 30.0). In these results the calculated data have been weighted by a constant factor that accounts for antenna gain and RF losses. (The same factor is used in all of these results.) The rods with dielectric constants of 2.4 and 30.0 are plastic and methanol, respectively. All of the rods are shown in Figure 4.15. The above comparison shows good agreement between the model and the measurement although there are some discrepancies which arise because of three factors. First, the window applied in the time domain to remove the early-time clutter causes some distortion at both ends of $T(\omega)$ as can be seen in Figure 4.13(a) and 4.14(a). Second, the dielectric constant of the hose we used differs from that of methanol. This can induce errors in the magnitude of $T(\omega)$. Finally, small timeshifts in Figure 4.13(b) and 4.14(b) between the measured and calculated data may arise because the dielectric constant of the soil may not be exactly 5.

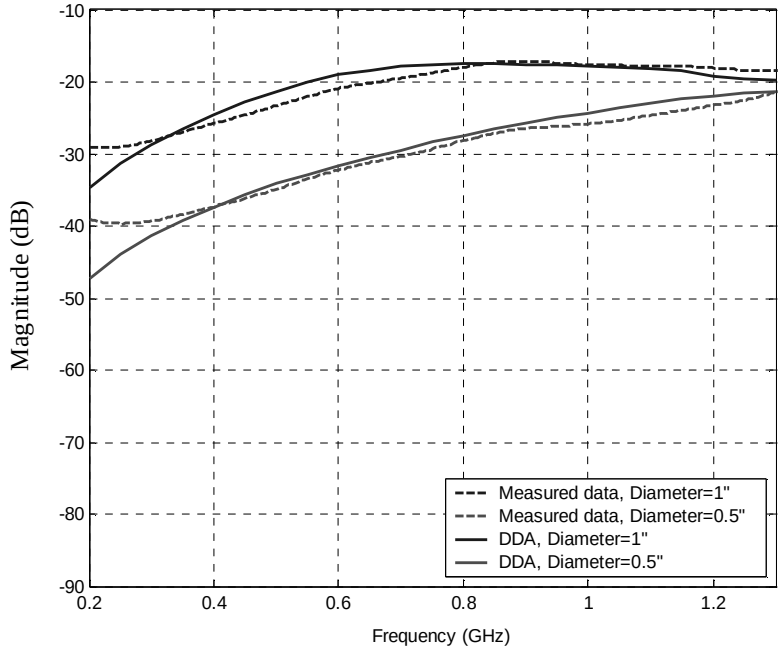

(a)

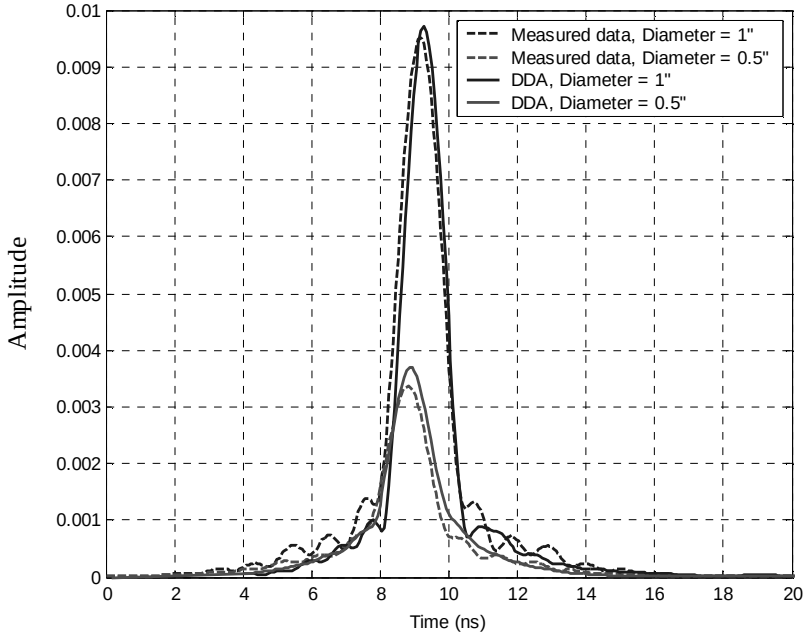

(b)

Figure 4.13. Comparison of measured and DDA-calculated backscatterer for two rods with the same permittivity and different diameters. (a) Frequency response. (b) Time-domain response.

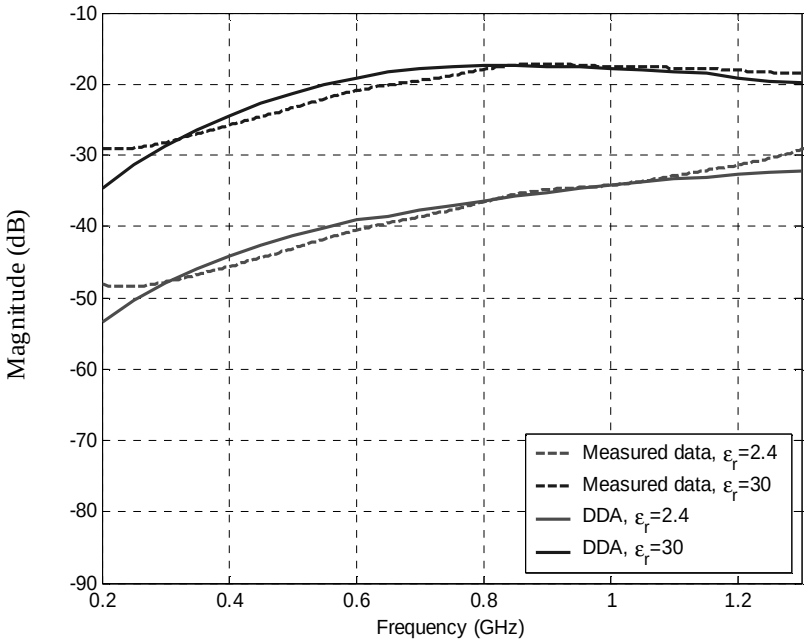

(a)

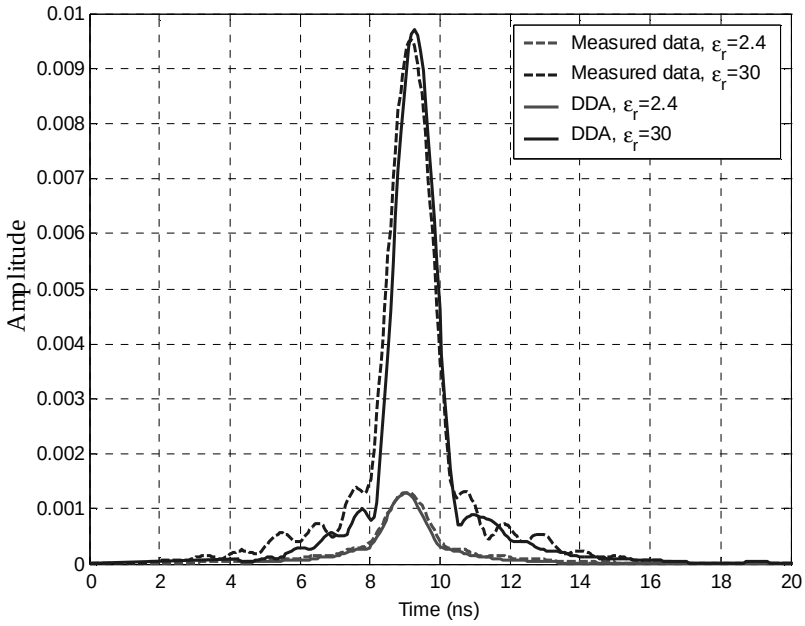

(b)

Figure 4.14. Comparison of measured and DDA-calculated backscatterer for two rods with the same diameter and different permittivities. (a) Frequency response. (b) Time domain response.

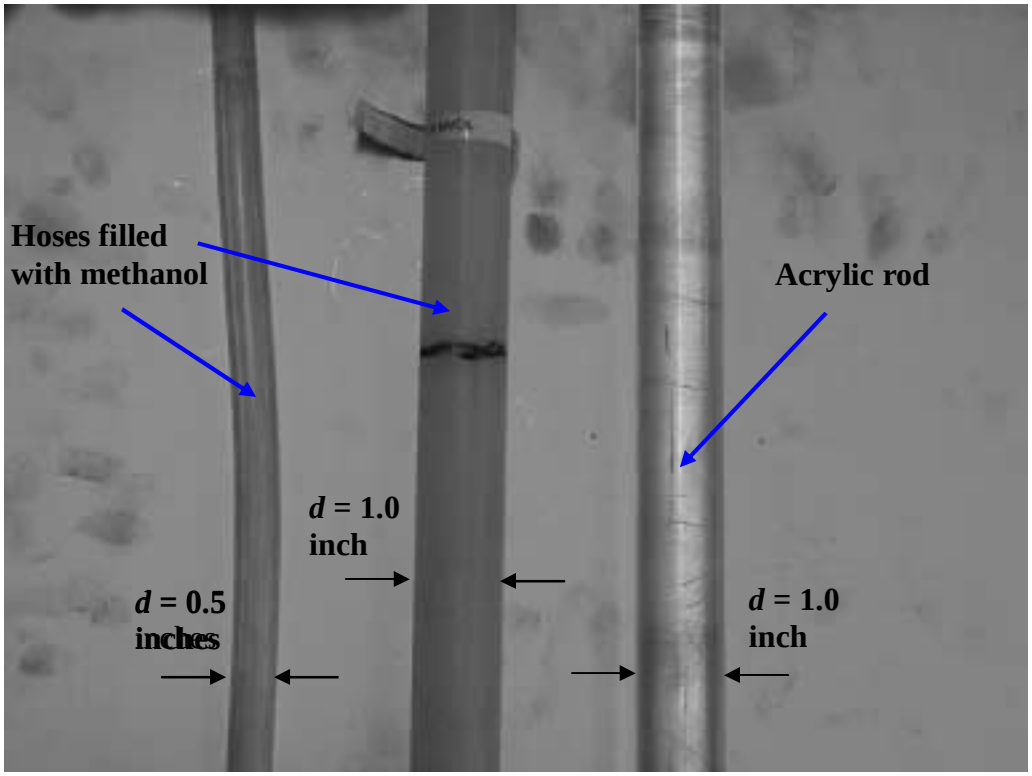

Figure 4.15. Dielectric rods used in the experiment. Note that "*d*" stands for diameter.

4.5 Summary

The measurement approaches used at the OSU/ESL test site for collecting wide band, dual-polarized data of buried rods made of plastic and methanol have been discussed. Both position-scanned and single-position data were collected. Burying the rods disturbed the soil, which produced clutter of a magnitude similar to the dielectric rod return. Single-position measurements were found to provide better data for model validation. Comparisons of calculated and measured returns from buried rods show good agreement. This demonstrates that the DDA code can be used to accurately compute the fields scattered from a root structure for a wide range of dielectric constants and diameters.

5.0 Case Studies of Effects of Roots on GPR

The simple model developed in Chapter 4 for simulating GPR scans will be used to study scattering from the root structure shown in Figure 2.1(b). This chapter begins with a discussion of how root scattering varies as a function of root dielectric constant and diameter. Comparisons between experimental and simulated GPR scans will be presented. Two issues concerning the effects of roots on GPR system are studied, namely, the increase in clutter level and root attenuation of targets signatures.

5.1 Properties of Root Scattering

Before presenting a comparison of measured and modeled results, we first use the model to illustrate the dependence of root scattering on dielectric constant and frequency. A long, thin, isolated root will be examined. The results can be contrasted with those in Chapter 3 for the thin, infinitely long root. The configuration for this case is shown in Figure 5.1(a) and 5.1(b). Note again that the radiating source is modeled as two perpendicular short dipole elements oriented in the x and y directions (assuming that the interface lies in the x-y plane). Throughout this chapter, we will assume the dielectric constant of roots (ε_d) to be 20+10i which is calculated using the Debye Cole dual-dispersion model described in Appendix B. The soil dielectric constant and conductivity are 5 and 0.0035 S/m, respectively, as measured by the Army Research Laboratory (ARL). The details are explained in Appendix C.

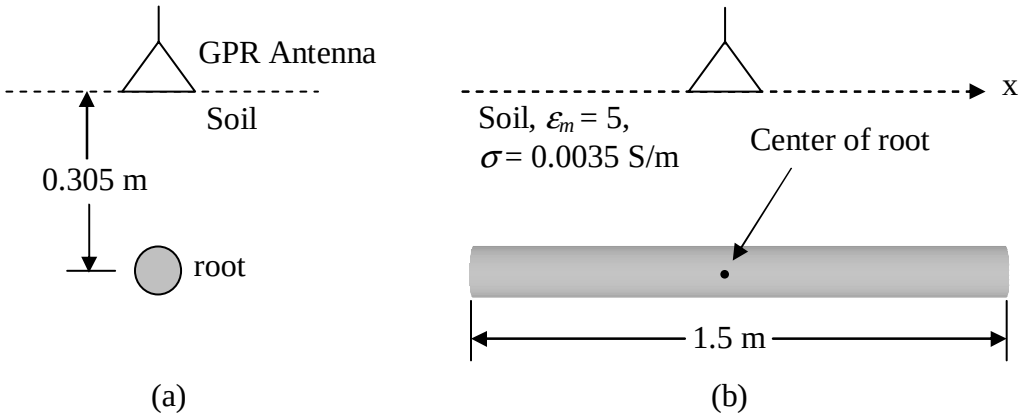

Figure 5.1. Configuration of the GPR scan used to study the scattering characteristics of a long, thin root with dielectric constant 20+10i. (a) Front view. (b) Side view.

The fields scattered from the root are computed at the antenna and are normalized by the incident field that would exist in the absence of the root at the location of the root's centroid. Figure 5.2 shows the calculated, scattered electric field intensity for the x polarization as a function of both diameter measured in wavelengths (D/λ_d) and root dielectric constant.

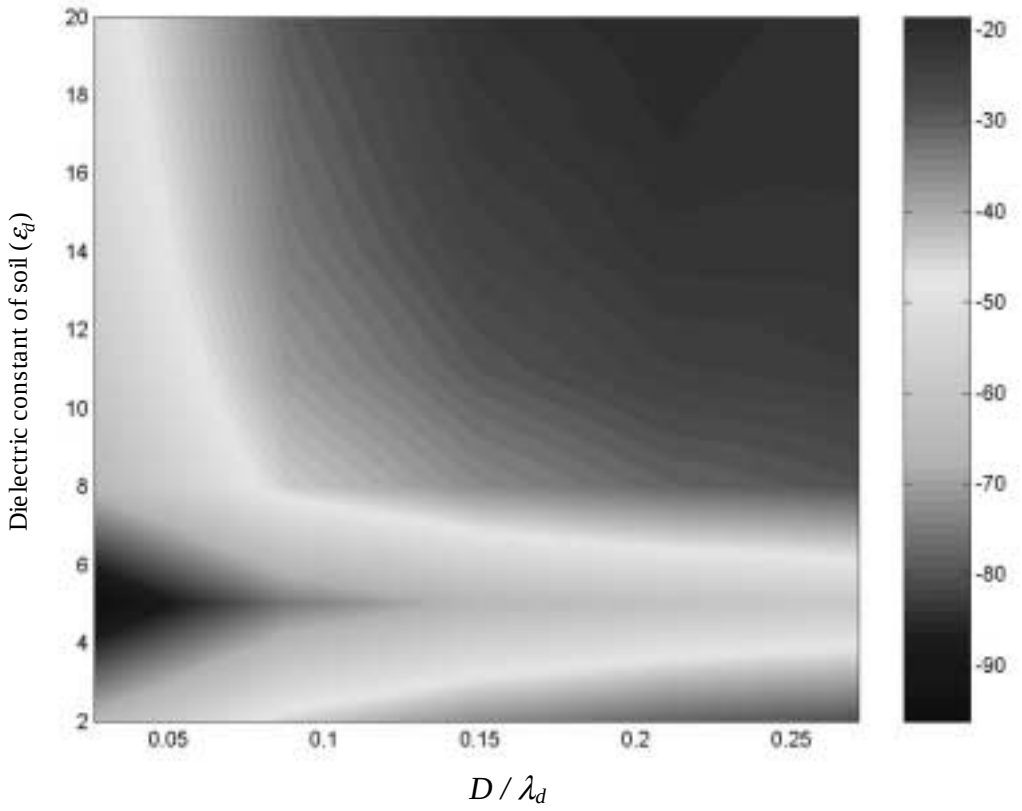

Figure 5.2. Magnitude of the scattered field intensity (in dB) as a function of root diameter in wavelengths and dielectric constant.

As expected, the magnitude of the field scattered from a long thin root increases as the diameter increases. It also increases with the dielectric contrast $\varepsilon_c = \varepsilon_d/\varepsilon_m$ where ε_m is the dielectric constant of the soil. These simple dependencies on $|\varepsilon_c - 1|$ and D/λ_d were also found in Chapter 3 for an infinitely long cylinder described by equation (3.11).

5.2 Approximations to Reduce Model Complexity

It was observed during early tests of the DDA code that taking into account all the roots in Figure 2.1(b) at every antenna position is computationally expensive, because of the large number of unknowns. Fortunately, further approximations can be employed to reduce the size of the problem.

In general, soil is lossy and the antenna has mildly directional radiating and receiving patterns. This implies that roots far from the antenna and outside the main pattern will have little contribution to the scattered fields. Thus, instead of considering all roots at each antenna position, it is sufficient to consider only those roots that both lie within some distance of the source and are within the transmitting/receiving patterns of the antenna. In this work we specify that the soil has a dielectric constant of 5, conductivity of 0.0035 S/m, and that the antennas are described by dipoles. As a result, only scattered fields caused by root segments within the cone shown in Figure 5.3 need to be considered in the calculation. The angle θ is found to be 76.8°, which is defined by the criterion that the incident field intensity at Point P is at least 25 dB below that at Point Q.

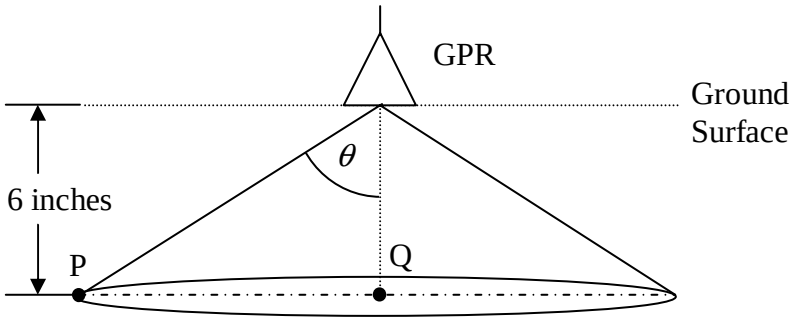

Figure 5.3. Only roots in a circular cone shape are considered in the scattering computation.

Another simplification involves the condition in equation (2.25), namely,

$$\left|\sqrt{\varepsilon_c}\right| k\,(2a_{\max}) \le 1. \tag{5.1}$$

The above condition leads to an overly fine sampling of the problem when a large number of roots are taken into account, and it is reduced to

$$\left|\sqrt{\varepsilon_c}\right| k\,a_{\max} \le 1. \tag{5.2}$$

Figure 5.4 shows good agreement between computed scattered field intensities as a function of frequency after the above approximations are applied. Here, the depth of the roots is 6 inches, and their dielectric constant is 20+10i. The antenna is positioned above the large root mass in Figure 2.1(b). This approach reduced the number of unknowns at 1 GHz from 31,152 to 9,960, which makes the calculation more efficient.

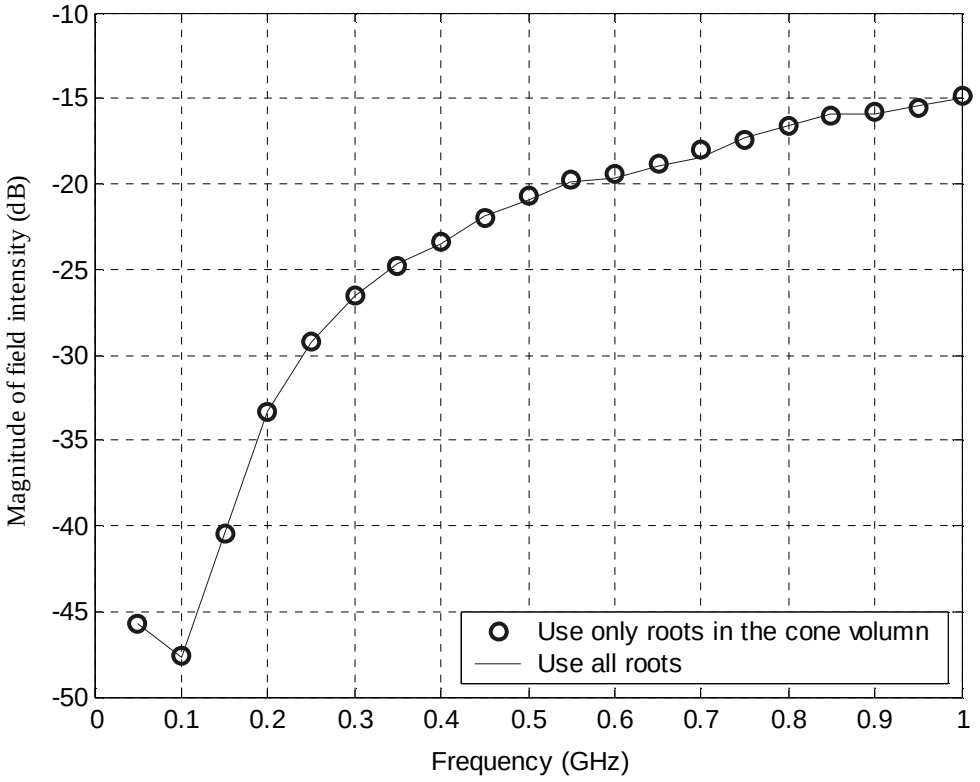

Figure 5.4. Comparison of scattered field intensities computed when considering all roots discretized using Equation (5.1) and only those roots that fall within the circular cone discretized using Equation (5.2).

5.3 Comparison Between Modeled and Measured GPR Data

To demonstrate that the model can reproduce fields scattered from a realistic root system, model results were compared with data collected at Eglin AFB along the path shown in Figure 5.5. Since it was shown in the first report [1] that the radar is insensitive to the roots for frequencies higher than 1.0 GHz, we will only consider the frequency range from 0.05 to 1.0 GHz. The frequency step for the measured data is 4.875 MHz with three inch increments in position, but for the simulated data, the frequency step is 50 MHz with 0.1333 m increments. Note that in the simulation, the depth of the root structure is set to be 6 inches. Figure 5.6 shows the calculated and measured data plotted as functions of time delay and scan position. Within the modeled interval, similarities between the measurement and model can be seen. The arrows indicate to the positions at which strong responses are expected and they agree well with the root location shown in both figures. Some disagreement between the measurement and model can be attributed to our two-dimentional (2-D) root model: the true root structure has some variation in depth, but the model places all roots at a fixed depth.

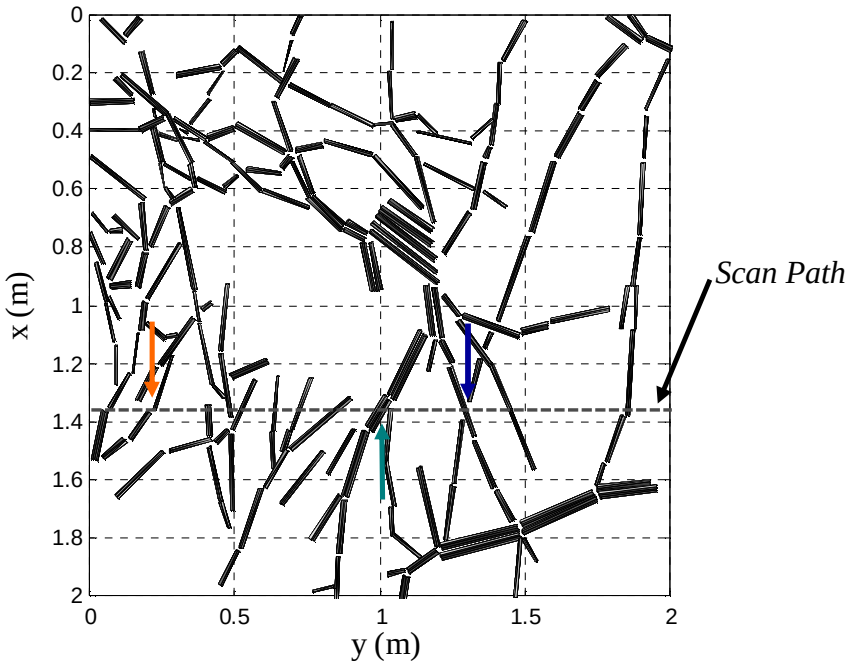

Figure 5.5. GPR scan path and root structure

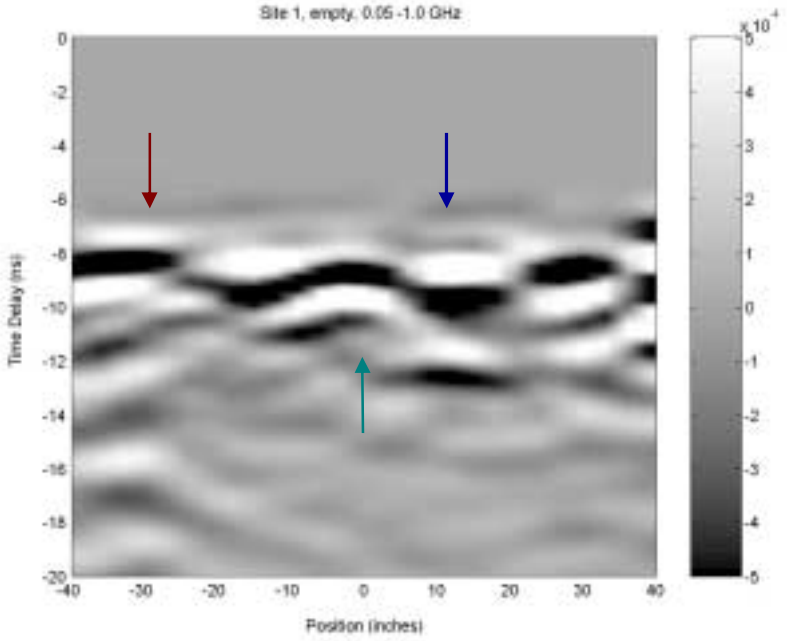

(a)

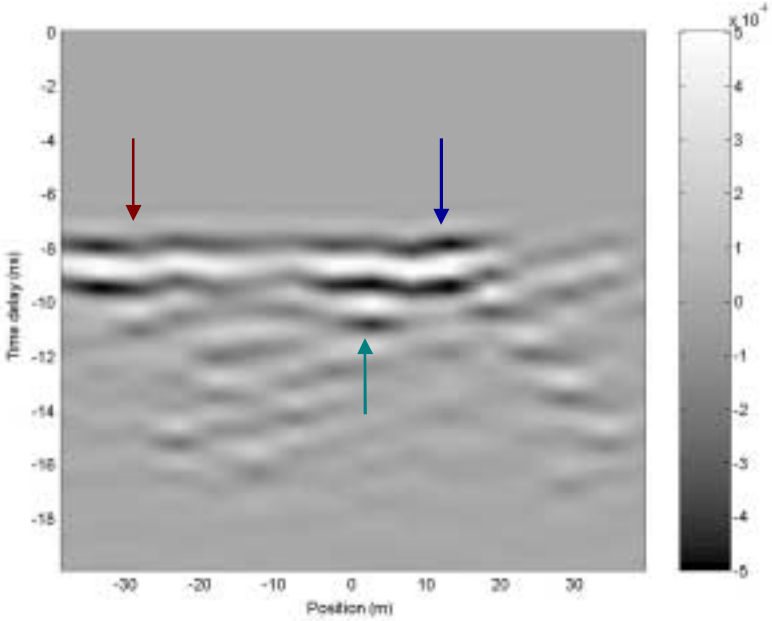

(b)

Figure 5.6. Comparison of measurements and model predictions. (a) Experimental data. (b) Model simulation.

5.4 Case Studies of the Effects of Roots on GPR Systems

From the above comparison, it is evident that the model can predict root scattering fairly well. Hence, the model can be used with some confidence to study the effects of roots on GPR performance. We begin with a study of two issues: root generated clutter and the tendency of roots to produce target attenuation.

5.5 Target Detection in the Presence of Roots

We now evaluate the detectability of a known UXO target in a clutter field caused by root scattering. A complete analysis of this topic is beyond the scope of this investigation, but useful insight can be drawn from a relatively simple analysis.

It is assumed that the radar emits a (complex) waveform *h(t)*. We further assume that the target response is dominated by the specular return, which can be expressed as $Ah(t-\tau_1)$, in which τ_1 is a time delay and *A* is a complex scalar that accounts for both propagation losses and a possible change in phase due to reflection. The root return is also approximated by its specular contribution, which we write as $Bh(t-\tau_2)$ in which τ_2 and *B* are an appropriate phase shift and a complex scalar, respectively. The effects of receiver noise are assumed to be insignificant in comparison to the clutter. The detection problem can be expressed as follows:

$$x(t) = \begin{cases} Ah(t-\tau_1) + Bh(t-\tau_2), & \text{if } H_1 \\ Bh(t-\tau_2), & \text{if } H_0 \end{cases} \tag{5.3}$$

in which *x(t)* is the measured signal, and H_0 (H_1) is the hypothesis that the target is absent (present) in the measurement.

An appropriate technique for detecting such signals involves the matched filter, in which the received waveform is convolved with the time-reversed, conjugated, transmitted waveform. We find

$$x(t) \otimes h^*(-t) = \begin{cases} Av(t-\tau_1) + Bv(t-\tau_2), & \text{if } H_1 \\ Bv(t-\tau_2), & \text{if } H_0 \end{cases} \tag{5.4}$$

in which *v(t)* is the response of the matched filter to the transmitted waveform

$$v(t) = h(t) \otimes h^*(-t)\,. \tag{5.5}$$

A practical implementation of this concept would involve searching the matched filter output for local maxima of the magnitude (which, presumably, would be the maxima of *v(t)*). A detection decision would be required for each maxima.

If the roots and targets are always found at different depths, then detection can be as simple as range-gating the matched filter output and applying a threshold. The case of interest here, however, is when both the target and roots are in the same range bin. In that case, we can take $\tau_1 \approx \tau_2$. If v_0 is the maximum value of *v(t)*, then the detection problem is equivalent to a test of the scalar

$$u \equiv \frac{\max[\,|\,x(t) \otimes h^*(-t)\,|\,]}{v_0} = \begin{cases} |\,A+B\,|, & \text{if } H_1 \\ |\,B\,|, & \text{if } H_0 \end{cases}. \tag{5.6}$$

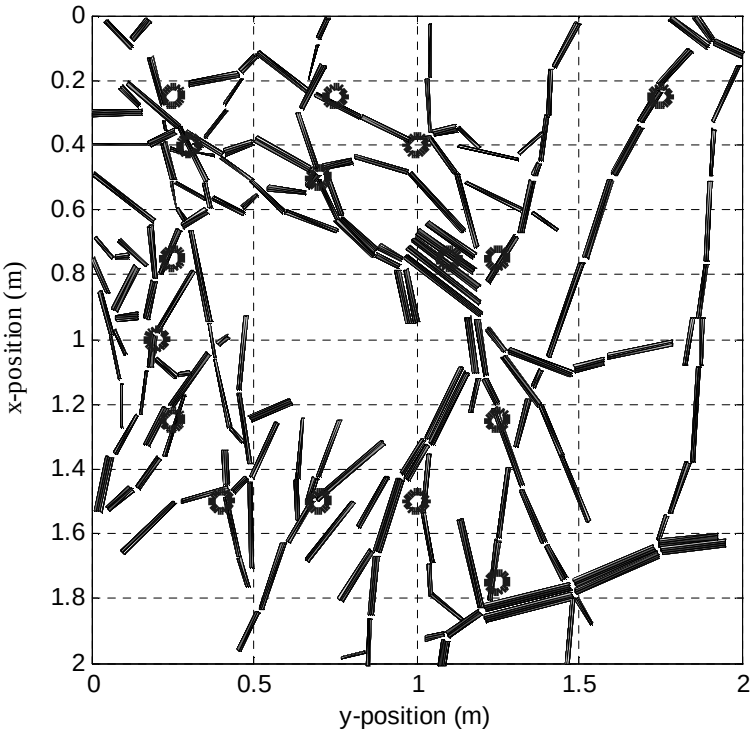

Figure 5.7. Sixteen chosen root locations.

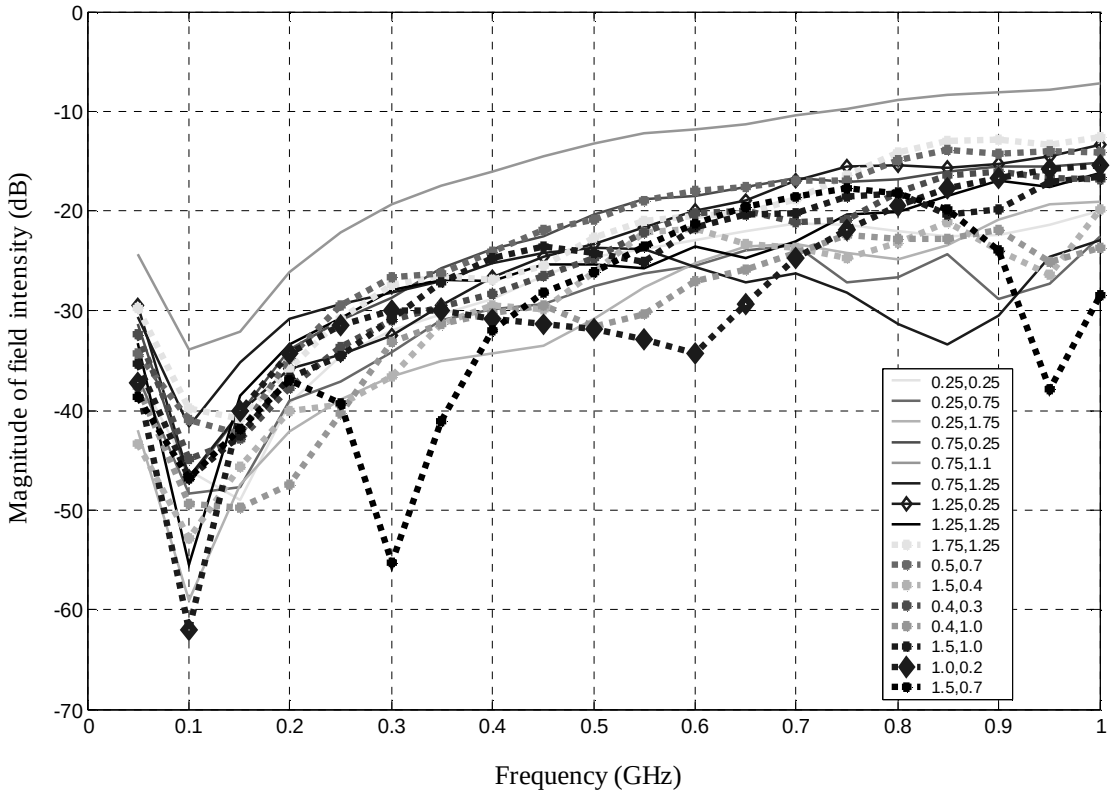

Figure 5.8. Sixteen examples of clutter spectra computed over known root locations.

When the probability densities of *A* and *B* are known, then one can formulate an optimal detection test for this problem. In the present case, however, the available information is limited, and less rigorous assessment is appropriate.

Consider first the density of |*B*|. Examples of clutter spectra for 16 locations chosen directly over roots (see Figure 5.7) appear in Figure 5.8. These data indicate that the clutter is strongly non-Gaussian. On the logarithmic (dB) scale used here, there is some degree of central tendency, and it is plausible to approximate the probability density values with a log-normal density *f(u)* given by

$$f(u)du = \frac{1}{\sqrt{2\pi}\sigma u} e^{-(\ln(u)-\mu)^2/(2\sigma^2)} du \tag{5.7}$$

where μ and σ are constants. Using the change of variable

$$v = \ln(u) \tag{5.8}$$

we obtain the alternate form

$$f(u)du = \frac{1}{\sqrt{2\pi}\sigma} e^{-(v-\mu)^2/(2\sigma^2)} dv \tag{5.9}$$

which shows that the logarithm of the independent variable u has a normal density in the transformed variable v with mean μ and standard deviation σ. If

$$s = 20\log_{10}(u) = \frac{20v}{\ln(10)} \tag{5.10}$$

is the value of the clutter return expressed in dB, then

$$f(u)du = \frac{1}{\sqrt{2\pi}\sigma'} e^{-(s-\mu')^2/(2\sigma'^2)} ds \tag{5.11}$$

which is a standard normal density with the following standard deviation and mean (both expressed in dB)

$$\begin{aligned} \sigma' &= 20\sigma/\ln(10) \\ \mu' &= 20\mu/\ln(10) \end{aligned}. \tag{5.12}$$

These quantities can be computed directly from the data expressed in dB.

Confidence intervals for this density are readily obtained from those for a standard normal density, and they permit us to define appropriate detection thresholds for a Neyman-Pearson receiver [28] (i.e., one which achieves a specified probability of false alarm.) For this receiver, knowledge of the density of A is not required to estimate the probability of false alarm. (They are, however, necessary to estimate the probability of detection.) For example, if the detection threshold for the target density in dB is set at $\mu'+1.28\sigma'$, then the probability of false alarm is 0.1. At a threshold of $\mu'+2.33\sigma'$ the false alarm probability is reduced to 0.01. The relevant false alarm rate is obtained by dividing these probabilities by the sensor's pixel area.

Use of the foregoing results is illustrated in Figure 5.9(a), in which we show a 105 mm shell signature at depth 0.35 m computed for several shell angles via FDTD [26]. Figure 5.9(b) defines the shell angle.[1] This target signature is superimposed with the average clutter spectra of Figure 5.8. The decision threshold (a function of frequency) for a false alarm rate of $0.01/m^2$ (assuming 1 m^2 sensor pixels) is also shown.

[1] The shell orientation in these results is nose-up, while real UXO signatures will typically be found nose-down. For the purposes of this analysis, however, the difference in the target signature will be small.

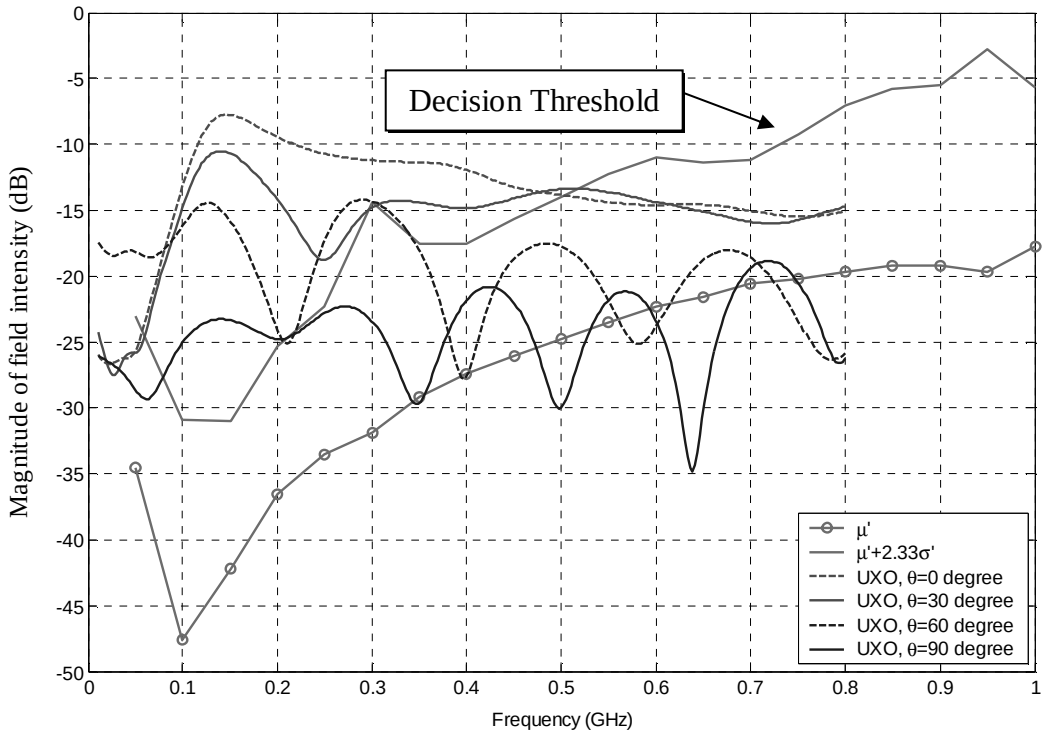

(a)

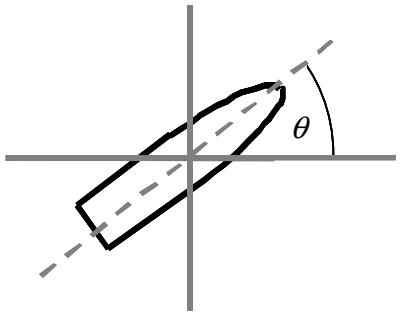

(b)

Figure 5.9. (a) Detectability calculations for a 105 mm shell in roots. The indicated line is the decision threshold for a false alarm rate of 0.01/m2. (b) Orientation of 105 mm shell as a function of θ.

The comparison in Figure 5.9(a) suggests that responses from the shell exceeds the mean root clutter level for most frequencies and shell angles. Nonetheless, it is only in the frequency regime below 0.5 GHz that the target signature exceeds the threshold required for a $10^{-2}/m^2$ false alarm rate. Based on these data, one expects better performance for low-frequency waveforms, and significant challenges in achieving very low false-alarm rates.

5.6 Target Signature Attenuation

Next, consider the UXO-shaped lossy dielectric target shown in Figure 5.10 (10 cm diameter by 40 cm length) with dielectric constant 1+20*i* placed under the root mass at depth 0.3 m. The target orientation is parallel to the vertical axis. The antenna position is directly above the root mass and polarized in the same direction. To isolate the effects of root-related attenuation, frequency responses are computed for the cases when the target is and is not present. The result of subtracting these two data sets is compared with the response from the target when no roots are present. The comparison in the frequency and time domains are shown in Figure 5.11(a) and 5.11(b). Note that in the calculation, we include the interaction between the roots and target. In these results it is important to disregard the relative magnitudes of the target and root responses. Because of limitation in the DDA code, the target (a good conductor) was approximated by a lossy dielectric (ε_r=1+20*i*), which has an abnormally weak return.

The results suggest that roots have a relatively small effect on the target signature. They attenuate the target response slightly at high frequencies, and they introduce a small time delay. Note that the attenuation can reach 3 to 4 dB at the highest frequency. These effects can be attributed to distortion in the incident field. Figure 5.12, 5.13 and 5.14 are plots of the calculated field magnitude at different positions normalized by the incident field for a depth of 0.3 m. The figures show the response at the frequencies 0.1, 0.6 and 1.0 GHz, respectively. The purple triangular shape illustrates the position of the antenna which is modeled as a dipole with polarization pointing down the page. It can be seen that at relatively high frequencies, the root-induced distortion of the incident field can reach 3 dB, but for low frequencies this distortion is relatively small.

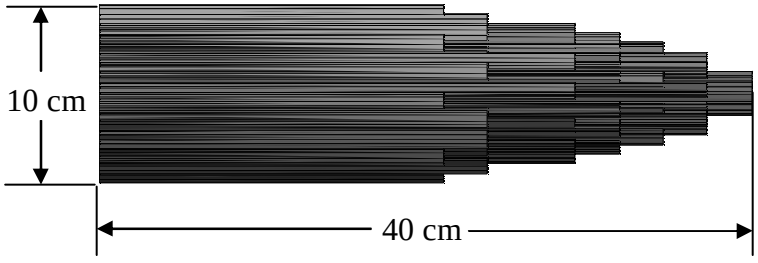

Figure 5.10. UXO-shaped target modeled with cylinders

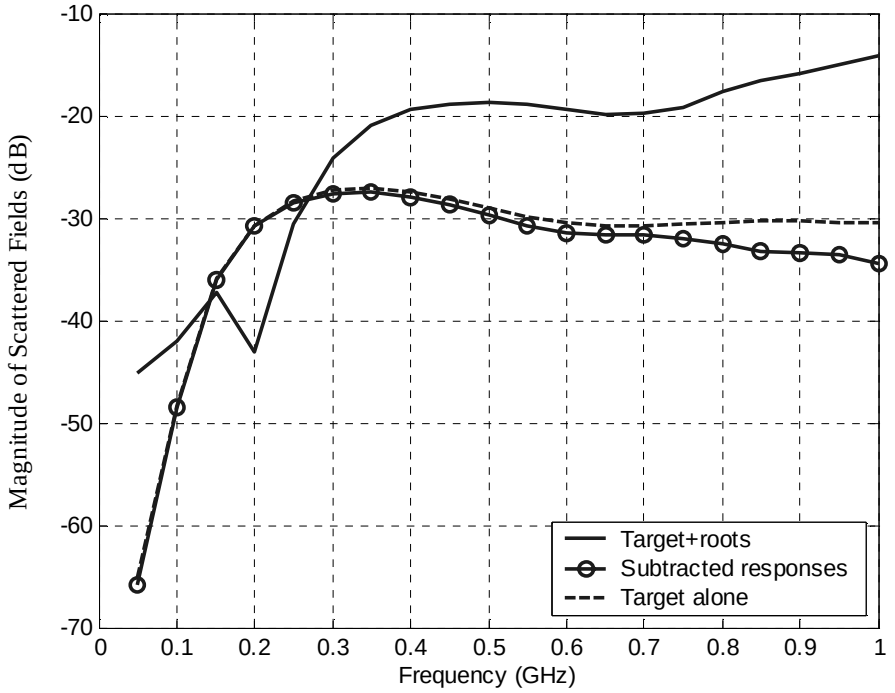

(a)

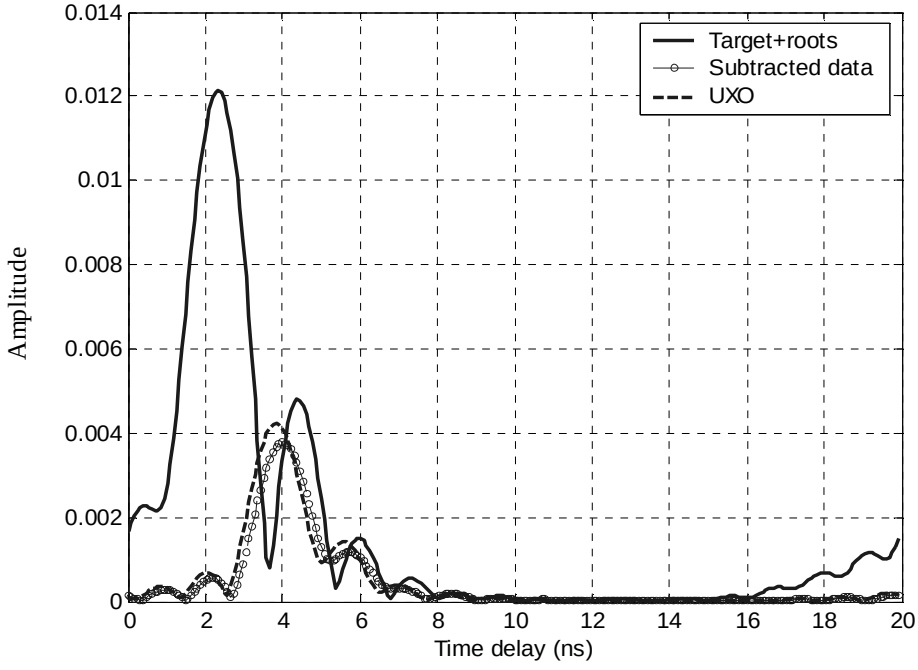

(b)

Figure 5.11. Comparison of responses from a target when roots are and are not present. (a) Frequency domain. (b) Time domain.

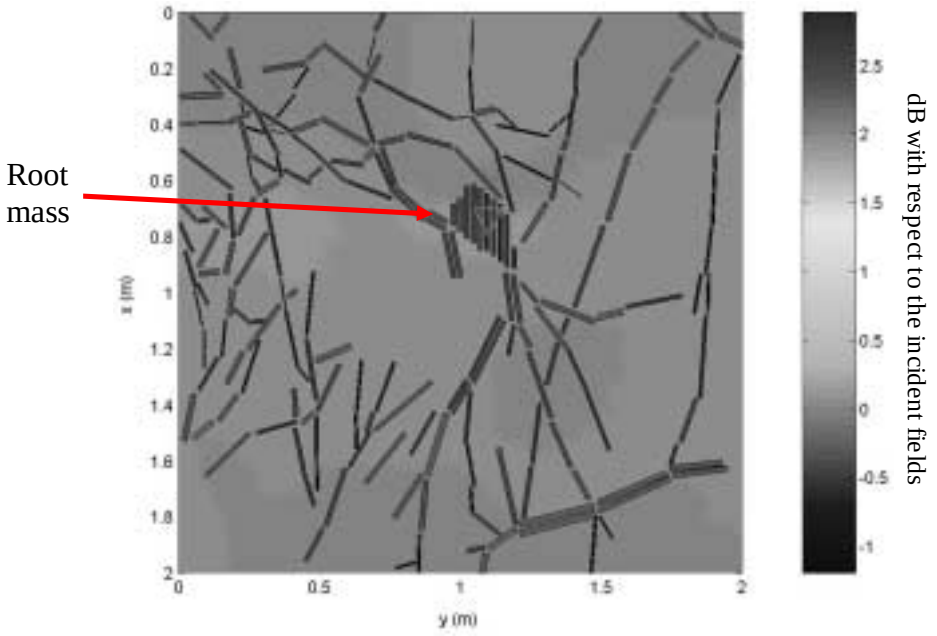

Figure 5.12. Distortion of the incident field magnitude at the depth 0.3 m for 0.1 GHz.

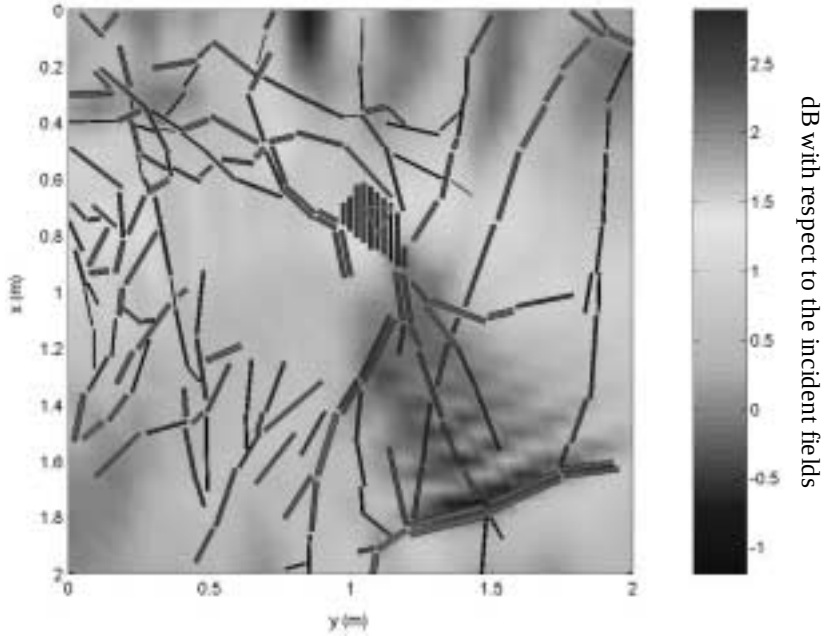

Figure 5.13. Distortion of the incident field magnitude at the depth 0.3 m for 0.6 GHz.

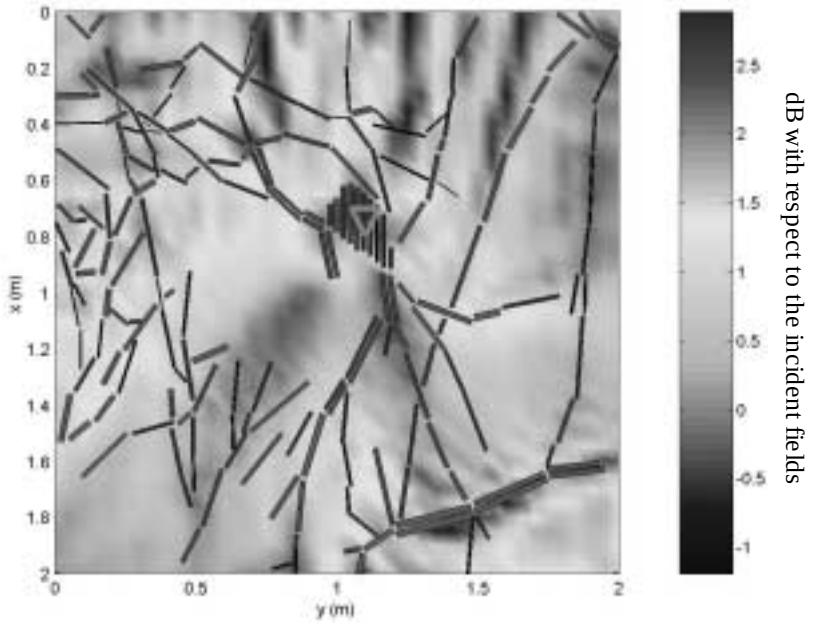

Figure 5.14. Distortion of the incident field magnitude at the depth 0.3 m for 1.0 GHz.

5.7 Imaging of Simulated GPR Data

The GPR response of a point target extends for a significant distance (more precisely, it produces a hyperbolic arc) in the along-scan dimension (more precisely, it produces a hyperbolic arc), which complicates target position estimates. One can, however, use imaging techniques to both localize the target signature and to increase the signal to noise ratio.

In this section we explore the effectiveness of imaging in the presence of root clutter. The imaging algorithm used here is based on the so-called "frequency-wavenumber (ω-k) migration" technique used in exploration geophysics. A detailed derivation of this technique is explained in several works [29-31]. For a brief review, one can refer to [32].

The approach that we will employ here is based on the scalar wave equation and the concept of the "exploding reflector" model [33]. The latter can be explained as follows. Assume that a GPR antenna collects data $f(x,z=0,t)$ where x is the scan dimension. The signal scattered back from a target at the antenna is the same as that received by a passive sensor when (a) the target becomes a source of radiation and (b) the velocity of wave propagation is reduced by a factor of 2.

The spectral representation of the measured data *f(x,z=0,t)* can be written as

$$F(k_x, z=0, \omega) = \int dx \int dt \; f(x, z=0, t) e^{+i\omega t - ik_x x} \; . \qquad (5.13)$$

Since we use the exploding reflector model, the field distribution of interest is *f(x,z,t=0)*. It is possible to show that this distribution given by

$$f(x, z, t=0) = \frac{1}{(2\pi)^2} \int dx \int dk_x \; e^{+ik_x x} F(k_x, z=0, \omega) e^{+iK_z z} \qquad (5.14)$$

where $K_z = \sqrt{k^2 - k_x^{\,2}}$ and $k = 2\omega / v$. The field distribution in Equation (5.14) will be plotted as an image. In evaluating the transforms in Equation 5.13, we apply a weighting function, i.e., a two-dimensional window, to *f(x,z=0,t)*, which restrict the images to the center of the field of view.

The effectiveness of imaging is illustrated in Figure 5.15(a), which shows the normalized time-domain response of a UXO-shaped target buried at a depth of 0.55 m under the root mass. Figure 5.15(b) shows the normalized radar image. The bright spots in the image correspond to the positions of the root mass and the target, and it is evident that roots can produce strong image artifacts. This suggests that imaging is not necessarily an effective means of clutter suppression. Figure 5.16 shows the image of the target in the absence of roots. The data were normalized by the same factor used in Figure 5.15(b). By comparing the above figures, it is found that roots can attenuate the relative magnitude of the image, but the effect is quite small.

From the discretized root representation in Figure 2.1(b) it is evident that, for GPR, roots are more like discrete scatterers than random media. As a result, image of the roots may be of interest also. An example is shown in Figure 5.16, which presents the image of Figure 5.6(b). It can be seen that the locations of the bright spots indicate the positions of roots. The absence of a return near the initial and final ends of the scan is the result of the window function.

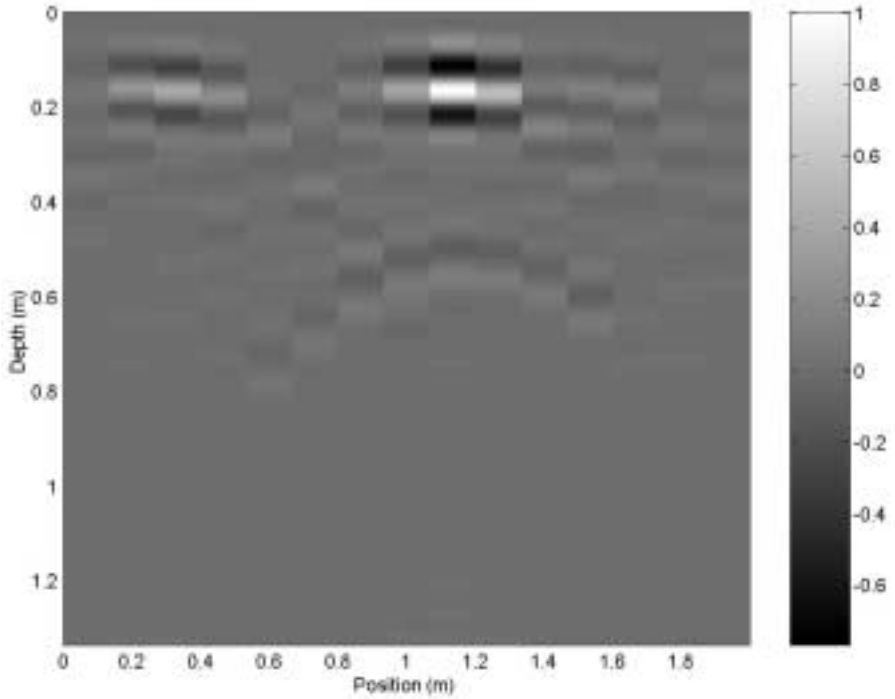

(a)

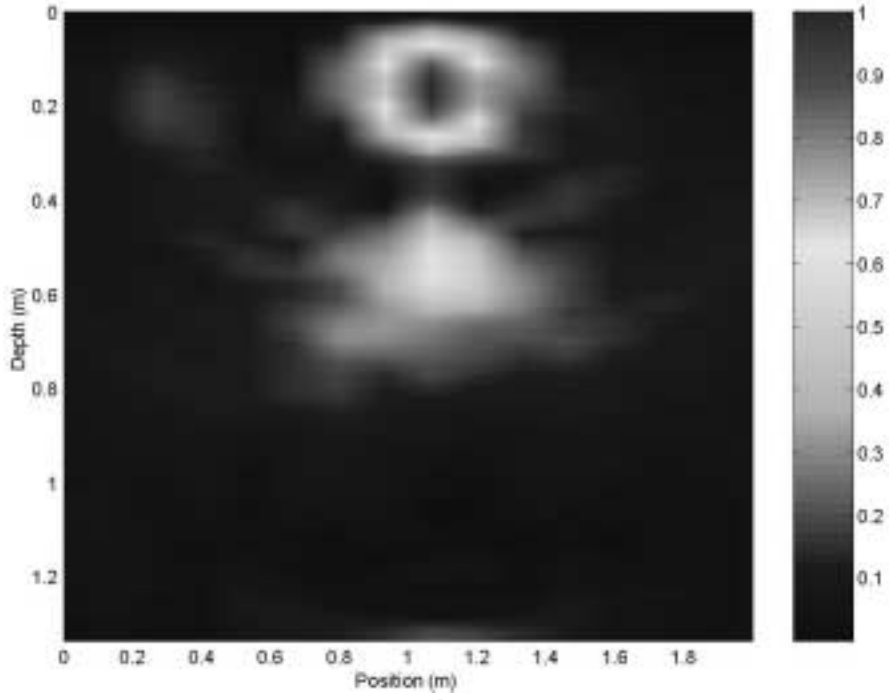

(b)

Figure 5.15. (a) Time domain response of a UXO-shaped lossy dielectric target. (b) Image of Figure 5.15(a).

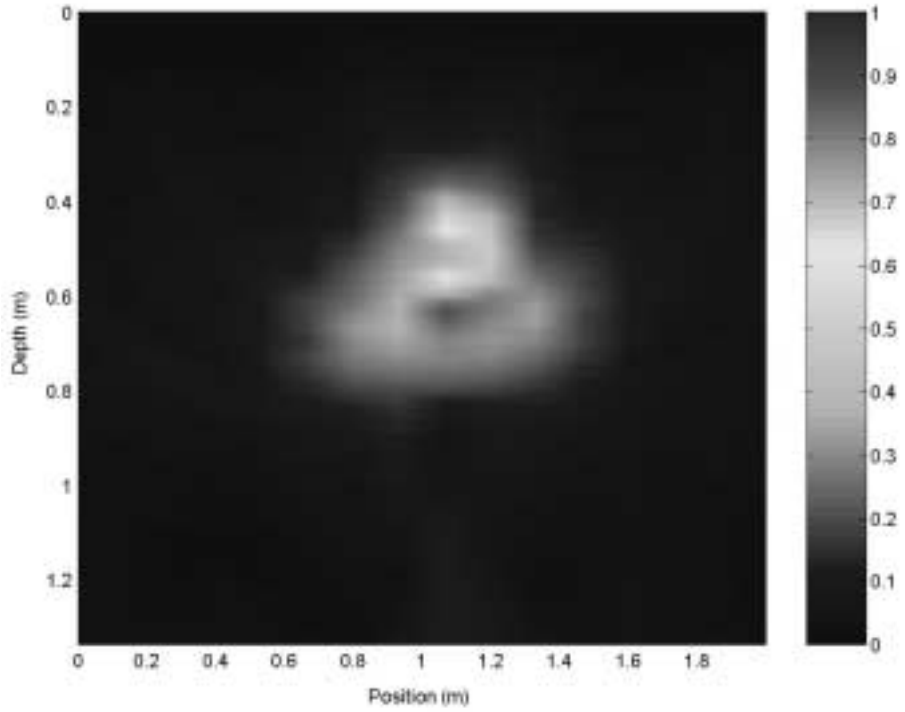

Figure 5.16. Image of the lossy dielectric target.

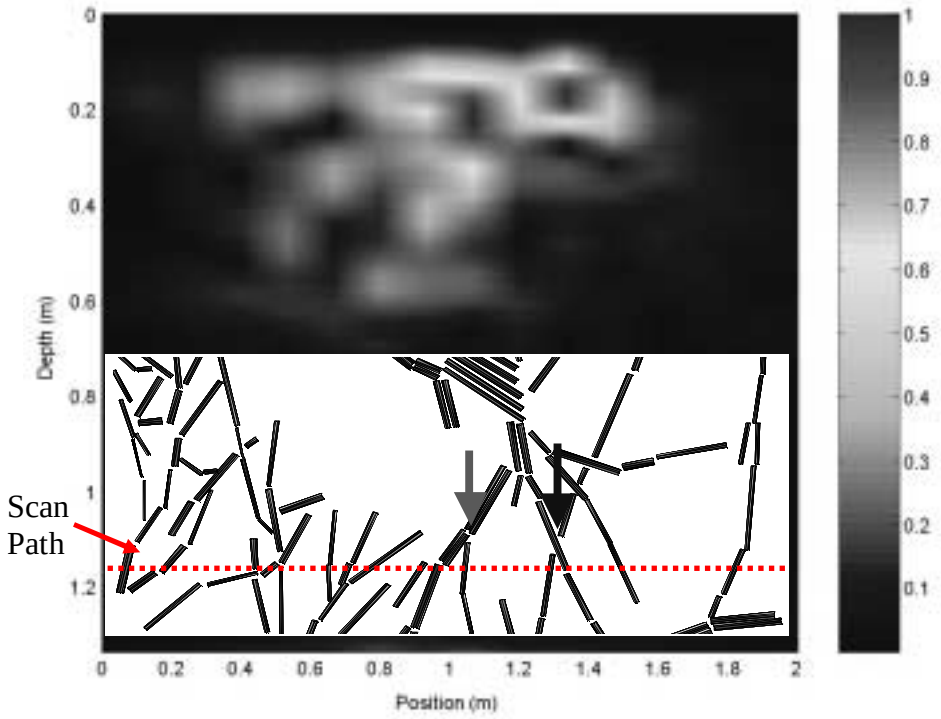

Figure 5.17. Image of Figure 5.5(b).

5.8 Summary

The scattering characteristics of a long, thin root as a function of its diameter in wavelengths (D/λ_d) and dielectric contrast relative to the medium (ε_c) have been studied. It was found that the scattered field intensity is proportional to D/λ_d and $\left|\varepsilon_c - 1\right|$. These simple dependencies were also found in Chapter 3 for an infinitely long cylinder. Comparisons of measured and simulated GPR scans showed that the DDA model is adequate to predict root scattering. Some discrepancies were noted and have been attributed to the fact that the modeled roots were all buried at a depth of at 6 inches, but the true root structure has some variations in depth. Further studies showed that roots increase the clutter level, which can cause problems in target detection. Based on the simulated data, better performance can be expected by operating the system at lower frequencies. Roots can also distort targets' response, but the effect is relatively small. Finally, experiments with imaging suggest that roots behave more like discrete scatterers than like a continuous random medium. As a result, radar images show distinct returns from roots, which are not immediately distinguished from targets.

6.0 Conclusions and Future Work

In this report a root structure obtained during experiments performed at Eglin AFB, FL was studied in detail. These roots were discretized and represented by an ensemble of cylindrical segments having variable radii. Scattering from the above cylinders was computed via the discrete dipole approximation (DDA) algorithm, which is an efficient technique for computing scattering from dielectric bodies. As a test, our DDA code was applied to the problem of plane wave scattering from a cylinder. Comparisons of the radar cross section computed by DDA and by a body of revolution (BOR) code showed good agreement.

The exact solutions for both TM and TE plane-wave scattering from an infinite dielectric cylinder were reviewed, and small radius approximations were derived. The approximate solutions have a simple form, which illustrates how scattered fields vary as a function of cylinder diameter and frequency. The results indicate that the magnitude of fields scattered from a cylinder increases as the cross-sectional area of the root and the permittivity contrast. We also presented two so-called "universal curves," from which the magnitude of the scattered fields can be found directly for any cylinder diameter or permittivity.

Use of the DDA algorithm to model GPR scans was also discussed. In this work the GPR is assumed to use a surface-contacting dielectric-loaded horn antenna matched to the ground, and the air-ground interface was neglected. To model the antenna, two perpendicular dipoles parallel to the surface were used as radiating sources. The above model was verified by comparing calculated scattered fields with measurements from buried cylinders having different diameters and permittivities. It was found that they agree well in both the frequency and time domains.

After validation of the model, scattering from roots was explored. We began by computing the scattering characteristics of a root as a function of frequency and diameter. The trend obtained matched that found for scattering from an infinite dielectric cylinder. Comparisons of spatially scanned time-domain responses obtained from both measurements at Eglin and model predictions were also shown to be in good agreement.

Two issues concerning the effects of roots on GPR performance were studied, namely, root-generated clutter and root-related target signature distortion. GPR responses directly over a number of roots were computed and fitted to a log-normal probability density. Analysis showed that this root-related clutter would produce high false alarm rates, particularly for sensors that had significant frequency content above about 0.5 GHz. Simulations of target signatures with and without overlying roots showed that the roots produce little signature distortion, adding only a small amount of attenuation and a modest time delay. Finally, attempts to image root signatures were successful, which suggest that roots are best treated as discrete clutter artifacts, rather than a continuous random phase screen. In summary, we concluded that the primary effect of roots is to add a randomly distributed set of discrete clutter sources, and that any root-related loss in performance can be partially offset by using lower frequencies.

A number of issues should be explored in any extension of this effort. First, the current form of the DDA code does not handle targets that are perfect electric conductors (PECs). It is suggested that the code be extended to include those targets.

Second, for a GPR antenna that does not contact the surface such as BoomSAR, the air-ground interface must be included in the model. To deal with the interface rigorously, it will be necessary to include Sommerfeld integrals, which are computationally expensive. A fast algorithm for computing those integrals would be essential for this effort.

Third, additional root samples should be investigated. This analysis was focused on a single root structure, which occupied an area of only 4 m^2. From this small sample it is difficult to identify and characterize root anomalies that drive system performance in an application such as UXO detection, which is defined by the occurrence of low probability events.

Finally, the universal curves should be extended to approximate the fields scattered from an average root structure such that we can approximate average root returns without using the DDA code.

Appendix A : Frequency Response of an Infinitely Long Perfectly Conducting Wire in the Frequency Range from 0.05-1.5 GHz

In this appendix we show that the frequency response of an infinitely long, perfectly conducting wire varies slowly for frequencies in the range 0.05 to 1.5 GHz. This result justifies our decision to approximate wire scattering as a frequency independent constant, which was done in our calibration procedure.

Consider the problem of plane wave scattering from an infinitely long cylinder with a radius a = 0.5 mm in a medium with dielectric constant ε_r = 5. The problem geometry is illustrated in Figure A1.

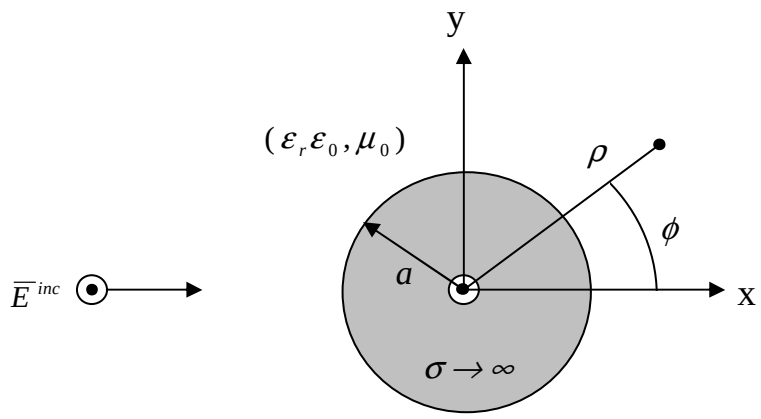

Figure A1. TM_z plane wave impinges on a conductive circular cylinder.

It can be shown that if we excite the problem with a TE_z uniform plane wave, a field scattered from a conductive thin cylinder is negligible [23]. As a result, only the TM_z case will be considered here. With the suppression of the factor $e^{-i\omega t}$, the field scattered from a TM_z plane wave can be expressed as [23]

$$\overline{E}_s = -\hat{z}E_o \sum_{n=0}^{\infty} (i)^n \varepsilon_n \frac{J_n(\beta\sqrt{\varepsilon_r}a)}{H_n^{(1)}(\beta\sqrt{\varepsilon_r}a)} H_n^{(1)}(\beta\sqrt{\varepsilon_r}\rho)\cos(n\phi) \qquad \text{(A-1)}$$

where

$J_n(.)$ = the Bessel function of the first kind of order n (n is an integer).

$H_n^{(1)}(.)$ = the Hankel function of the first kind of order n.

E_0 = magnitude of incident fields (set to 1).

$$\beta = \omega\sqrt{\mu_0 \varepsilon_0} \tag{A-2}$$

$$\varepsilon_n = \begin{cases} 1 & if\ n = 0 \\ 2 & if\ n \neq 0 \end{cases} \tag{A-3}$$

For an electrically thin wire the quantity $\beta a << 1$. Using the small argument approximations to the Bessel and Hankel functions described in Chapter 3, it is clear that the n=0 term dominates the series in (A-1). We can write

$$\left| \overline{E}_s \right| \approx \left| \frac{\pi}{2} \frac{H_0^{(1)}(\beta\sqrt{\varepsilon_r}\rho)}{\ln\left(\frac{1.781\beta\sqrt{\varepsilon_r}\, a}{2}\right)} \right| \tag{A-4}$$

Figure A2 shows the magnitude of the backscattered field as a function of frequency. For the entire frequency range shown, the variation in magnitude is about 4 dB, but for most of the range, i.e., from 0.3 to 1.5 GHz, the variation is 2 dB, which is quite small. As a result, we can approximate the frequency response of a long conducting wire as independent of frequency with a small error, which arises primarily at low frequency.

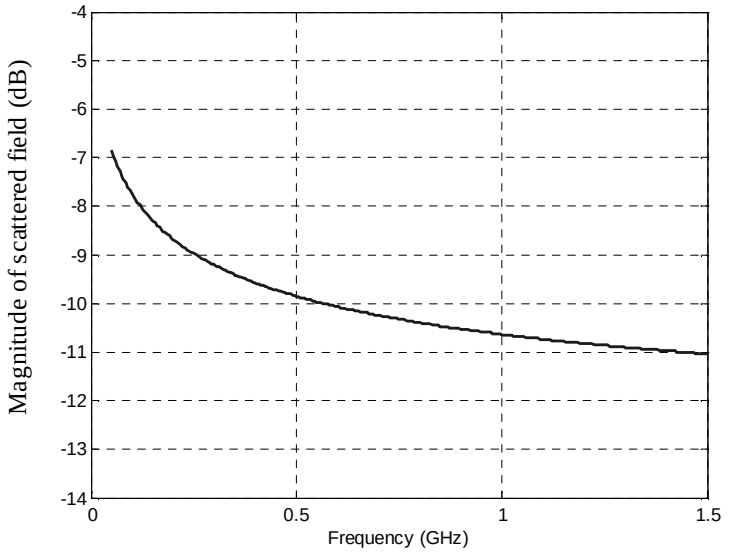

Figure A2. Magnitude of the field backscattered from a wire of radius 0.5 mm in a medium with relative permittivity ε_r = 5 as a function of frequency. Here ρ = 0.3 m and ϕ =180^o.

Appendix B: Dielectric Constant of Tree Roots

In this work we employed a root dielectric constant model known as the "Debye-Cole dual-dispersion dielectric model," which was developed by Ulaby *et al*. [33]. The model's authors asserted that it provides a good estimate of the dielectric constant for leaves, stalks and trunks, and herein we have applied it to roots as well. In this model the following three components contribute to the dielectric constant

a) dry bulk vegetation material,

b) free water, and

c) bound water.

Only the formulae required to compute the dielectric constant are shown here. Further details are given in [33]. The expressions for the dielectric constant of vegetation ε_v is

$$\varepsilon_v = \varepsilon_r + vf\,\varepsilon_f + v_b\,\varepsilon_b \tag{B-1}$$

where

$$\varepsilon_r = 1.7 - 0.74\,Mg + 6.16\,Mg^2 \tag{B-2}$$

$$v_{fw} = Mg\,(0.55\,Mg - 0.076) \tag{B-3}$$

$$\varepsilon_f = 4.9 + \frac{75}{1 - \frac{i\,f}{18}} + \frac{i18\sigma}{f} \tag{B-4}$$

$$v_b = \frac{4.64\,Mg^2}{(1 + 7.36\,Mg^2)} \tag{B-5}$$

$$\varepsilon_b = 2.9 + \frac{55}{1 + \left(\frac{(-i)\,f}{0.18}\right)^{0.5}} \tag{B-6}$$

$$\sigma = 1.27 \tag{B-7}$$

Mg = gravimetric moisture content, defined as

[weight of water in a root (g)] / [weight of a root (g)]

f = frequency in GHz.

Measurements at ESL of the gravimetric moisture content for five root samples acquired at Eglin yielded the Mg values 0.450, 0.500, 0.568, 0.660, and 0.730. The

average value is 0.58. For this value, the real and imaginary parts of ε_v are computed from (B-1) and shown in Figure B1 as a function of frequency. Note that this model is valid (produces error less than $\pm 20\%$) for the frequency range from 0.5 to 20.0 GHz. Since we are interested in the frequency range from 0.05 to 1.0 GHz, we will not use the exact model in the DDA code, but the round number of ε_v instead. Throughout the report, ε_v is set to be 20+10*i*.

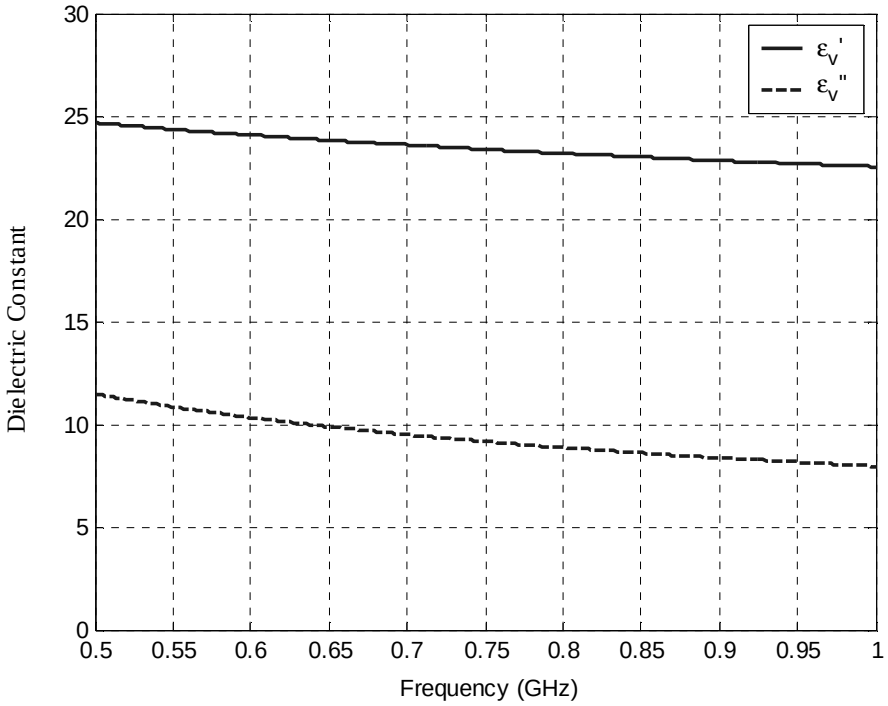

Figure B1. Real and imaginary parts of ε_v of a root with gravimetric moisture content = 0.58.

Appendix C: Dielectric Constant of Soils

Samples of soils from Eglin AFB, FL were collected at two sites by a team from ESL. As described in the first report [1], these sites were chosen to have high and low root densities, and are referred to as "Site 1" and "Site 2," respectively. Soils were collected at six inches depth intervals from surface to three feet. The dielectric constant and conductivity of samples from Site 1 were measured by the U.S. Army Research Laboratory (ARL).

Soil moisture contents from Site 1 and Site 2 were measured at ESL, and the data are shown in Table C1 and C2, respectively. The data are plotted in Figure C1. Figures C2, C3 and C4 show the dielectric constant and conductivity of the soil as a function of its depth and frequency (0.1-3 GHz) for soil with gravimetric moisture content 0%, 5%, and 10%, respectively.

Table C1 Moisture Contents of Soils from Site 1

Depth (inch)	% Water by Weight
0	3.1
6	4.6
12	4.6
18	4.3
24	4.4
30	4.6
36	4.9

Table C2 Moisture Contents of Soils from Site 2

Depth (inch)	% Water by Weight
0	2.4
6	4.6
12	4.4
18	4.6
24	5.2
30	4.9
36	4.6

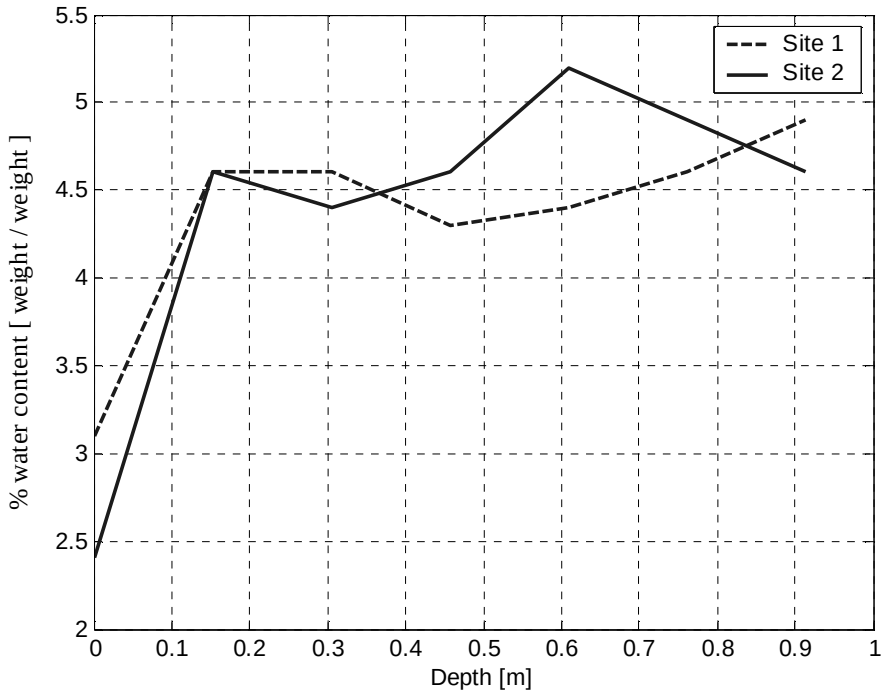

Figure C1. Moisture content of soil from Site 1 and Site 2.

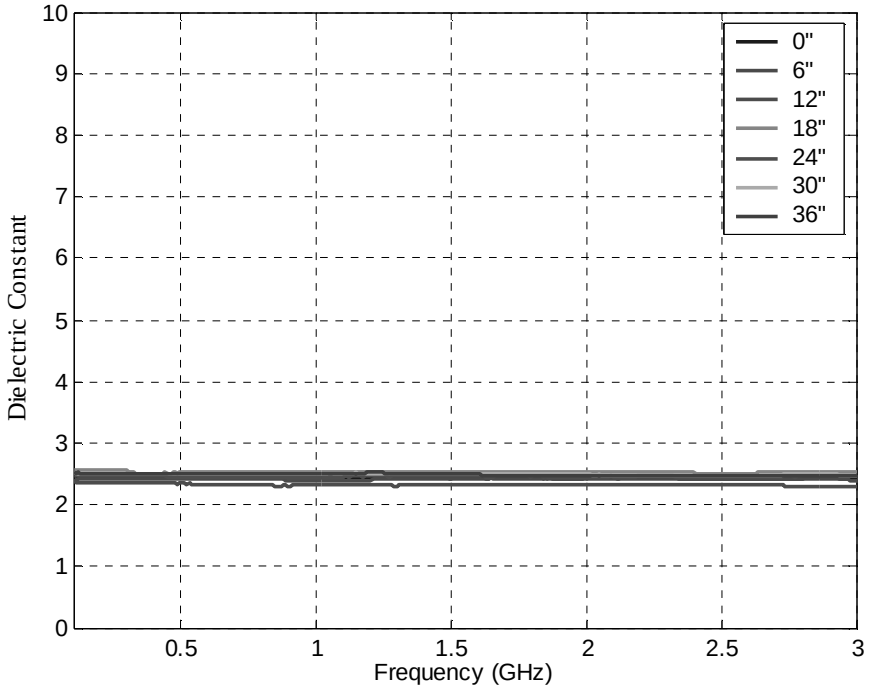

(a)

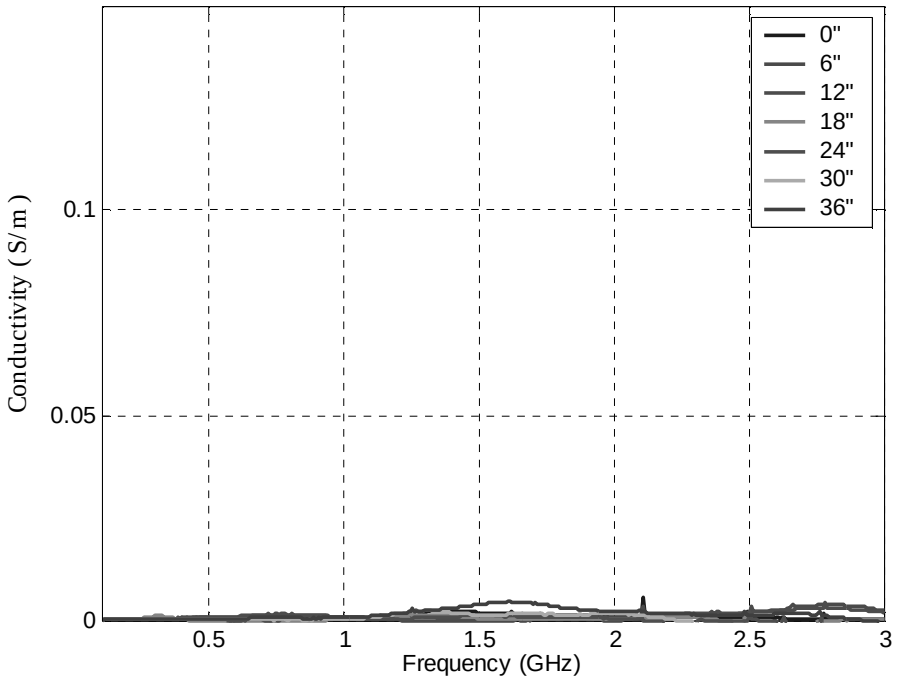

(b)

Figure C2. Characteristic parameters for soil with moisture content 0% at different depths. (a) Dielectric constant. (b) Conductivity.

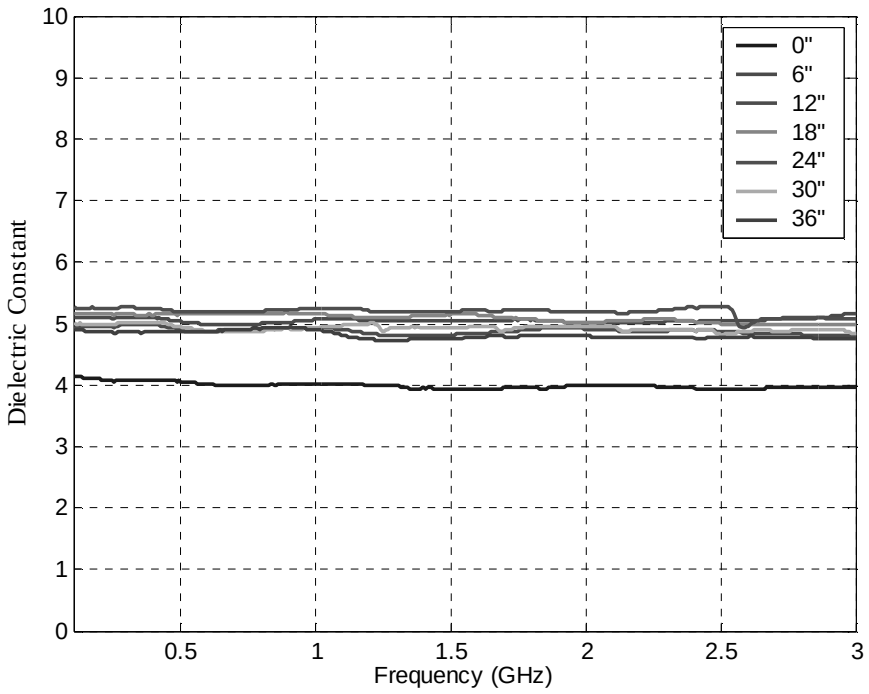

(a)

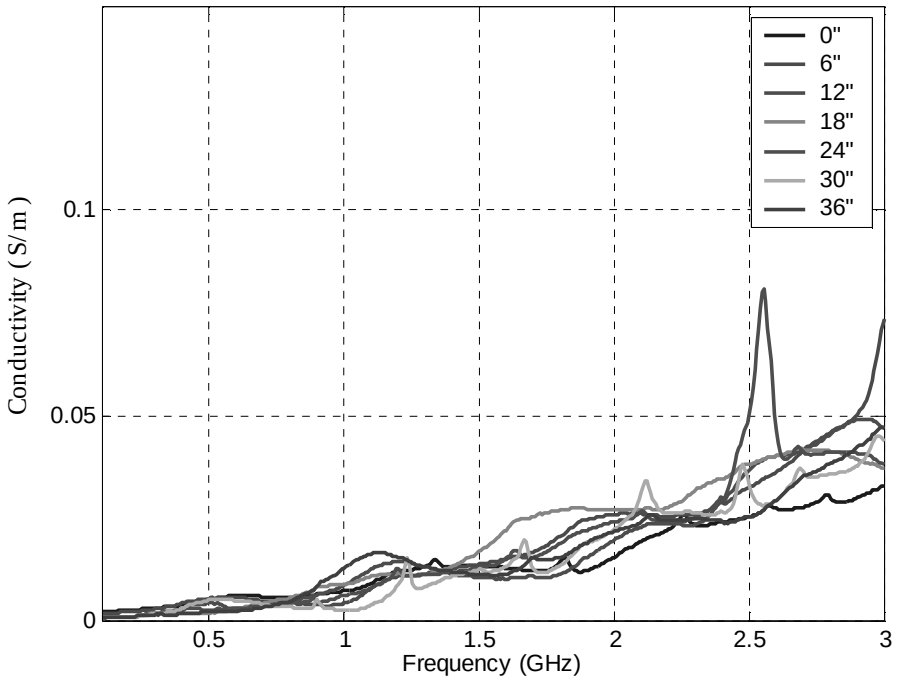

(b)

Figure C3. Characteristic parameters for soil with moisture content 5% at different depths. (a) Dielectric constant. (b) Conductivity.

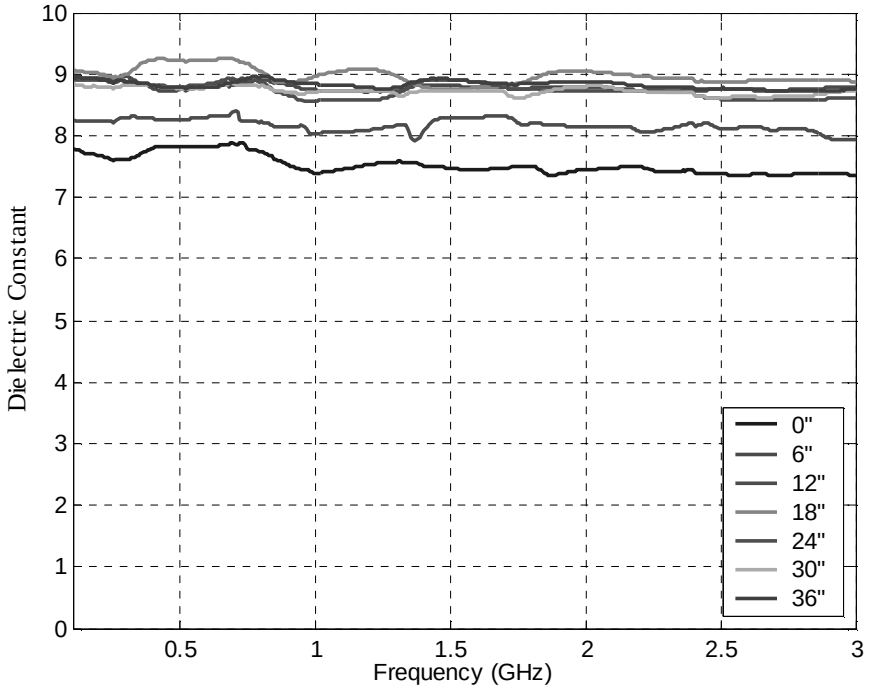

(a)

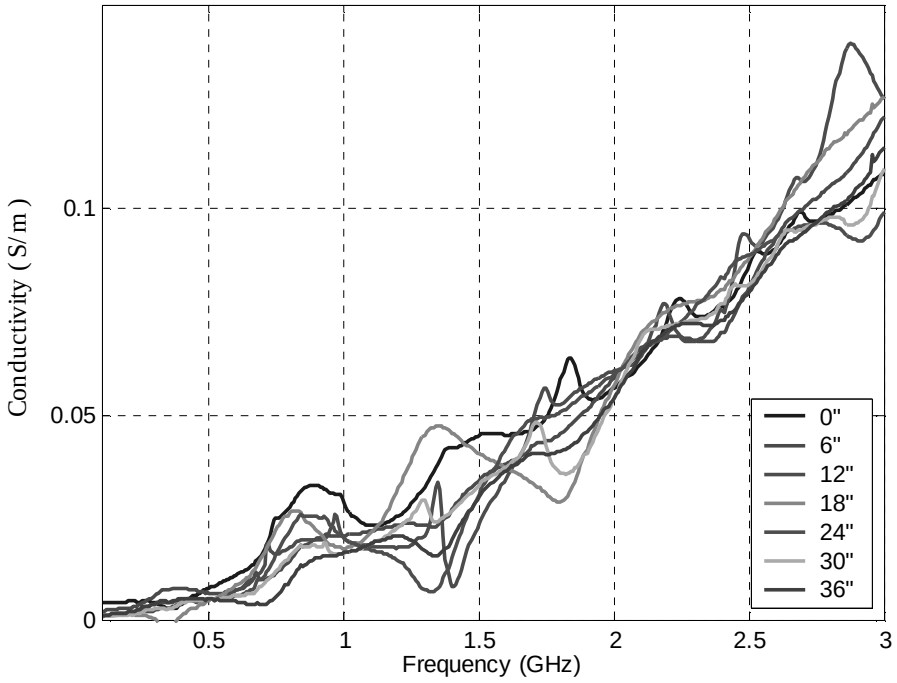

(b)

Figure C4. Characteristic parameters for soil with moisture content 10% at different depths. (a) Dielectric constant. (b) Conductivity.

It can be seen that the moisture content of the soil is approximately 5%, although the surface soil is notably drier. Also, it was noted in the first report [1] that at higher frequencies, i.e., for f > 1 GHz, the higher soil absorption decreases the penetration depth, making the radar insensitive to the roots. As a result, the data from Site 1 for frequencies less than 1 GHz with moisture content 5% are of special interest and are shown in Figures C5 and C6. From the last two figures, the average values of dielectric constant and conductivity at six inch depths are found to be approximately 5 and 0.0035 S/m, respectively. These soil parameters are used throughout the report.

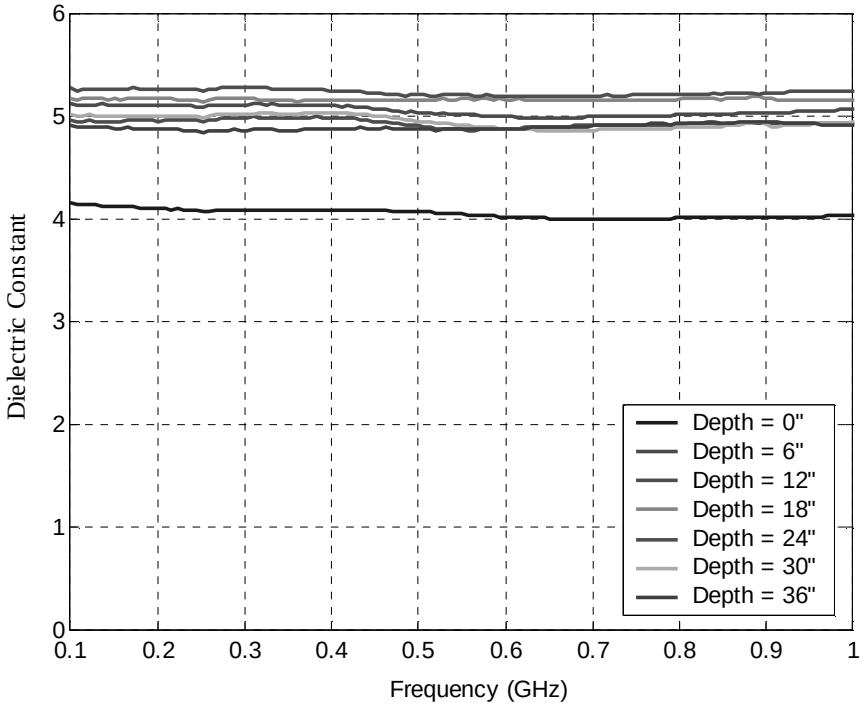

Figure C5. Dielectric constant of the soil samples with moisture content 5% from different depths.

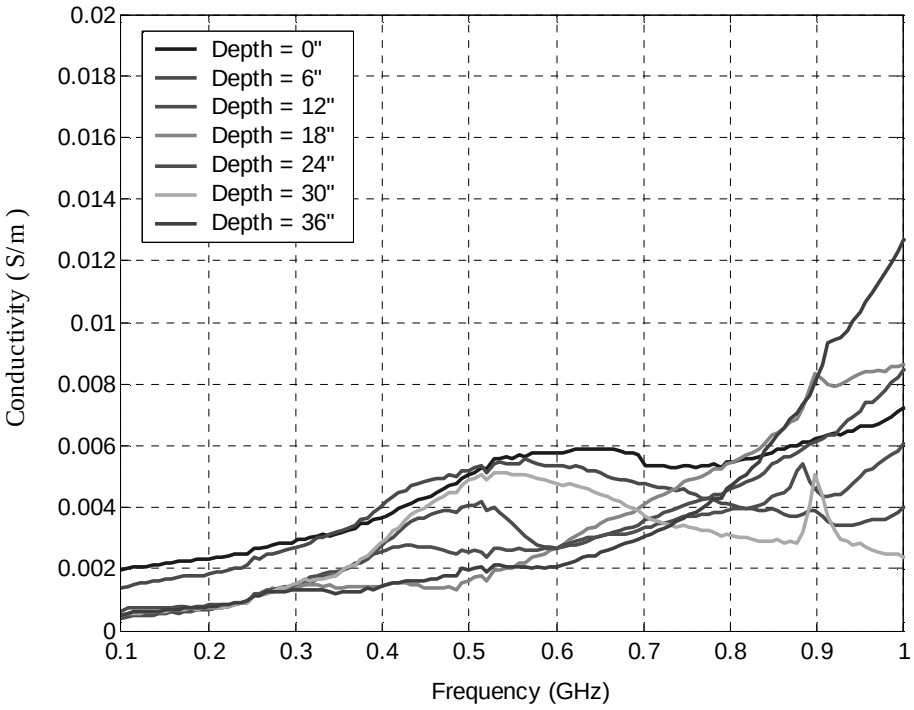

Figure C6. Conductivity of the soil samples with moisture content 5% from different depths.

References

[1] M. Higgins, N. Niltawach, J. T. Johnson, C.-C. Chen, and B. A. Baertlein, "GPR Performance in the Presence of Buried Biomass-Part 1: Experimental Findings," Technical Report, The Ohio State University, ElectroScience Laboratory, Sep. 2002.

[2] G. Lombardi, G. Manara, G. Pelosi, and G. Toso, "Scattering by buried dielectric objects: Volumetric Integral Equation Approach," *Proc. IGARSS Conf.*, vol. 1, 1995, pp. 24-26.

[3] S. F. Mahmoud, S. M. Ali, and J. R. Wait, "Electromagnetic scattering from a buried cylindrical inhomogeneity inside a lossy earth," *Radio Sci.*, vol. 16, pp. 1285-1298, Nov./Dec. 1981.

[4] N. P. Zhuck, and A. G. Yarovoy, "Two-dimensional scattering from an inhomogeneous dielectric cylinder embedded in a stratified medium: case of TM polarization," *IEEE Trans. Antennas Propagat.*, vol. AP-42, pp. 16-21, Jan. 1994.

[5] C. M. Butler, and X. B. Xu, "TE scattering by partially buried and coupled cylinders at the interface between two media," *IEEE Trans. Antennas Propagat.*, vol. AP-38, pp. 1829-1990, Nov. 1990.

[6] X. B. Xu, and C. M. Butler, "Current induced by TE excitation on coupled and partially buried cylinders at the interface between two media," *IEEE Trans. Antennas Propagat.*, vol. AP-38, pp. 1823-1990, Nov. 1990.

[7] K. A. Michalski, and D. Zheng, "Electromagnetic scattering and radiation by surfaces of arbitrary shape in layered media, Part I: Theory," *IEEE Trans. Antennas Propagat.*, vol. AP-38, pp. 335-343, Mar. 1990.

[8] T. J. Cui, and A. Herschlein, "Electromagnetic scattering by multiple three-dimensional scatterers buried under multilayered media-Part I: Theory," *IEEE Trans. Geosci. Remote Sensing*, vol. GE-36, pp. 526-534, Mar. 1998.

[9] T. J. Cui, and W. C. Chew, "Fast algorithm for electromagnetic scattering by buried 3-D dielectric objects of large size," *IEEE Trans. Geosci. Remote Sensing*, vol. GE-37, pp. 2597-2608, Sep. 1999.

[10] T. J. Cui, and W. C. Chew, "Fast evaluation of Sommerfeld integrals for EM scattering and radiation by three-dimensional buried objects," *IEEE Trans. Geosci. Remote Sensing*, vol. GE-37, pp. 887-900, Mar. 1999.

[11] A. Sullivan, "Model-based summary conclusions on the use of UWB radar for detecting unexploded ordnance," *Proc. SPIE.*, vol. 4742, pp. 291-302, Apr. 2002.

[12] M. Shenawee, and C.M. Rappaport, "Monte Carlo simulations for clutter statistics in minefields: AP-mine-like-target buried near a dielectric object beneath 2-D random rough ground surfaces," *IEEE Trans. Geosci. Remote Sensing*, vol. GE-40, pp. 1416-1426, Jun. 2002.

[13] B. T. Draine, and P. Flatau, "The discrete-dipole approximation for scattering calculations," *J. Opt. Soc. Am. A*, vol. 11, no. 4., pp. 1491-1499, 1994.

[14] L. Tsang, J. A. Kong, K. H. Ding, and C. O. Ao, *Scattering of Electromagnetic Waves-Numerical Simulations*. New York: Wiley, 2001.

[15] A. D. Yaghjian, "Electric Dyadic Green's Functions in the Source Region," *in Proc. IEEE*, vol.68, pp.248-263, Feb. 1980.

[16] W. C. Chew, *Waves and Fields in Inhomogeneous Media*, New York: Van Nostrand Reinhold, 1995.

[17] W. C. Au, "Computational Electromagnetics in Microwave Remote Sensing," Ph.D. dissertion, Univ. Massachusetts Institute of Technology, 1994.

[18] P. Flatau, "Improvements in the discrete-dipole approximation method of computing scattering and absorption," *Optics Letters*, vol. 22, no. 16, pp. 1205-1207, 1997.

[19] J. M. Putnam, and L. N. Medgyesi-Mitschang, "Electromagnetic scattering from axially inhomogeneous bodies of revolution," *IEEE Trans. Antennas Propagat.*, vol. AP-32, pp. 797-806, Mar. 1984.

[20] M. G. Andreasen, "Scattering from bodies of revolution," *IEEE Trans. Antennas Propagat.*, vol. AP-13, pp. 303-310, 1965.

[21] J. R. Mautz, and R. F. Harrington, "Radiation and scattering from bodies of revolution," Appl. Sci. Re., vol 20, pp.405-435, 1969.

[22] E. H. Newman, "A user's manual for the electromagnetic surface patch code: ESP version 5," ElectroScience Laboratory, The Ohio State University, July 1999.

[23] C. A. Balanis, *Advanced Engineering Electromagnetics*, New York: Wiley, 1989.

[24] C. A. Balanis, *Antenna theory-analysis and design*, New York: Wiley, 1997.

[25] C. C. Chen, “Development of custom dielectric-loaded horn antenna,” Tech. Rep. 741582-1, The Ohio State University, ElectroScience Laboratory, Columbus, Ohio, Feb. 2002.

[26] K. Rama Rao, K.-H. Lee, C-C. Chen and R. Lee, “Application of Full-Polarimetric Groung Penetrating Radar for Buried UXO Classification,” Technical Report, 738520-1, The Ohio State University, ElectroScience Laboratory, Feb. 2001.

[27] D. M. Pozar, *Microwave Engineering*, New York: Wiley, 1998.

[28] H. L. Van Trees, Detection, *Estimation, and Modulation Theory*, pp. 33-36, New York: Wiley, 1968.

[29] R. Stolt, “Migration by Fourier transform,” *Geophysics*, vol. 43(1), pp. 23-48, 1978.

[30] J. Gazdag, and P. Sguazzero, “Migration of seismic data,” *Proceedings of IEEE*, vol. 10, pp. 1302-1315, Oct. 1984.

[31] C. Cafforio, C. Prati, and F. Rocca, “SAR data focusing using seismic migration techniques,” *IEEE Trans. Aerospace Electron. Syst.*, vol. 27, pp. 194-206, 1991.

[32] J. F. Claerbout, *Imaging the Earth Interior*, Blackwell Scientific Publications, Oxford, UK, 1978.

[33] F. T. Ulaby, and M. A. El-Rayes, “Microwave Dielectric Spectrum of Vegetation-Part II: Dual-Dispersion Model,” *IEEE Trans. Geosci. Remote Sensing*, vol. GE-5, pp. 550-557, Sep. 1987.